

# Argonne National Laboratory

CHEMICAL ENGINEERING DIVISION

RESEARCH HIGHLIGHTS

January — December 1969

The facilities of Argonne National Laboratory are owned by the United States Government. Under the terms of a contract (W-31-109-Eng-38) between the U. S. Atomic Energy Commission, Argonne Universities Association and The University of Chicago, the University employs the staff and operates the Laboratory in accordance with policies and programs formulated, approved and reviewed by the Association.

#### MEMBERS OF ARGONNE UNIVERSITIES ASSOCIATION

The University of Arizona	Kansas State University	The Ohio State University
Carnegie-Mellon University	The University of Kansas	Ohio University
Case Western Reserve University	Loyola University	The Pennsylvania State University
The University of Chicago	Marquette University	Purdue University
University of Cincinnati	Michigan State University	Saint Louis University
Illinois Institute of Technology	The University of Michigan	Southern Illinois University
University of Illinois	University of Minnesota	University of Texas
Indiana University	University of Missouri	Washington University
Iowa State University	Northwestern University	Wayne State University
The University of Iowa	University of Notre Dame	The University of Wisconsin

#### LEGAL NOTICE

This report was prepared as an account of Government sponsored work. Neither the United States, nor the Commission, nor any person acting on behalf of the Commission:

A. Makes any warranty or representation, expressed or implied, with respect to the accuracy, completeness, or usefulness of the information contained in this report, or that the use of any information, apparatus, method, or process disclosed in this report may not infringe privately owned rights; or

B. Assumes any liabilities with respect to the use of, or for damages resulting from the use of any information, apparatus, method, or process disclosed in this report.

As used in the above, "person acting on behalf of the Commission" includes any employee or contractor of the Commission, or employee of such contractor, to the extent that such employee or contractor of the Commission, or employee of such contractor prepares, disseminates, or provides access to, any information pursuant to his employment or contract with the Commission, or his employment with such contractor.

Printed in the United States of America

Available from

Clearinghouse for Federal Scientific and Technical Information

National Bureau of Standards, U. S. Department of Commerce

Springfield, Virginia 22151\*

Price: Printed Copy \$3.00; Microfiche \$0.65



ARGONNE NATIONAL LABORATORY  
9700 South Cass Avenue  
Argonne, Illinois 60439

CHEMICAL ENGINEERING DIVISION  
RESEARCH HIGHLIGHTS

January-December 1969

R. C. Vogel, Division Director  
L. Burris, Associate Division Director  
A. D. Tevebaugh, Associate Division Director  
D. S. Webster, Associate Division Director  
E. R. Proud, Assistant Division Director  
J. Royal



## TABLE OF CONTENTS

ABSTRACT	1
I. FUEL-CYCLE TECHNOLOGY	1
A. LIQUID METAL-MOLTEN SALT TECHNOLOGY	1
1. Decladding by Liquid Metals	1
2. High-temperature Mixer-Settler Development	4
3. Pyrochemical Purification of Plutonium-238	7
B. FLUIDIZATION AND VOLATILITY PROCESSING	8
1. Reprocessing Fast Breeder Reactor Fuels	8
2. Fluidization Technology	11
C. CONVERSION OF FBR OXIDE FUELS TO CARBIDE FUELS	13
REFERENCES AND FOOTNOTES	14
II. SODIUM TECHNOLOGY	15
A. INTRODUCTION	15
B. CHEMICAL DEVELOPMENTS	15
1. Sodium Chemistry	15
C. ENGINEERING DEVELOPMENTS	19
1. Sodium Purification and Monitoring of Sodium Purity	19
2. Fission Product Behavior and Control	21
3. Nature and Control of Formation of Sodium Aerosol	21
REFERENCES AND FOOTNOTES	22
III. MATERIALS CHEMISTRY AND THERMODYNAMICS	23
A. HIGH-TEMPERATURE THERMODYNAMIC STUDIES	23
1. Volatilization Studies of Plutonium Compounds by Mass Spectrometry	23
2. Phase Diagram of the Uranium-Plutonium-Oxygen System	25
3. Equilibrium Studies of Uranium-Fission Product-Oxygen Systems	26
4. Transpiration Studies of the Uranium-Carbon System	26
B. STUDIES OF REACTOR SAFETY AND PHYSICAL PROPERTIES	27
1. Enthalpies and Heat Capacities by Drop Calorimetry	27
2. Other Studies of Physical Properties	28
3. Segregation in Ceramic Fuels: Studies of Fuel Migration	28
C. CALORIMETRY	29
1. Thermochemistry of Uranium Compounds: Enthalpy of Formation of Uranium Diboride	30
2. Thermochemistry of Plutonium Compounds: Enthalpy of Formation of Plutonium Monocarbide	30
3. Thermochemistry of Hydrogen Fluoride	30
4. Chemical Bonding in $\text{NSF}_3$ , NSF, and NS	32
5. Enthalpy of Formation of Molybdenum Disulfide	32
6. Thermochemistry of Aqueous Xenon Trioxide	32
7. Enthalpies of Formation of $\text{KBrO}_4(\text{c})$ and $\text{KBrO}_3(\text{c})$ and the Thermodynamic Properties of the Perbromate and Bromate Ions	33
REFERENCES AND FOOTNOTES	33
IV. ANALYTICAL AND REACTOR CHEMISTRY	35
A. CHEMISTRY OF IRRADIATED FAST-REACTOR FUELS AND MATERIALS	35
1. Electron-microprobe Analysis of Irradiated $\text{UO}_2$ -PuO <sub>2</sub> Fuel	35
2. Electron-microprobe Analysis of Irradiated UC-PuC Fuel	37

## TABLE OF CONTENTS

B.	XENON TAGGING OF FUEL ELEMENTS IN EBR-II	38
1.	Preparation of Xenon-tag Mixtures	38
2.	Implementation of Xenon-tagging System	38
C.	DETERMINATION OF BURNUP IN FAST-REACTOR FUELS	39
1.	X-ray-spectrometric Determination of Fission Product Rare Earths	39
2.	A New Method for the Determination of Fast-fission Yields	40
	REFERENCES AND FOOTNOTES	40
V.	CHEMISTRY OF LIQUID METALS AND MOLTEN SALTS	41
A.	STUDIES OF LIQUID METALS	41
1.	Thermodynamics	41
2.	Transport Properties: Electronic Conductivity of Selenium- and Sulfur-containing Cathode Alloys	47
B.	STUDIES OF MOLTEN SALTS	48
1.	Thermodynamics: Phase Diagrams of Lithium Halide-containing Systems	48
2.	Structure Investigations by Spectroscopic Methods	50
C.	STUDIES OF ENERGY CONVERSION	51
1.	Lithium/Chalcogen Cells	51
2.	Immobilization of Fused-salt Electrolytes	55
3.	Materials Stability	57
D.	BATTERY DEVELOPMENT	57
1.	High-specific-energy Lithium/Selenium Batteries for Implantation	57
2.	High-specific-power Lithium/Selenium Cells for Vehicle Propulsion	59
3.	Lithium/Sulfur Cells for Vehicle Propulsion	62
4.	Performance Comparison	63
	REFERENCES AND FOOTNOTES	65
VI.	FLUIDIZED-BED COMBUSTION OF FOSSIL FUELS	67
	REFERENCES AND FOOTNOTES	68
VII.	ADDENDUM	69

## ABSTRACT

During 1969, Argonne's Chemical Engineering Division pursued continuing studies while initiating several new investigations. High-temperature data are being determined to evaluate the performance of FBR fuels and the safety of FBR materials under accident conditions. The calorimetric program is directed toward the properties of substances of interest in high-temperature chemistry and nuclear technology. Analytical and reactor chemistry investigations include the chemistry of irradiated FBR materials, xenon tagging to locate failed EBR-II fuel elements, and methods for determining burnup in FBR fuels. Of importance to LMFBRs, energy-conversion devices, and other applications are studies of liquid metals and molten salts. The investigation, begun last year, of the fluidized-bed combustion of fossil fuels as a means of reducing the emission of pollutants is progressing.

New investigations were started in two areas: While secondary-cell investigations continue in the energy-conversion studies, work was initiated to develop batteries for human implantation and vehicular propulsion. A program of sodium technology was instituted to develop equipment and procedures to control sodium contamination and corrosion in LMFBRs; the program incorporates on-going studies of sodium chemistry.

## I. FUEL-CYCLE TECHNOLOGY

### A. LIQUID METAL-MOLTEN SALT TECHNOLOGY

Compact pyrochemical processes have been under development for the decontamination and recovery of spent fast breeder reactor (FBR) fuels. Because radiation-stable liquid metal and salt solvents are used in these processes, they can accommodate short-cooled, high-burnup fuels, thereby permitting rapid recycle of the fuel and a reduction in out-of-reactor inventory costs.

The recent pyrochemical studies have been concentrated on the development of a salt-transport process for the recovery of FBR fuels. This process, which is described in detail in the preceding report of this series (ANL-7550, pp. 7-9), consists of the following operations:

Stainless steel cladding is removed from the oxide fuel by dissolution of the cladding in liquid zinc. The separated fuel oxide is then reduced to metal by a Cu-Mg-Ca alloy with the aid of a  $\text{CaCl}_2\text{-CaF}_2$  flux; the volatile fission products released during the decladding and reduction steps are collected in the argon cover gas. Subsequently, plutonium and uranium are separated from fission products in a series of liquid metal-molten salt extraction steps, probably in high-temperature mixer-settlers. After these purification steps, metallic plutonium and uranium are recovered from product solutions by vacuum distillation of the final solvent metal (Zn-Mg). The actinide metals are next powdered by hydriding, then reconverted to the oxides by treatment with  $\text{CO}_2$  in a fluidized-bed reactor.

Most of the process chemistry has been investigated and is well understood. Much of the required basic engineering

information is also available, and work was started on facilities for a bench-scale engineering demonstration of the process. In mid-1969, development work on the salt-transport process was terminated because of budget cuts. However, a reduced effort is continuing on the development of the procedure for liquid metal decladding as an alternative to mechanical decladding schemes such as the shear-leach method that has been proposed as the head-end step for aqueous processing of FBR fuels.

In other work, liquid metal-molten salt extraction techniques similar to those used in the salt transport process have been investigated as a means of recovering and purifying plutonium-238 from recycled scrap materials generated in the preparation of isotopic power sources. Experimental studies showed that the necessary separation of plutonium from impurities (such as light elements that cause neutron emission through  $\alpha, n$  reactions) can be achieved, but that additional work is required to establish the technical feasibility of a complete process. This program was also terminated in mid-1969 for lack of funding.

### 1. Decladding by Liquid Metals

#### a. Plant Concept for FBR Fuel Decladding

A conceptual design study was initiated of a plant for decladding 5 metric tons/day of stainless steel-clad LMFBF core and blanket fuel assemblies in molten metal. This head-end facility is assumed to be coupled to a large, central, aqueous reprocessing plant, although the concept is

also applicable to smaller plants and to separate head-end plants. Objectives are to achieve process simplicity, to minimize the number of mechanical handling steps, and to minimize the required shielded area and number of process vessels.

Decladding with molten metal is an alternative to mechanical decladding schemes,<sup>1\*</sup> which require removal of sodium, disassembly of the fuel assembly, and fuel chopping as separate operations. An advantage of a molten-metal-decladding step is that the fuel oxide does not react with the decladding chemicals and, once separated, can be fed either to an aqueous dissolution step or to another interfacing step. An additional advantage is that no special treatment is required for fuel pins that are sodium-logged as a result of cladding failure or on which sodium is held up externally.

An Atomics International stainless steel-clad  $\text{UO}_2$ -20 wt %  $\text{PuO}_2$  fuel element<sup>2</sup> has been selected as a reference. Special attention must be given to the high plutonium content of this fuel, its high heat load, and its high content of gaseous fission products. Other design bases for this study are similar to those selected for a recent design-concept study of a fluoride volatility plant.<sup>3</sup>

The present study considers the fuel from the time it arrives at the reprocessing plant in sodium-filled shipping casks until the oxide fuel is charged to an aqueous dissolution or other interfacing step. Zinc, which dissolves stainless steel at practical rates, has been selected as the decladding agent in preference to another candidate, antimony-copper,<sup>4</sup> since zinc is capable of adequate stainless steel loadings at moderate temperatures, is considerably cheaper than antimony-copper, and appears to pose less of a containment problem. (Investigations of decladding with zinc and copper-antimony are discussed in following sections of this report.)

Graphite and tungsten are being considered as the material of construction for containment of the molten metal systems. Graphite is the prime candidate for the decladding vessel because it is more readily fabricated and far less expensive than tungsten. For the proposed scale of operation, the vessel would be 8 ft long, 8 ft high, and 2 ft wide. Vessel size was selected on the basis of achieving a 15 wt % loading of stainless steel in zinc.

The tentative scheme for the metal-decladding operations, which would be performed in an inert-gas process cell, includes the following steps:

1) Fuel assemblies are transferred from a sodium-filled shipping cask to a sawing station or to the decladding vessel. The fuel assemblies are transported in turret-like fixtures.

2) Excess hardware is sawed from the inactive end of fuel assemblies for disposal as waste; alternatively, this step may be bypassed and the hardware dissolved with the cladding in the decladding vessel. Disadvantages of the latter alternative would be requirements for larger vessels and a larger inventory of zinc.

3) Fuel assemblies suspended from turrets are loaded vertically into removable, perforated, refractory metal baskets immersed in liquid zinc inside the decladding vessel by attaching the turrets at five loading stations in the top of a decladding vessel. A function of the baskets is to separate batches of fuel from each other for criticality safety; each basket accommodates three fuel assemblies. There are two decladding vessels, which are employed alternately on a 48-hr cycle; a cycle consists of 24 hr for four successive dissolutions (a total of approximately 50-60 fuel assemblies), followed by a 24-hr cleanout step.

4) Cladding is partially dissolved in molten zinc, releasing fission product gases. Total retention of the iodine and other fission product gases is a basic goal of this concept study. Iodine and other volatile fission products that penetrate a salt layer above the metal will be removed from the closed decladding vessel in a purge-gas stream.

5) Dissolution of cladding in mildly agitated zinc solution is completed, allowing the fuel to fall into the baskets.

6) Fuel is removed from the decladding vessel in the metal baskets and transported to the next processing station (e.g., the voloxidizer<sup>1</sup> described by ORNL).

Fuel material that is coarse is readily contained in the baskets. Fuel fines that migrate through the basket to the zinc phase are recovered after each day's operations by a technique that has been demonstrated with  $\text{UO}_2$  fines (see Chemical Engineering Division Annual Report, 1968, ANL-7575, pp. 29-31). The technique consists of contacting the molten zinc with a layer of molten fluoride salt above the metal, which effects transfer of the fuel to the salt phase. (The zinc-stainless steel solution, after monitoring to verify that it does not contain actinides, is cast as rods for storage as waste.) The salt is removed from the decladding vessel and kept in a storage vessel during cleanup of the decladding vessel, then recycled. Processing of the salt is required only when the fuel concentration in the salt becomes high; the fuel loading limit for the salt needs to be established. The layer of molten salt over the zinc in the

\*References and explanatory footnotes are placed at the end of each section.

decladding vessel may also serve other purposes, e.g., suppression of zinc vaporization and trapping of some fission product iodine.

Material and heat balances around the decladding vessel have been prepared, along with preliminary cell layouts, showing that an inert-gas process cell, approximately cube-shaped and 30 ft on a side, would be adequate. The cell includes a floor-port fuel-unloading station, a saw for trimming excess hardware from the fuel assemblies, two decladding vessels, turret storage racks, salt-storage tanks, scales, hoists, manipulators, and auxiliary components. A criticality analysis led to the selection of a decladder design utilizing mass control rather than geometry control.

A very brief, exploratory examination of a continuous decladding concept indicates that it may have advantages in comparison with the batch concept described above. The concept of continuous decladding, which provides for the continuous operation of a single decladding vessel rather than alternating use of two vessels, appears to merit further study.

#### *b. Studies of Cladding Dissolution in Liquid Metal*

Preliminary decladding experiments (see ANL-7550, pp. 13-15) had demonstrated the feasibility of decladding stainless steel fuel assemblies using liquid zinc at 800°C. Dissolutions were rapid and complete. Satisfactory separation of the fuel from the zinc-stainless steel solution with negligible loss of fuel was observed.

**Dissolution Mechanism.** Experiments were conducted to study the mechanism of dissolution-disintegration of type 304 stainless steel cladding by liquid zinc. Stainless steel bar stock was heated in quartz tubes with known quantities of

zinc shot for various times and at several temperatures. The nature of the dissolution-disintegration process was deduced by examination of the cooled product by metallographic, electron microprobe, X-ray, and thermal-analysis techniques.

A photomicrograph of a partially dissolved bar is shown in Fig. I-1. Adjacent to the unattacked steel in the upper right of the micrograph is a wide region of iron-zinc alloy in which the grain sizes increase with distance from the steel (diameters range from <0.04 to 0.1 mm). No relationship is apparent between the size of these grains and the size of the grains in the unreacted stainless steel. A large crack runs through this region toward the steel. At the lower end of the crack, the grains are of fairly uniform size, but become more thinly dispersed in the direction of the zinc melt.

The evidence indicates that dissolution-disintegration begins with penetration of liquid zinc into the stainless steel and with the preferential diffusion of nickel from the steel into the zinc. Iron and chromium also enter the zinc, but at rates lower than that for nickel. As the surface of the steel is depleted of nickel, the structure of the austenitic gamma phase transforms into the ferritic alpha phase.

If sufficient zinc is present, all of the steel is dissolved in the liquid zinc. Cooling of this liquid from the dissolution temperature of 800°C causes a portion to transform to the delta phase, which is 20% more voluminous; thermal analysis indicates that the delta phase forms below 655°C.

**Equipment for Engineering-scale Investigations.** The Plutonium Salt Transport Facility (described in ANL-7550, pp. 17-18), which was being built to demonstrate the complete pyrochemical process flowsheet, is being modified for study of the liquid metal decladding step to prepare

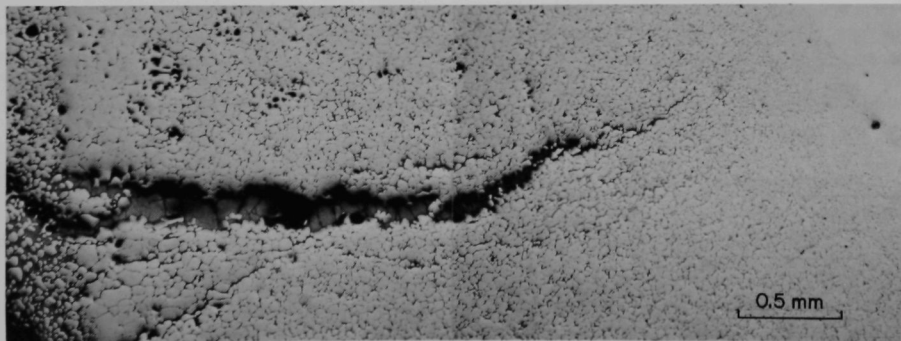


Fig. I-1. Type 304 Stainless Steel Bar after Being Partially Dissolved by Liquid Zinc.



oxide fuel for aqueous processing. Only the gloveboxes for solids handling and decladding will be activated.

**Dissolution Rate.** Three experiments were conducted to determine the relative rates of dissolution in liquid zinc of 1½-in.-dia discs of Zircaloy-2 (cladding for thermal reactor fuel) and of types 304 and 316 stainless steel (potential claddings for fast reactor fuel). In each test, a disc (encased in tantalum except for a 3/4-in.-dia circular area in direct contact with the zinc) was attached to the bottom of a 2-in.-dia agitator. The agitator was lowered into a 4½-in.-dia baffled tungsten crucible containing 3.67 kg of zinc and 100 g of salt (to retard zinc vaporization) at 800°C. The agitator was rotated at 350 rpm to ensure homogeneity of the liquid metal for sampling. Enclosing the sample disc in tantalum prevented the changing configuration of the dissolving disc from altering the mixing characteristics and also provided a fixed, known surface area in the early stages of dissolution. After about one hour of contact, the agitator-disc assembly was removed from the melt for inspection and analysis.

Copper-antimony alloy, recommended by Payrissat and Wurm,<sup>4</sup> is being studied as a backup solvent to zinc. An experiment was performed in which a type 304 stainless steel disc was dissolved in Sb-18 at. % Cu at the higher temperature of 900°C (necessary for adequate solubility of the stainless steel in the Sb-Cu alloy); the other experimental conditions were identical to those described for the zinc experiments.

The initial rates of dissolution for zinc and antimony-copper are given in Table I-1. Although the slowest dissolution was observed for type 304 stainless steel in zinc, this system had previously been demonstrated on an engineering scale to possess a satisfactory decladding rate.

**Effect of Irradiation on Dissolution Rate.** Another experiment was conducted to test the effect of irradiation on the rate of stainless steel dissolution in zinc. A 0.17-in.-dia by 2.6-in.-long, type 304 stainless steel rod that had been irradiated in EBR-II (to an irradiation level equivalent to a burnup of ~2.2 at. % for LMFBR core fuel) was dissolved along with five unirradiated type 304 stainless

steel rods of identical geometry to compare their dissolution rates. The rods were charged to 10 kg of zinc, which was agitated mildly (150-300 rpm) in a 5.6-in.-dia alumina crucible at 800°C. Samples of the zinc were taken intermittently and analyzed for irradiated steel content by measuring the radioactivity of the solution (the original 4-g rod yielded a 25-R beta-gamma contact dose rate, with the principal activity due to <sup>54</sup>Mn). The samples were also analyzed for total iron concentration by wet chemistry, and the dissolution rate of the unirradiated stainless steel was obtained by subtraction. The irradiated steel rod dissolved about twice as rapidly as did the unirradiated rods and was completely dissolved in about 30 min.

**Stainless Steel Loading in Zinc.** A series of four experiments was conducted to investigate the maximum loading of stainless steel in zinc at 850°C and to study the effects of loading on the dissolution rate. Type 304 stainless steel rods (of 3/8-in. diameter by 1 in.) were immersed in 4.8 kg of zinc and 0.1 kg of salt at 850°C, and the system was agitated mildly. In all four experiments, the iron and chromium concentrations of filtered samples of the liquid metal phase rose rapidly to about 5.8 wt % and 1.0 wt %, respectively, and remained essentially constant thereafter. The nickel concentration in the zinc continued to rise until all of the nickel originally in the steel was dissolved. About one-half of the iron and chromium in the stainless steel charged in each experiment was in solution in the zinc; however, examination of the frozen ingots at the end of the experiments showed that the rods had completely disintegrated. Sections of the ingots were metallographically examined (see above for the results of a more extensive study of the dissolution mechanism) and found to contain suspensions of finely divided grains of alpha iron containing zinc and chromium in solid solution. The maximum "solubility" of stainless steel in zinc is about 6 wt % at 850°C, but even after the zinc is saturated with chromium and iron, rapid disintegration of stainless steel continues until loadings of at least 15 wt % (including the suspended solids) are reached. The resulting mixtures appear to be quite fluid, with no evidence of settling of solids; consequently, loadings of at least 15 wt % stainless steel may be possible when decladding with zinc.

Other aspects to be investigated include (1) materials of construction for a full-scale decladding vessel, (2) behavior of sodium and certain fission products during dissolution, (3) proportion of volatile fission products released and trapped, and (4) alternative pyrochemical head-end processes.

## 2. High-temperature Mixer-Settler Development

A conceptual salt-transport process for FBR fuel (see ANL-7550, pp. 7-9) would utilize a semicontinuous

TABLE I-1. Relative Rates of Cladding Dissolution<sup>a</sup>

	Solvent	Temp (°C)	Dissolution Rate (mils/min)
Type 304 stainless steel	Zinc	800	~2
Type 316 stainless steel	Zinc	800	~4
Zircaloy-2	Zinc	800	20 <sup>b</sup>
Type 304 stainless steel	Sb-18 at. % Cu	900	>20

<sup>a</sup>Mild agitation was provided by a 2-in.-dia, 5/8-in.-high agitator at 350 rpm.

<sup>b</sup>After an 8-min induction period.

mixer-settler for removal of rare earth and noble metal fission products from the fuel.

#### a. Agitator-Pump Mixer-Settler Investigations

The proposed design and mode of operation of a seven-stage mixer-settler for the separation of fission products from plutonium by molten salt-liquid metal extraction were described in ANL-7550, pp. 15-17.

During the past year, investigations of mixing and flow characteristics<sup>5</sup> culminated in an agitator-pump and mixing-chamber design for one stage of a multistage mixer-settler. This design provides a 1-liter mixing chamber and a 7.0-cm-dia agitator that produces a high degree of agitation while reducing the bypassing of solutions to an acceptably low level. In a run, some of the salt and metal phases flow continuously between stages; other phases (captive phases) move batchwise between runs (Fig. I-2 shows a captive-metal stage).

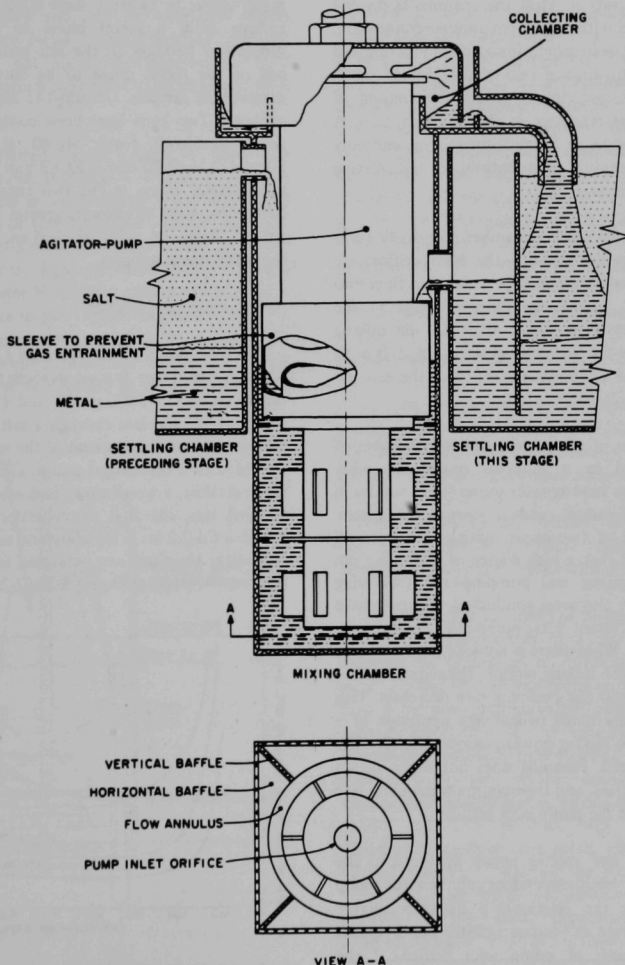


Fig. I-2. Arrangement of Mixing and Settling Chambers (captive-metal stage).

In normal operation with a two-phase system, both phases enter the zone above the mixing chamber and flow downward. A horizontal baffle and a sleeve above the mixing chamber prevent entrainment of gas in the fluids (and thus maintain mixing efficiency) if the liquid level is kept at least 3 cm above the baffle. In the mixing chamber, the two phases are mixed by blades attached to the pump rotor.

A fixed horizontal baffle that has an 8.9-cm-dia opening is located at about mid-elevation of the mixing chamber. A horizontal disc, of 7.6-cm OD, is mounted on the agitator-pump at the same elevation. Thus the chamber is divided into two mixing zones with a 0.65-cm annular connection. This configuration, by decreasing top-to-bottom mixing and approaching the performance of two total backmix<sup>6</sup> stages operating in series, is intended to reduce the amount of material that has short residence in the mixing region. A series of tests conducted in a mock-up mixing assembly allowed the residence-time distribution in the mixing chamber to be determined.

The two phases in the mixing chamber eventually enter the bottom of the pump through the inlet orifice, are pumped up into the collecting chamber, and then flow into the settling chamber. After the fluids separate in the settling chamber, they flow either back to the mixing chamber (as is the case for the metal phase in Fig. I-2) or to the mixing chamber of a following stage (as is the case for the salt phase in Fig. I-2).

During development of the present design, a number of tests were performed in a mockup mixing assembly consisting of a stainless steel agitator-pump (built for use in a high-temperature furnace) and a transparent plastic chamber. Observation of two-phase mixing of water and organic phases showed that a high degree of dispersion can be achieved. Mixing-power and pumping-rate tests using water as a single phase also were conducted. Pumping rates were measured for different lifts, pump-inlet-orifice sizes, and rotational speeds. When there is reduced holdup (i.e., a lower liquid level) in the mixing section, the required lift is increased, and as a result the pumping rate decreases. This holdup-flow relationship tends to stabilize operation of a multistage system. The mixing power is proportional to the cube of rotational speed. Pumping does not begin until a minimum speed is reached, and the maximum pumping rate is limited by the size of the pump inlet orifice.

The pumping rate and mixing power delivered to the mixing chamber are both dependent on agitator-pump speed; Fig. I-3 shows the relationship between mixing power and pumping rate at various agitator-pump speeds for three different sizes of pump inlet orifice. If the extractor is designed to provide satisfactory performance at a minimum agitator-pump speed of about 550 rpm,

satisfactory extraction can be expected at all higher agitator-pump speeds and pumping rates.

A high-temperature, single-stage mixer-settler was fabricated of type 304 stainless steel for operation with molten Mg-Cu alloy and halide salt. The components were designed to give experimental flexibility and to fit into an existing furnace; nevertheless, the mixing chamber and agitator-pump have the same configuration as that shown in Fig. I-2.

A series of extraction runs are being made in this mixer-settler to measure stage efficiency for the transfer of cerium from a metal phase to a salt phase. Cerium distributes strongly to the salt phase, allowing extraction out of the metal phase to be determined precisely with metal-phase samples. Cerium-141 tracer is used to facilitate analyses. Two runs have been completed in which cerium was transferred from Mg-40 at. % Cu to  $\text{MgCl}_2$ -30 mol % NaCl-20 mol % KCl-3 mol %  $\text{MgF}_2$  at 675°C. The salt-to-metal ratios in the two runs were 0.2 and 1.5. In both runs, stage efficiencies greater than 99% were demonstrated, based on radiochemical analysis for cerium-141 in the metal-phase samples.

#### b. Larger-scale Studies

Another facility was operated (1) to test mixer-settler components under typical pyrochemical-processing conditions (see ANL-7550, p. 18) and (2) to demonstrate the transport of uranium through a salt phase and to measure entrainment of liquid metal in the salt. The test equipment consisted of a centrifugal pump, a constant-head tank, two mixer-settlers, a weigh tank, and a sump tank. At the start of each run, the first mixer-settler (mixer-settler 1) contained a Cd-2.2 at. % Mg alloy and uranium in excess of the solubility. Uranium was extracted from this alloy into the flowing salt ( $\text{MgCl}_2$ -30 mol % NaCl-20 mol % KCl) and then

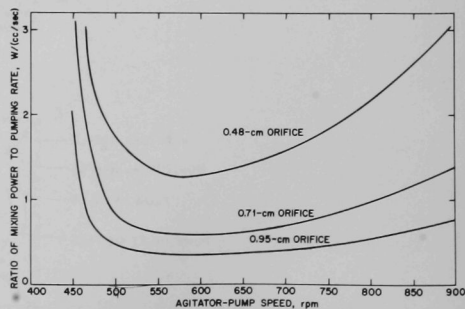


Fig. I-3. Mixing Power-to-Pumping Rate Ratio for Agitator-Pump as a Function of Agitator-Pump Speed and Size of Pump Inlet Orifice (pump lift = 16 cm).

was extracted from the salt in mixer-settler 2 by a Cd-45 at. % Mg alloy. Since magnesium is exchanged for uranium as the uranium is extracted, the magnesium concentration increased in the first alloy and decreased in the second. These two alloys were selected because they allowed demonstration of the salt-transport step in stainless steel apparatus.

In the design used for these mixer-settlers, the salt flows into a central, conical region (see Fig. 1-4), where it mixes with the liquid metal alloy. The salt then flows under the cone and baffle assembly and into the quiescent region outside the cone, where metal droplets separate from the salt by gravity. The salt leaves the mixer-settler tank through a standpipe, which maintains a constant salt level in the tank.

Mass-transfer coefficients were calculated from the extraction data of one run, Run MSL-4. During most of the run, uranium extraction in mixer-settler 1 was limited by the rate of dissolution of uranium metal rods (original size: 3/32-in. diameter; 2 to 3 in. long) by the Cd-Mg alloy. The mass-transfer coefficient,  $K_{sA}$ , in mixer-settler 1 ranged from about 20 to greater than 200 kg U/(min)(wt fraction U in salt phase). The higher values occurred after the uranium particles became small enough to be suspended by the mixer and are equivalent to a stage efficiency of about 98%. The mass-transfer coefficient in mixer-settler 2 had

the relatively constant value of about 55 kg U/(min)(wt fraction U in salt phase), which is equivalent to a stage efficiency of about 94%. The agitation speeds for the two mixer-settlers were 640 and 460 rpm, respectively, corresponding to mixing power densities of 8.5 and 3.6 W/liter.

In a salt-transport process, any entrainment in the salt phase of the metal phase from mixer-settler 1 would lower the achievable decontamination factor. Therefore, in Runs MSL-5 and MSL-6, the amounts of metal entrained with the salt flowing to mixer-settler 2 were measured. An irradiated copper tracer was used in each run to enhance analytical precision. Agitator speeds of 200 to 600 rpm and salt flow rates of 3.1 to 4.7 kg/min were employed. The average rate of entrainment in each run was 0.02 g Cd/kg of salt circulated. The entrainment rate apparently increased with agitator speed, but this trend was only barely detectable. This low level of entrainment is entirely acceptable for most process applications; for the present system, the decontamination factor for nobler elements would be limited to about 750 for a single stage as a result of entrainment.

No further development of mixer-settlers is planned.

### 3. Pyrochemical Purification of Plutonium-238

Pyrochemical-processing techniques were investigated as a means of recovering and purifying plutonium-238 contained in various types of materials, such as scrap from the preparation of isotopic power sources.

The Plutonium-238 Facility, described in ANL-7550 (pp. 20-22) and in a topical report,<sup>7</sup> was used in two laboratory-scale experiments with plutonium-238.

The procedure consisted of suspending impure  $^{238}\text{PuO}_2$  powder or microspheres in a molten chloride salt and reducing the plutonium to metal by mixing the salt with liquid Zn-Mg. The salt and metal phases were separated, and then a metallic plutonium-238 product was recovered by vacuum distillation of the solvent metals. This process effectively removed light-element impurities that contributed undesirable neutron emission by  $(\alpha, n)$  reactions with plutonium-238 alphas. In one experiment, the neutron count of the product was 2930 n/(sec)(g  $^{238}\text{Pu}$ ) [2360 n/(sec)(g Pu)], compared with a neutron count of 42,500 n/(sec)(g  $^{238}\text{Pu}$ ) for the starting material (10 g of  $^{238}\text{PuO}_2$ ). The initial and final neutron counts for the product in the other experiment were 89,300 and 3980 n/(sec)(g  $^{238}\text{Pu}$ ). More than 90% of the plutonium charged was recovered in the vacuum-distillation residue for both runs; the remainder was largely in salt and metal streams that would be recycled in a full-scale process.

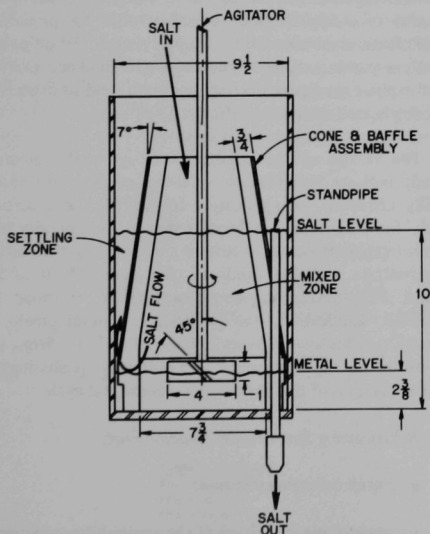


Fig. 1-4. Mixer-Settler (dimensions in inches).

Several experiments were performed with plutonium-239 as a stand-in for plutonium-238. The materials used were  $^{239}\text{PuO}_2$  microspheres and  $^{239}\text{PuO}_2$ -molybdenum cermet.

In one experiment utilizing 10 g of  $^{239}\text{PuO}_2$  microspheres, the procedure was (1) reduction of  $^{239}\text{PuO}_2$  with a Mg-30 wt % Cd reduction-donor alloy in contact with a  $\text{MgCl}_2$ -42 wt %  $\text{CaCl}_2$  salt system, (2) transport of the plutonium away from impurities that remain in the reduction-donor alloy by cycling the salt between the reduction-donor alloy and a Zn-25 wt % Mg acceptor alloy having a high plutonium affinity, and (3) recovery of plutonium-239 metal product by retorting the acceptor alloy. High-purity zinc (nominally 99.9999 wt % Zn) and magnesium (nominally 99.995 wt % Mg) were used for the acceptor alloy. Of the 8.82 g of plutonium charged in this run, 7.827 g was transferred to the acceptor alloy. Of 6.58 g of plutonium retorted in this run, 6.05 g was recovered in the product. The light elements and uranium were successfully removed.

Another experiment with  $^{239}\text{PuO}_2$  microspheres (in which stainless steel also was charged) utilized the following procedure: (1) reduction with Zn-Ca in contact with a  $\text{CaCl}_2$ -KCl salt system, (2) addition of  $\text{ZnCl}_2$  to oxidize the plutonium and excess calcium in the reduction alloy to  $^{239}\text{PuCl}_3$  and  $\text{CaCl}_2$  in the salt phase, (3) transfer of the  $^{239}\text{PuCl}_3$ -bearing salt phase to a Zn-Ca acceptor alloy and reduction of the  $^{239}\text{PuCl}_3$  in the salt to plutonium metal in the acceptor alloy, and (4) recovery of the purified plutonium metal by retorting the acceptor alloy. Spark-source mass-spectrographic analysis of the plutonium metal product indicated that the plutonium had been separated from the bulk of the iron and nickel charged, but not from chromium. There had been no removal of uranium impurity, indicating that processes requiring high removals of uranium should use magnesium rather than calcium as the reducing agent.

Two runs to recover high-purity plutonium metal from  $^{239}\text{PuO}_2$ -molybdenum cermet fuel utilized approximately the same salt, alloy, and transport scheme that were used in processing  $^{239}\text{PuO}_2$  except that the plutonium oxide was converted to the chloride by  $\text{CuCl}_2$  in the salt system prior to transfer of the plutonium to an acceptor alloy. Disintegration of the cermet was effected in both runs, but the plutonium metal product contained excessive concentrations of copper.

These results indicate that pyrochemical processes are generally feasible for these applications, but that the techniques have not been sufficiently developed for use in production. Nevertheless, certain pyrochemical procedures may have immediate production applications. These include

(1) reduction of  $^{238}\text{PuO}_2$  scrap material to produce a metal alloy for subsequent aqueous processing, (2) reduction of relatively pure  $^{238}\text{PuO}_2$  to remove light-element impurities and produce plutonium-238 metal simultaneously, and (3) disintegration of  $^{238}\text{PuO}_2$ -Mo compacts in a  $\text{CuCl}_2$ -containing molten salt for aqueous processing.

Work on this project was discontinued June 30, 1969.

## B. FLUIDIZATION AND VOLATILITY PROCESSING

The basis for the processing method based on fluoride volatility is the reaction of fluorinating agents with fuel materials in fluid-bed systems to produce the volatile hexafluorides of uranium and plutonium, which are separable from nonvolatile fission product compounds. Since volatile fluorides of certain fission product elements accompany  $\text{UF}_6$  and  $\text{PuF}_6$ , additional separation procedures are necessary to produce purified products.

Laboratory investigations during the report period concerned (1) a method for the separation of uranium from plutonium in the fluorination step of the fluoride volatility process for oxidic FBR fuel, (2) the identification of ruthenium fluoride species in product streams from an oxyfluorination step, and (3) the sorption of ruthenium fluorides in cold traps.

Also reported are the conclusions of conceptual design studies of a large fluoride volatility plant for processing FBR fuels, as are the results of supporting studies on pulsed beds; a continuous-feed, two-stage slab fluid-bed reactor; dense-phase transport of granular solids; and heat transfer from a heated surface to a fluidized bed.

The results of the conceptual design and evaluation study indicate that fluoride volatility methods are potentially attractive for application to LMFBR fuels, particularly for long-range fast breeder reactor fuels of very high performance. However, owing to a decision by the AEC to concentrate available funds on the development of the more conventional aqueous reprocessing methods for LMFBR application, the program of development of fluoride volatility processes is being closed out. Work will continue on the application of fluidization technology to other portions of the fast breeder reactor fuel cycle.

### 1. Reprocessing Fast Breeder Reactor Fuels

#### a. Engineering Investigations

An engineering evaluation of the applicability of fluoride volatility methods to LMFBR fuel reprocessing was successfully carried out by using the technique of developing a

reference process design and a reference plant concept to identify key problems and areas of uncertainty.

The design basis for the evaluation was a plant capacity of 1 metric ton of actinides per day from combined core and blanket fuel [15,000 MW(e) equivalent]. A simplified version of the flowsheet (also published in the preceding report) is shown in Fig. 1-5. Results of this study have been presented in a topical report,<sup>8</sup> and the conclusions are repeated here.

The application of fluoride volatility processing to LMFBR fuels is supported by a substantial body of basic and technological information that was generated in re-processing work with other nuclear fuel materials and in related processes. This information, coupled with several innovative design features, provides the basis for this conceptual design study. The reference process shows a high potential for handling highly radioactive, short-cooled fuel, as well as considerable flexibility in processing feed materials with a wide range of concentrations of fissile material. The conceptual plant has a practical size, comparable to the size of existing plants that process LWR fuels. With optimization, a substantially improved process should be expected.

The uniquely difficult characteristics of LMFBR fuels (namely, high plutonium content, high heat load, and high content of fission products) can be accommodated by appropriate design. In the reference process, use is made of continuous, slab-shaped, fluidized-bed fluorination reactors (fluorinators). The continuous system minimizes plutonium inventory and permits operating conditions that promote high plutonium throughput. The slab shape eases the heat-removal problem (by providing high wall area-to-bed volume ratios) and provides geometric control of criticality.

The high content of volatile fission products in the fuel is accommodated by utilizing a "total containment" concept. Volatile wastes are converted to a solid waste form by sorption; rare gases are separated, compressed, and stored.

The process appears to be technically feasible since the techniques employed—continuous fluidized-bed fluorination, hexafluoride cold trapping, fractional distillation, and pneumatic conveying of solids—are basic to other nuclear and chemical processes. Additional development work would be needed to confirm the economic feasibility of the process.

An analysis of the reference process has defined a number of key problems, which are summarized briefly below and which could serve as a basis for developing an R&D program:

- 1) Mechanical decladding requires study because of possible difficulties stemming from the high rate of heat generation and the requirement that all fuel oxide be removed from the fuel hulls. A continuous ball mill for separation of fuel oxide from chopped fuel cladding segments represents an initial concept for study.
- 2) The continuous fluorination step will require development of reliable solids-feeding devices and unique equipment such as slab-shaped fluorinators and dual-stage reaction vessels. A requirement is that plutonium losses in the alumina waste from fluorination be low.
- 3) Further development and testing are needed to determine whether plutonium decontamination by the proposed process will meet requirements.
- 4) The preparation of mixed fuel oxides by direct fluidized-bed conversion of the mixed hexafluorides should

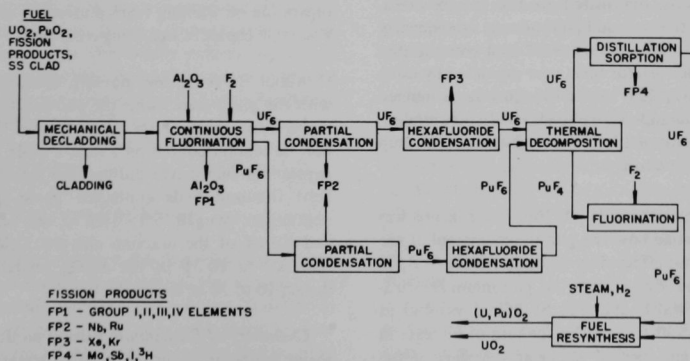


Fig. 1-5. Fluoride Volatility Process for Fast Breeder Reactor Fuels.



be studied on an engineering scale since work to date has been on separate conversion of  $\text{UF}_6$  to  $\text{UO}_2$  and  $\text{PuF}_6$  to  $\text{PuO}_2$ .

5) Total containment of radioactive and noxious off-gases, although not an essential requirement, is a highly desirable goal. Where possible, gases would be converted to low-volume solid or liquid form by appropriate reactions. This concept needs development.

6) Further work is needed to insure that criticality safety and containment of  $\text{PuF}_6$  will meet all requirements.

7) The role of sodium in the process and its possible effect on plutonium losses will require additional study, since it is known that  $\text{PuF}_6$  can be sorbed irreversibly on sodium fluoride.

Solutions to the above areas of uncertainty do not appear to be unduly difficult since much information is already available on which to base a program of research leading to an attractive and workable process. For this and other reasons brought out in the report of the conceptual design study, it is concluded that the fluoride volatility process is potentially attractive for application to short-cooled, high-performance fast breeder reactor fuels.

#### *b. Supporting Chemical Investigations*

*Fluorination of Simulated FBR Fuels in a 2-in.-dia Fluidized-bed Reactor.* Exploratory experiments have been carried out with simulated, oxidic FBR fuel in fluidized alumina beds to investigate the initial fluorination step of Fig. 1-5. A 2-in.-dia fluidized-bed reactor has been used to study the fluorination of fuels containing uranium, plutonium, and nonradioactive oxides of the fission product elements. Uranium is fluorinated to the volatile hexafluoride with dilute fluorine, and plutonium is subsequently fluorinated to the volatile hexafluoride with concentrated fluorine. Fast breeder reactor fuels were simulated by using a solid solution  $\text{UO}_2$ -20.0 wt %  $\text{PuO}_2$  powder combined with a mixture of nonradioactive oxides of fission product elements representative of LMFBR core fuel with a burnup of 100,000 MWD/metric ton.

A fractional factorial series of five experiments was performed to determine how the plutonium content of the final fluidized bed was affected by oxidation of the fuel, by the time-temperature sequence in the plutonium fluorination step (4 hr at 400°C and 4 hr at 550°C vs. 4 hr at 500°C and 4 hr at 550°C), and by the rate of increase in fluorine concentration (fast or slow) at the start of the plutonium fluorination step. For this series of experiments, neptunium was also added to the initial fluidized bed as

$\text{NpO}_2$  powder to determine how this fuel constituent would be distributed under the processing conditions used.

Plutonium concentration in the final fluidized-bed samples ranged from 0.09 to 0.21 wt %; these results correspond to 0.9-2.2% of the plutonium charged. The statistical evaluation of the results indicated that the plutonium content of the final bed can be reduced by using an oxidation step, by increasing the fluorine concentration quickly at the start of the plutonium-fluorination step, and by using 400°C rather than 500°C as the initial temperature in the plutonium-fluorination step. Two replicate experiments demonstrated that operating conditions can be chosen to reduce residual plutonium in the final fluidized bed to 1% or less of the plutonium charged.

The highest rates of plutonium fluorination were observed at the start of the plutonium-fluorination period. The average rate of production of  $\text{PuF}_6$  at 400°C was 2.2 lb/(hr)(ft<sup>2</sup>) with the reactor operating at an average of 53% of equilibrium for the reaction  $\text{PuF}_4(\text{s}) + \text{F}_2(\text{g}) \rightleftharpoons \text{PuF}_6(\text{g})$ . At 500°C, the average rate was 2.4 lb  $\text{PuF}_6$ /(hr)(ft<sup>2</sup>) at only 28% of equilibrium. An apparent activation energy of 8.6 kcal/mol was calculated from reaction-rate data as a function of temperature for this series of experiments and a series of experiments reported in ANL-7550, pp. 26-27.

In two of the runs, NaF traps used to collect the  $\text{UF}_6$  product in the uranium-fluorination step were taken off-stream as soon as fluorine was detected in the reactor off-gas. Analysis showed high U/Pu ratios (5280 and 3700) in the traps, thereby indicating good separation of uranium from plutonium. When excess fluorine was present in the off-gas in this step, signifying that most of the uranium had been fluorinated, plutonium was then also fluorinated from the fluid-bed reactor. These results show that an initial separation of uranium from plutonium can be obtained by a suitable choice of operating conditions.

About 1.7% of the uranium charged was fluorinated with the plutonium during the plutonium-fluorination step. Apparently, most of the molybdenum fluorinated during the uranium-fluorination step, while ruthenium and neptunium fluorinated during both fluorination steps. The final fluidized beds contained about 1 to 2% of the neptunium charged, 5 to 18% of the ruthenium charged, and  $\leq 0.1\%$  of the uranium charged. Calculations indicate that 6.9 to 10.3% of the  $\text{Al}_2\text{O}_3$  was converted to  $\text{AlF}_3$  during 10 to 20 hr of fluorination.

*Chemistry of Ruthenium.* Fission product ruthenium is a major contaminant in the product streams of the fluoride volatility process because ruthenium forms several volatile compounds containing fluorine and oxygen. The chemistry



of these ruthenium compounds is only poorly understood, and is complicated by the existence of a number of stable valence states of ruthenium and a variety of volatile compounds that are transformed to other volatile compounds under process conditions. Chemical and thermogravimetric studies indicated that the formation of volatile  $\text{RuO}_4$  by the reaction of  $\text{RuO}_2$  and oxygen is catalyzed by elemental fluorine. The thermal instability of  $\text{RuO}_4$  toward decomposition to  $\text{RuO}_2$  suggests that the reaction of the dioxide with fluorine-oxygen mixtures leads to a mixture of products consisting of the slightly volatile  $\text{RuF}_5$  and the very volatile  $\text{RuO}_4$  which, on heating, are converted to a mixture of  $\text{RuF}_5$  and nonvolatile  $\text{RuO}_2$ . The formation of these compounds is in agreement with the results of experiments on the decontamination of  $\text{PuF}_6$ .

*Decontamination of Plutonium Hexafluoride.* Bench-scale studies were carried out to test the proposed separation of ruthenium from plutonium hexafluoride by preferential condensation of ruthenium fluoride at  $-10^\circ\text{C}$ . If the only ruthenium species produced by fluorination of irradiated nuclear fuel is  $\text{RuF}_5$ , adequate separation of ruthenium from  $\text{PuF}_6$  at  $-10^\circ\text{C}$  is predicted because of the large difference in vapor pressures of the pure materials at this temperature. Mixtures of  $\text{PuF}_4$  and ruthenium metal were fluorinated, and the resulting gaseous mixture was passed through a cold trap at  $-10^\circ\text{C}$  and then through a cold trap at  $-78^\circ\text{C}$ . The quantities of ruthenium penetrating the  $-10^\circ\text{C}$  trap were small fractions of the total ruthenium, but nevertheless were greater by several orders of magnitude than the quantities that would have penetrated if the solid species in the trap had been  $\text{RuF}_5$  alone. Comparison of the quantities of ruthenium in the exit gas from the cold trap at  $-78^\circ\text{C}$  with the theoretical quantities for various ruthenium species (calculated from vapor pressures) indicated that the small, more volatile fraction may be  $\text{RuO}_4$ . The sources of oxygen for the formation of this compound are believed to be surface contamination of the equipment and a small amount of  $\text{RuO}_2$  present in the ruthenium metal. The tentative identification of the highly volatile ruthenium species as  $\text{RuO}_4$  is considered an important step in solving the problem of separating traces of ruthenium contaminant from plutonium hexafluoride.

## 2. Fluidization Technology

### a. Continuous-feed, Two-stage Reactor

Conceptual design studies of fluoride volatility processing plants for fast breeder fuels indicate that criticality as well as heat-removal considerations require fluorination reactors of slab-shaped design and approximately 4-in. thickness. To obtain information concerning the practical design and operation of continuous-solids-flow slab reactors of approximately this thickness, exploratory tests were

conducted, first on gas-distributor designs, then on mocked-up sections of Lucite slab reactors. In all tests, alumina was fluidized with air at ambient temperature.

Initial testing was performed with a 4-in.-square Lucite column having an inverted-pyramid-shaped gas inlet section (gas distributor) 3 in. deep. In tests with a 1/16-in. gas inlet, spouting occurred. However, a 7-in.-deep gas distributor with a 1/2-in.-dia gas inlet appeared to give good fluidization in this column. Some downward flow of solids was observed when a 1/2-in.-dia gas inlet was used at superficial gas velocities of about 1 ft/hr, indicating that continuous countercurrent flow of solids might be possible without the use of downcomer pipes, thereby simplifying design.

Continuous-solids-flow tests were performed with a two-stage column by adding another stage of 4-in.-square cross section above the original column. Each stage was 36 in. tall. The gas distributor for the upper stage was an inverted pyramid with the same nominal depth, 7 in., as the lower stage. The solids level in each stage was maintained constant by recycling solids from the lower stage to the upper stage via a pneumatic jet-conveyor device. A variable-position truncated-pyramid-shaped plug (1- by 1-in. base,  $2\frac{3}{4}$ -in. by  $2\frac{3}{4}$ -in. top,  $3\frac{1}{2}$ -in. height) was inserted at various positions above the orifice of the upper stage. Control of solids flow through a 1-in. orifice was achieved over the range 10 to 9000 lb/(hr)(ft<sup>2</sup>) by adjustment of plug location and gas flow rate.

A two-stage, slab-shaped, fluidized-bed column of 4-in. by 2-ft cross section and having six gas-inlet sections was mocked up of Lucite and tested qualitatively, i.e., solids flow and the quality of fluidization were observed. Downward flow of solids through the several gas orifices could not be stabilized, indicating the need for design improvement. Since relatively large openings are needed to allow solids to pass downward from the upper stage, insertion of a "priming" device (such as an auxiliary gas jet) in each opening may be needed.

A second two-stage, 4-in. by 2-ft Lucite column was fabricated which incorporated (1) a weir section for overflow of solids from the upper stage to the stage below, and (2) flat drilled-plate gas distributors. The stages were each 36 in. tall, and the downcomer section had a 4-in. by 4-in. cross section. Solids were continuously recycled from the lower to the upper stage by pneumatic conveying, simulating a continuous feed. With a gas velocity of 0.75 ft/sec, fluidization quality was good in both stages during 27 hr of operation. At this velocity, the perforated distributor plate performed well; few or no static bed regions were observed in either plate. Solids recirculation with a jet conveyor was good, as was solids movement from the upper stage to the lower stage via the downcomer. Slugging, observed in the

downcomer at this velocity, should be avoided in future designs.

Overall results indicate that fluidization quality and multistage contacting of gas and solids are satisfactory in slab-shaped, fluidized-bed reactors.

### *b. Dense-phase Transport of Granular Solids*

Dense-phase transport of granular solids through pipelines has a number of potential applications in the nuclear fuel cycle, e.g., in the handling of powdered nuclear fuels and particulate waste. This method of transporting powders through pipes differs from the conventional dilute-phase mode of pneumatic transport: in dense-phase transport, the solids are fed from a pressurized hopper and the solids-to-gas ratio is comparatively very high. Also, in dense-phase transport, velocities for solids and for gas are low, which may result in less attrition of solids and less erosion of piping than in dilute-phase transport.

Exploratory studies of the effects of motivating air pressure and discharge-orifice diameter on the transport rate of solids were conducted in an apparatus consisting of a 20-liter pressurized solids-feed vessel (hopper), a 3/8-in.-ID, 55-ft-long, polyethylene transport line with a discharge orifice, a solids-collection vessel, and gas-flow instrumentation. Discharge orifices were 3/32, 3/16, or 3/8 in. in diameter. Nominally 48-100 mesh alumina was the test solid.

The results at various operating conditions (summarized in Table I-2) show that higher pressures in the solids-feed vessel gave higher solids transport rates. Similarly, higher transport rates were achieved with greater diameters of the discharge orifice. Overall results show that this technique is applicable to the transport of particulate materials typical of those contemplated for use in fluoride volatility processes.

### *c. Pulsed-bed Studies*

Studies were continued on the pulsed-bed approach to fluidization (see ANL-7550, p. 32) as an alternative to conventional fluidized beds with steady upward flow of gas. (The latter is specified in the reference process design, Fig. I-5.) Pulsed beds are obtained by controlled,

intermittent upflow of gas through a bed of solid particles, causing the bed to expand; the bed contracts during the period when the gas flow is shut off. Additional data were obtained on bed expansion and pressure drop in pulsed beds by using four sizes of glass beads (average diameters of 73 to 580  $\mu\text{m}$ ) and 4-in.-OD, 1.25-in.-ID annular columns. The unique characteristics of pulsed beds, within the conditions studied,<sup>9</sup> were found to be:

1) Pressure-drop patterns for a given pulse cycle are reproducible.

2) Maximum pressure drop increases linearly as the pulsed-gas velocity is increased; "velocity" is the time-averaged value.

3) Bed-expansion ratio (maximum expanded bed height/static bed height) increases with (a) increasing gas velocity, (b) decreasing pulse frequency, and (c) decreasing fraction of on-period relative to off-period.

4) The characteristics of beds composed of large or heavy particles are more regular at a given set of pulsing conditions than are the characteristics of beds composed of small or light particles.

5) Good particle motion continues in a pulsed bed at average gas velocities lower than the velocity that would be the minimum fluidizing velocity if the bed were operated conventionally.

6) For pulsed-bed behavior to be fully controlled, the on-period should not exceed an upper limit that is equal to the time required for a gas bubble to form at the gas distributor and rise through the bed; nor should the off-period be below a lower limit equal to the time required for the bed to settle to its height at minimum fluidization. The bed-expansion ratio can be predicted from on-period, gas velocity, and minimum bubbling velocity.

The effects of pulsing conditions (gas velocity and on- and off-periods), particle properties (size, density, thermal conductivity, and heat capacity), gas properties (density, viscosity, and thermal conductivity), heater position, heater length, and static bed height on heat transfer from a concentrically located heater to a pulsed bed also have been studied for four sizes of glass beads, aluminum shot, and copper shot. Heat transfer in pulsed beds was superior to that in conventional fluidized beds for beds consisting of large or heavy particles and for a short heater or a heater located in the upper part of the bed.

A model was proposed for the heat-transfer mechanism in gas-solid particle systems. The proposed model was used

TABLE I-2. Operating Conditions and Results for Tests of Dense-phase Transport of Solids (nominally 48-100 mesh alumina)

Discharge-orifice diameter, in.	3/32	3/16	3/16	3/16	3/8
Motivating air pressure, psig	50.1	41.9	49.7	60	46.2
Air flow rate, cfm, at 70°F and 1 atm	0.042	0.02	0.042	0.088	0.042
Solids transport rate, g/min	167	127	238	694	329

to calculate heat-transfer coefficients from particle residence times and particle fluxes (measured from high-speed motion pictures) in both conventional fluidized beds and pulsed beds. Comparison of the calculated data with experimental heat-transfer data showed satisfactory agreement. The proposed heat-transfer-mechanism model can be used to estimate the heat-transfer coefficients in a pulsed bed.

#### *d. Basic Fluidization Studies*

The high rate of heat transfer at heating and cooling surfaces is probably the single most important property of fluidized beds. Despite the significance of this property and the relatively large effort expended in measuring fluidized-bed heat-transfer rates, correlations of heat-transfer coefficients have remained empirical and generally limited to the specific apparatus involved in the measurements.

As a first step in investigating the complex mechanism of heat transfer in a fluidized bed, the rate of heat transfer to the bed as a function of fluidized-particle residence time at a heater surface was considered. Two aspects of this problem were studied: (1) the case of infinite residence time of the particle (the bed at minimum fluidization with little or no particle motion) and (2) the case of finite residence time of the particle (the bed fluidized with particles in motion).

A model was proposed<sup>10</sup> which describes the rate of heat transfer from a heater to a bed of particles for gas flow through the bed equal to that required for minimum fluidization. It was assumed in this model that all of the heat is removed by the flowing gas. Predicted heat-transfer coefficients for both cylindrical and flat heaters were in good agreement with experimentally determined heat-transfer coefficients. It was also determined that the model adequately predicts heat-transfer rates for gas flows through the particle bed less than that required for minimum fluidization (packed-bed case).

Two other models were proposed for unsteady-state heat transfer from a wall to particles moving within a fluidized bed. One model was based on a bed of spheres in orthorhombic array, and a second, simplified model approximated a bed of spheres by a series of alternating slabs to represent the gas and solid phases of a fluidized bed. Numerical analyses showed good agreement between models. Good agreement between theory and experiment was also obtained.

#### *C. CONVERSION OF FBR OXIDE FUELS TO CARBIDE FUELS*

Studies of the use of a plasma-torch reactor for the conversion of FBR oxide fuel to carbide fuel have been

initiated. The current work is devoted to the conversion of uranium oxide to uranium monocarbide, but the process is expected to be applicable to the production of (U,Pu)C in equipment installed in an alpha-tight enclosure.

The method involves making small (~100 mesh), composite particles of uranium oxide and graphite, and reacting the oxide and graphite by passing the particles through and concurrently with the plasma flame of an inductively coupled plasma torch pointed downward. The product, in the form of small, free-flowing spheres of carbide and unreacted oxide and carbon, is collected in a product receiver at the bottom of the reactor. The CO reaction product is removed from the reaction chamber along with the inert plasma-forming gas.

The objective of the current work is to determine the operating conditions required to produce high yields of reactor-grade uranium monocarbide in order to assess the feasibility of a continuous production process using a plasma-torch reactor.

A 25-kW, inductively heated plasma-torch reactor has been installed (see Fig. 1-6). The equipment consists of four

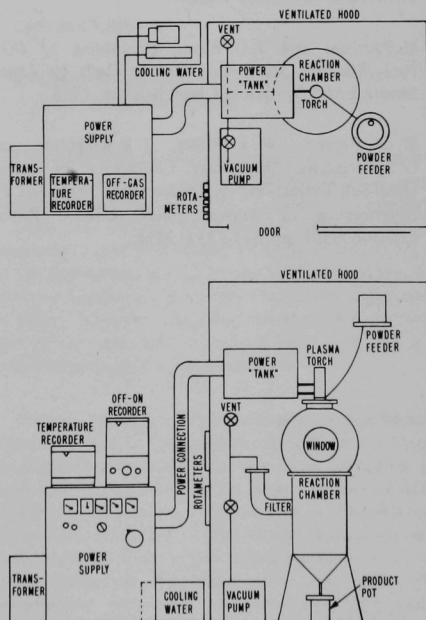


Fig. 1-6. Plasma-torch Installation for Studying the Conversion of Uranium Oxide to Uranium Carbide.

major parts: the plasma torch, the reaction chamber, the high-frequency power "tank" and power supply, and the powder feeder.

In preliminary experiments, uranium dioxide-graphite particles (containing 8.7 wt % carbon as opposed to 4.8 wt % carbon in UC) were fed into the plasma flame at 0.6 to 0.9 kg/hr. The carbon content of the effluent material from these experiments was 5.0 to 6.5 wt %. The

carbon content of the product was lower at higher power levels (20 kVA), with lower gas flow rates (132 scfh), and with higher hydrogen concentrations in the plasma gas (6 vol %). However, the oxygen content of the effluent material was nearly the same as that in the feed, indicating that the hot particles emanating from the torch might have reacted with atmospheric oxygen in the reaction chamber. Equipment improvements are under way to exclude oxygen and maintain an atmosphere of argon in the reaction chamber.

## REFERENCES AND FOOTNOTES

1. C. D. Watson *et al.*, "Head-End Processing of Spent LMFBF Fuel," in *Proceedings of 16th Conference on Remote Systems Technology*, pp. 19-38, American Nuclear Society, Hinsdale, Ill. (1969).
2. H. Dieckamp and L. H. Roddis, Jr., *The GPU/Al Demonstration Plant*, Nucl. News 11(7), 41 (1968).
3. N. M. Levitz *et al.*, *A Conceptual Design Study of a Fluoride Volatility Plant for Reprocessing LMFBF Fuels*, ANL-7568 (July 1969).
4. M. Payrissat and J. G. Wurm, *Decladding of UO<sub>2</sub>-PuO<sub>2</sub>/Stainless Steel Fast Reactor Fuels by Liquid Metals*, EAES Symposium, Mol, Belgium, 1968.
5. R. D. Pierce, W. E. Miller, J. B. Knighton, and G. J. Bernstein, "Multistage Contactors for Liquid Metal-Salt Extraction," in *Nuclear Metallurgy, Vol. 15, Reprocessing of Nuclear Fuels*, USAEC Report CONF-690801, pp. 511-533 (1969).
6. A total backmix stage is one in which the composition of all the material in the stage is uniform at any instant so that the material leaving the stage has the same composition as the material in the stage.
7. J. Fischer, *Glovebox Facility for Pyrochemical Research and Development Work with Plutonium-238*, ANL-7568 (May 1969).
8. N. M. Levitz *et al.*, *A Conceptual Design Study of a Fluoride Volatility Plant for Reprocessing LMFBF Fuels*, ANL-7583 (July 1969).
9. Fully reported in ANL-7592, a dissertation submitted by M. Kobayashi to the Graduate School of Northwestern University in partial fulfillment of the requirements for the degree of Doctor of Philosophy, Chemical Engineering.
10. J. D. Gabor, *Heat Transfer to Particle Beds with Gas Flows Less than or Equal to that Required for Incipient Fluidization*, Chem. Eng. Sci. (in press).

## II. SODIUM TECHNOLOGY

### A. INTRODUCTION

In July 1969, the ANL program in sodium technology was expanded. The major reason for assigning new sodium technology programs to ANL is the availability of EBR-II as a test facility. Advanced equipment and procedures that are being developed for subsequent LMFBRs will be proof-tested at EBR-II.

The ANL program contains work in the following areas:

1) *Sodium Chemistry.* Work in this area is aimed primarily at identification of species of impurity elements, reactions, and corrosion mechanisms—essentially to increase our understanding of the chemistry of liquid sodium. This is an ongoing program.

2) *Sampling and Analysis.* ANL is being made the center for the development of analytical methods for sodium. It does not have the sole responsibility for development of sodium analyses, but it does have the responsibility for establishing reference and standard analytical procedures, and for certifying them for national use. Development of sampling methods and equipment is a considerable part of this work.

3) *Sodium Purification and Monitoring.* At the maximum sodium temperature of about 600°C now being considered for LMFBRs, corrosion by sodium is probably within acceptable limits for "well-cold-trapped" sodium. On-line monitors are needed, however, to indicate system upsets and deterioration of sodium purity. Considerable attention is being given to improvement and testing of meters for monitoring oxygen, carbon, and hydrogen in sodium, and to the calibration of the meters in place.

4) *Fission Product Behavior and Control.* This area includes studies of the behavior of fission products in sodium, an assessment of the maintenance and shielding problems created by their presence, development of methods for their removal from sodium, development of on-line fission product monitors, and detection of fuel-cladding failures.

5) *Cover-gas Studies.* This includes work on the mechanism and control of aerosol formation in cover gases, and the monitoring of cover gases for hydrogen and fission product activities.

6) *Materials Compatibility.* Many problems fall within this area. Two being investigated at present involve the transfer of carbon in primary and secondary sodium systems and the evaluation of vanadium alloys as cladding

and structural materials for LMFBRs. Much of the materials compatibility work is carried out in the Materials Science Division and is not reported here.

### B. CHEMICAL DEVELOPMENTS

The chemistry program on liquid sodium is directed toward developing a sound scientific foundation for (1) understanding the behavior of sodium's common non-metallic contaminants (C, O, H, and N), (2) interpreting and evaluating existing corrosion data, and (3) predicting potential corrosion problems in reactor sodium systems. Of special interest therefore are the reactions of structural elements, such as iron and nickel, with elements that can enter metals interstitially, such as carbon, oxygen, hydrogen, and nitrogen. In this connection, the stability and solubility of carbon-bearing compounds believed to be important in the transport of carbon between steels are being determined, and the importance of surface diffusion in the corrosion of metals in sodium systems is being assessed. In addition, the solubility in sodium of potential reactor cover gases is being measured.

#### 1. Sodium Chemistry

##### a. Characterization of the Disodium Acetylide-Sodium System

One of the mechanisms proposed for the transport of carbon between steels in liquid-sodium systems involves disodium acetylide ( $\text{Na}_2\text{C}_2$ ).<sup>1</sup> Carbon is transported through the sodium by dissolved acetylide, which is presumed to have been formed by the interaction of carbon at the appropriate activity in the steel and sodium. In an effort to substantiate this model, the stability and solubility of  $\text{Na}_2\text{C}_2$  in sodium are being examined. A brief description of the experimental methods being used and of the preliminary findings is presented below.

*Stability of  $\text{Na}_2\text{C}_2$ .* The thermal stability of solid  $\text{Na}_2\text{C}_2$  (99.5% purity) is being studied by differential thermal-thermogravimetric analysis (under 1 atm of helium pressure) and by high-temperature X-ray powder diffraction. Differential thermal analysis revealed a reversible endothermic change at 275°C. This change was shown by the X-ray study to be associated with a transition of the solid from tetragonal (low-temperature) to cubic (high-temperature) symmetry. No other significant features appeared in the thermogram up to about 700°C, whereupon vaporization and consequent loss of sodium became significant.

X-ray patterns were obtained up to about 450°C. The cubic structure of the high-temperature modification of  $\text{Na}_2\text{C}_2$  persisted, suggesting that this compound is stable to at least 450°C. The X-ray study is being extended to higher temperatures to define better the limits of  $\text{Na}_2\text{C}_2$  stability. In addition, experiments to test the stability of the acetylide in the presence of sodium are planned.

**Solubility of  $\text{Na}_2\text{C}_2$  in Sodium.** An attempt is being made to measure the solubility of  $\text{Na}_2\text{C}_2$  in liquid sodium over the temperature range in which it is stable. The method involves equilibrating reactor-grade sodium with excess  $\text{Na}_2\text{C}_2$  at a preselected temperature, pressurizing a sample of the melt through a nickel-frit drain into a collector, dissolving the sample in water, and assaying the resulting off-gas for acetylene by gas chromatography. Preliminary results indicate that the acetylide ( $\text{C}_2^-$ ) content in sodium is about 10 ppm near 550°C and that this level is invariant over a period of at least 70 hr.

#### b. Studies of Surface Diffusivity

This study was undertaken to determine the importance of surface diffusion in the corrosion and transport of  $\alpha$ -iron in a liquid sodium environment. The technique employed is to observe by interference microscopy the development of grain-boundary grooves on polished  $\alpha$ -iron surfaces. Experiments are carried out at temperatures between 600 and 880°C. Preliminary data on groove profiles and on the kinetics of their development have been collected at 800°C. These data and their significance are discussed below.

**Groove Growth.** The kinetics of groove growth may be conveniently described in terms of the width of the groove,  $w$ , shown in the schematic drawing of a groove profile in Fig. II-1. In a liquid metal environment, there are two possible mechanisms for groove formation: surface diffusion of iron atoms along the solid-liquid interface and volume diffusion of iron atoms through either the bulk solid or the bulk liquid. Mullins<sup>2,3</sup> has shown that these two mechanisms lead to different grooving kinetics, namely,

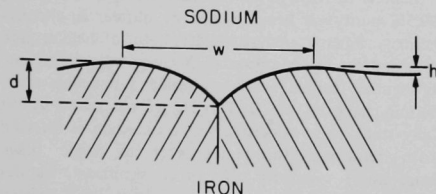


Fig. II-1. Schematic of Grain-boundary Groove Profile ( $w$  = width;  $d$  = depth;  $h$  = ridge height).

$$w = 4.6(Bt)^{1/4} \text{ for surface diffusion,} \quad (1)$$

$$w = 5.0(At)^{1/3} \text{ for volume diffusion,} \quad (2)$$

where  $B$  and  $A$  are constants at a given temperature and  $t$  is time.

Eight different  $\alpha$ -iron specimens were heated at 800°C for various times from 1 to 8 days. Many grooves on each specimen were examined. A typical interferogram is shown in Fig. II-2. The widest groove observed on each sample was selected for the kinetic analysis, and Fig. II-3 shows a log-log plot of the groove width versus time at temperature. The linear relationship between  $\log w$  and  $\log t$  was fit by the method of least squares. A slope of 0.22 with a standard deviation of 0.04 was obtained, in reasonable agreement with the exponent 0.25 that Eq. 1 indicates is appropriate for surface diffusion. Thus, surface rather than volume diffusion is indicated as the mechanism of mass transport responsible for groove formation.

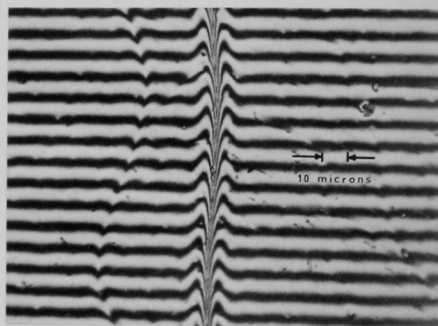


Fig. II-2. Interferogram of an  $\alpha$ -Iron Surface Annealed in Liquid Sodium at 800°C.

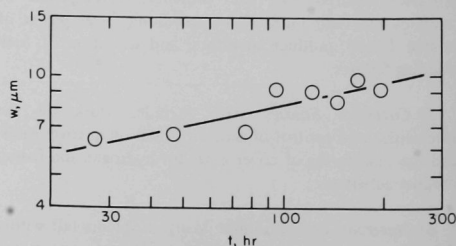


Fig. II-3. Maximum Groove Width Versus Time for  $\alpha$ -Iron in Liquid Sodium at 800°C.



Mullins' analysis of grain-boundary grooving showed that the parameter B in Eq. 1 is

$$B = D_{SL} \nu \gamma_{SL} \Omega^2 / kT, \quad (3)$$

where  $D_{SL}$  is the diffusion coefficient for iron-atom movement along the solid-liquid interface,  $\nu$  is the surface atom concentration of iron,  $\gamma_{SL}$  is the solid-liquid interfacial tension,  $\Omega$  is the atomic volume,  $k$  is the Boltzmann constant, and  $T$  is the absolute temperature. A surface diffusion coefficient of  $D_{SL} = 3 \times 10^{-6}$  cm<sup>2</sup>/sec is obtained from Eq. 3 by using the least-squares value  $B = 5.3 \times 10^{-21}$  cm<sup>4</sup>/sec and assuming  $\gamma_{SL} = 2000$  erg/cm<sup>2</sup>,  $\Omega = 7.8 \times 10^{-24}$  cm<sup>3</sup>/atom, and a bcc closest-packed surface plane with  $\nu = 2^{1/6} \Omega^{-2/3}$ . This result is larger than that obtained by Blakely and Mykura<sup>4</sup> in their study of  $\alpha$ -iron grooving in vacuum, namely,  $D_{SV} = 5 \times 10^{-7}$  cm<sup>2</sup>/sec at 800°C, and shows that surface diffusion of iron is enhanced by the liquid sodium environment.

**Groove Profile.** According to Mullins' theory, the profile of a grain-boundary groove formed by surface diffusion is different from one formed by volume diffusion. This difference is conveniently characterized by the relative ridge height of the groove,  $h/d$ , where  $h$  is the height of the groove ridge and  $d$  is the depth of the groove (see Fig. II-1). Allen<sup>5</sup> has shown that

$$h/d = 0.208 \text{ for surface diffusion}; \quad (4)$$

$$h/d = 0.149 \text{ for volume diffusion}. \quad (5)$$

Measurements of relative ridge height were made for 59 grooves on the specimens heated at 800°C. A histogram of the results is shown in Fig. II-4. The distribution has a maximum at  $h/d = 0.23$ , which agrees, within experimental error, with that expected for surface diffusion.

In summary, the preliminary findings at 800°C indicate that surface diffusion is an important mechanism in the corrosion of  $\alpha$ -iron by liquid sodium and that surface

diffusion proceeds more rapidly in a liquid sodium environment than in vacuum.

### c. Solubility of Helium in Liquid Sodium

Information on the solubility in sodium of potential cover gases is needed by reactor designers and engineers to evaluate the possibility that exsolution of gas in the coolant circuit could lead to cavitation and/or bubble formation, and thus result in diminished sodium flow. Of the three potential cover gases, argon,<sup>6</sup> nitrogen,<sup>7</sup> and helium, the solubilities in sodium of the first two have already been measured. The present study was undertaken to provide solubility data for helium.

The measurements with helium were carried out in the same apparatus previously used to measure the solubility of argon and nitrogen in sodium. The experimental procedure, adapted from a method due to Grimes *et al.*,<sup>8</sup> was as follows. Approximately 2.5 liters of cold-trapped sodium was saturated with <sup>3</sup>He-enriched helium gas in a stainless steel vessel (saturator) at a preselected temperature and pressure by circulating the gas through the metal for 2 hr. The saturated metal was allowed to stand overnight in the saturator at the same temperature and pressure. Approximately 2 liters of the equilibrated sodium was then transferred into another vessel (stripper) where the dissolved helium was stripped from the liquid sodium by sparging with an excess of recirculating argon. The argon-helium mixture in the stripper was then drawn by a Toepler pump through a liquid-nitrogen-cooled Molecular Sieve trap<sup>9</sup> into a calibrated bulb. Helium passed unadsorbed through the trap, whereas the argon was retained. The contents of the bulb were then assayed with a mass spectrometer. Helium-3 was included in the saturating gas to distinguish between soluble helium and helium that was introduced inadvertently during the stripping step as a contaminant of the argon.

The removal of argon by the Molecular Sieves concentrated the helium and thereby improved the analysis for helium. Tests were made to determine if helium was lost in this step. Known quantities of <sup>3</sup>He gas were introduced into the stripper, and the sequence outlined above, beginning with sparging, was carried out. The results of these tests, given in Table II-1, show that (a) 100% recovery of

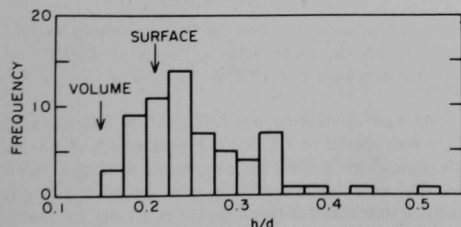


Fig. II-4. Relative Ridge Heights for  $\alpha$ -Iron in Liquid Sodium at 800°C.

TABLE II-1. Helium Recovery Tests

Helium-3 Injected into Stripper ( $\mu$ mol)	Helium-3 Recovered (%)
1.3	67 $\pm$ 7
4.8	84 $\pm$ 7
11.6	87 $\pm$ 5
22.6	100
56.4	100



helium was obtained when the total amount of helium in sodium exceeded  $20\text{ }\mu\text{mol}$ , and (b) below  $20\text{ }\mu\text{mol}$ , the recovery decreased rapidly with decreasing helium content. In the actual solubility measurements, helium recoveries ranged from 8 to 120  $\mu\text{mol}$ . For the few experiments (at 350 and 400°C) that yielded  $<20\text{ }\mu\text{mol}$  of helium, corrections were applied for partial recovery.

Solubilities were measured as functions of both pressure and temperature. The pressure dependence was determined from 14 experiments carried out at  $\sim 500^\circ\text{C}$  and at pressures ranging from 2 to 9 atm. Figure II-5 shows the variation of the mole-fraction solubility of helium (corrected to exactly  $500^\circ\text{C}$ ) with helium pressure. The experimental points were fitted by the method of least squares to a linear equation with a slope (the Henry's law constant  $K_H$ ) of  $1.56 \times 10^{-7}\text{ atm}^{-1}$ . On the basis of a statistical F-test made on the value of the intercept, the displacement of the line from the origin is insignificant. This can be seen in Fig. II-5 by the position of the 95% confidence limits. The solubility data, therefore, obey Henry's law.

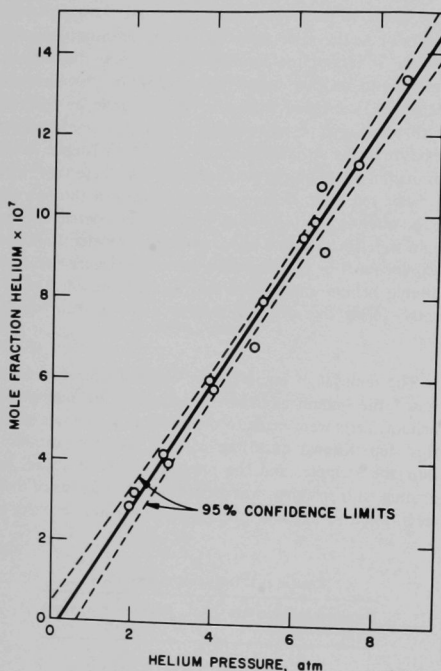


Fig. II-5. Pressure Dependence of the Solubility of Helium in Sodium at  $500^\circ\text{C}$ .

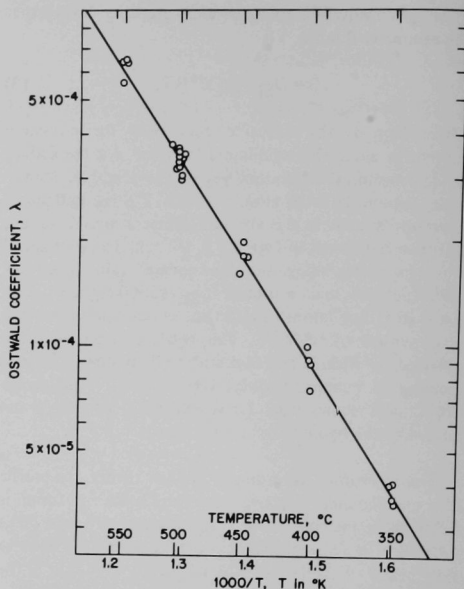


Fig. II-6. Temperature Dependence of the Solubility of Helium in Sodium.

The temperature dependence of the solubility was determined from about 30 experiments carried out at approximately 50-degree intervals between 350 and  $550^\circ\text{C}$ . The data, shown in Fig. II-6 in terms of the Ostwald coefficient  $\lambda$  (volume of helium dissolved per unit volume of sodium) and  $T$  in degrees Kelvin, were fitted by the method of least squares to a linear equation of the form  $\log \lambda$  vs.  $1/T$ . The regression line<sup>10</sup> in Fig. II-6 can be represented by

$$(350-550^\circ\text{C}) \log \lambda = 0.511 - 3070 T^{-1}. \quad (6)$$

Error analysis showed that at the 95% confidence level the deviation of the mean value of  $\log \lambda$  is  $\pm 0.015$ ; the corresponding error in  $\lambda$  is  $\pm 3.6\%$ .

The heat of solution was calculated by differentiating Eq. 6 with respect to  $1/T$ . For the standard state defined as one gram-atom of ideal gas compressed at temperature  $T$  into the molar volume of sodium at that temperature (a standard state useful in theoretical calculations), the heat of solution is  $14.1 \pm 0.6\text{ kcal/mol}$ . For the standard state defined as one gram-atom of ideal gas at one atmosphere pressure, the heat of solution is  $13.0 \pm 0.4\text{ kcal/mol}$ .

No reported experimental measurements of the solubility of helium in sodium exist with which to compare the present data. A theoretical model that satisfactorily accounts for the measured helium solubility, however, has been developed in this laboratory. A description of this theoretical work appears in Sect. V.A.1.d.

## C. ENGINEERING DEVELOPMENTS

### 1. Sodium Purification and Monitoring of Sodium Purity

Work has been initiated on the development, testing, evaluation, and improvement of purification devices and on-line monitors for impurities in sodium.

The initial studies of purification of sodium will include an evaluation of insoluble getters and hot traps for removal of hydrogen and oxygen, and possibly carbon and nitrogen. A program to obtain sound design criteria and improve operating procedures for cold-trap purifiers will begin in FY 1971.

On-line monitors for measuring the concentration of oxygen, carbon, and hydrogen are needed to study the chemistry of these impurities in sodium as well as to monitor their presence in LMFBF sodium coolant. The ability to detect abnormally high buildup of oxygen, carbon, or hydrogen in sodium is required so that corrective action may be taken to avoid excessive corrosion of reactor components. On-line hydrogen monitors are also needed in the secondary sodium system to detect small water leaks from the steam-generator tubes. Rapid detection would enable the reactor to be shut down before a leak propagates and causes widespread or catastrophic damage.

Monitors and monitoring systems (which include means for on-line calibration), after being fully tested and certified in the ANL Sodium Technology Program, will be proof-tested at EBR-II and other national test facilities.

#### a. Oxygen-activity Meter

The oxygen meter currently under test at ANL is the electrochemical cell developed by the United Nuclear Corp. (UNC). This meter is based on a galvanic cell having a  $\text{ThO}_2$ -15 wt %  $\text{Y}_2\text{O}_3$  solid electrolyte, a  $\text{Cu-Cu}_2\text{O}$  reference electrode, and a recommended operating temperature of 600°F (315°C). The cell develops a voltage dependent on the activity of oxygen in the sodium. Possible improvements in the cell, such as replacement of the  $\text{Cu-Cu}_2\text{O}$  reference electrode with  $\text{Na-Na}_2\text{O}$  or oxygen gas, are being studied at Brookhaven National Laboratory. As improvements are developed, they will be tested in the ANL program.

Two UNC electrochemical oxygen cells were tested and calibrated prior to shipment to EBR-II early in 1969. The cells were calibrated in the Sodium Analytical Loop (SAL). The calibration involved monitoring the steady-state cell output after various levels of oxygen were introduced into the loop by the decomposition of  $\text{NaOH}$ . Hydrogen from this decomposition was removed by gettering with zirconium. Prior to each addition of  $\text{NaOH}$ , oxygen was reduced to below 1 ppm by gettering with uranium. The technique of dip sampling and vacuum distillation was used to measure the  $\text{Na}_2\text{O}$  concentration.

The data yielded the following calibration equations relating oxygen concentration to cell voltage at 600°F:

$$\text{Cell TP-285 } \ln O(\text{ppm}) = 54.2 - 45.0 V,$$

$$\text{Cell TP-286 } \ln O(\text{ppm}) = 56.4 - 46.9 V,$$

where  $V$  is the cell output in volts. The theoretical value for the slope at 600°F is -39.4. The higher values (-45.0 and -46.9) observed experimentally cannot be accounted for at present. The cells were shipped to EBR-II, where they will be installed in the secondary sodium system.

Two other noncalibrated UNC cells have been operated in static sodium at EBR-II, one in a radiation field (cold-trap room), the other isolated from the radiation. Periodically, the placement of the cells is reversed to determine if measurable effects of radiation have taken place rather than normal drift or aging. To date, no effects of radiation have been observed. These results do not completely agree with earlier tests (possible with earlier cell models) at Atomic Power Development Associates in which significant radiation effects were noted occasionally.

Additional experience with long-term operation of the UNC oxygen cells in flowing sodium is needed as well as information on the effects of higher radiation levels. Therefore, plans are being made to test cells in the Radioactive Sodium Chemistry Loop (RSCL) that is being constructed for the EBR-II primary sodium system. These cells will be supplied by Brookhaven National Laboratory, and will be tested and calibrated at ANL-Illinois before installation on RSCL. On-line calibration techniques will also be developed at ANL-Illinois for use in these long-term tests. Two calibrated cells will be shipped to EBR-II in mid-1970 for testing in the RSCL. Additional calibrated cells will be supplied to EBR-II as required.

#### b. Carbon-activity Meter

Knowing the activity of carbon in LMFBF sodium is important to reactor operators since the strength of materials of construction and cladding can be adversely

affected by corrosion if the carbon activity is abnormally high. UNC has developed an on-line carbon-activity monitor that measures the flux of carbon diffusing through an iron membrane immersed in sodium at about 1400°F (760°C). The Chemical Engineering Division has one of the three carbon-activity meters made available by UNC for field testing. This meter will be tested to determine its reliability of operation and its response to the typical steady-state conditions (e.g., temperature and impurity levels) of EBR-II sodium as well as abnormal releases of carburizing agents into the sodium. For these experiments, the meter is being incorporated into the Test and Evaluation Apparatus (TEA), which is shown schematically in Fig. II-7.

TEA is constructed of type 304 stainless steel. It has a capacity of 40 to 50 lb of sodium and a maximum pumping rate of 8.5 gpm in the 1/2-in. schedule 40 pipe of the main loop, which is of welded construction for operation at temperatures up to 1200°F. There is an on-line distillation sampler (dip type) in the main loop and a freeze-line sampler in the purification loop. The response of the carbon-activity meter will be correlated with the rate of carburization of metal specimens mounted in a test section adjacent to the meter. During the course of these experiments, various changes in the design of the iron-membrane probe and the detector system will be tested in an effort to improve the meter.

Attempts to improve the meter are also being made by experiments in which probes are tested in sodium contained in stirred vessels. This type of equipment is also being used to determine meter response to various carbon-bearing species that may be important in carbon transport in sodium systems.

The most reliable model of the carbon-activity meter that is developed in this program will be prooftested at EBR-II in the Radioactive Sodium Chemistry Loop (RSCL). Methods of on-line calibration and of checking meter response to a sudden change in carbon activity will be developed by work with the TEA. Later, these methods will be incorporated into the operation of the carbon-meter station at RSCL.

### c. Hydrogen-activity Meter

Design and calculational studies are under way on an on-line monitoring system for hydrogen in sodium. Initial emphasis will be on the rapid detection of minute water leaks from the LMFBR steam-generator tubes into the secondary sodium. This enables the reactor to be shut down for repairs before such leaks propagate to adjacent tubes or become so large that catastrophic damage ensues. The main requirements for a leak indicator are sensitivity, rapid response, and reliability. It may be necessary to detect

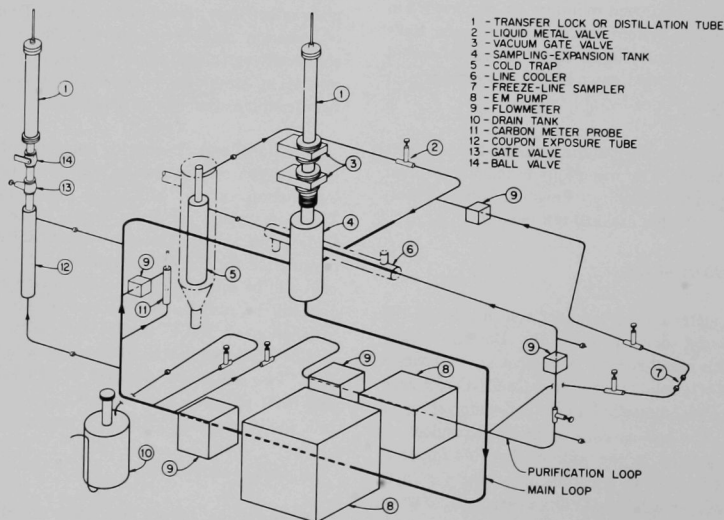


Fig. II-7. Test and Evaluation Apparatus (TEA).

changes in hydrogen concentration as small as 0.01 to 0.02 ppm within a fraction of a minute. The meter must be reliable since false indications of water leakage could result in unnecessary reactor shutdown.

Oxygen-activity meters could also be used for detection of water leaks into sodium. Such meters have fast response and high sensitivity, and may eventually be superior to hydrogen meters as leak detectors. However, oxygen meters are not yet well enough developed for use on large engineering systems.

To respond to the immediate needs of facilities using sodium-heated steam generators, the work on water-leak detection is being concentrated on development of an on-line hydrogen monitor similar to that used successfully at Electricité de France.<sup>11</sup> This simple, apparently rugged monitor is based on diffusion of the hydrogen in the sodium through a nickel membrane and detection of the hydrogen with a mass spectrometer. A vacuum is drawn at a steady rate on the membrane, thereby creating a hydrogen-activity gradient from the sodium side to the vacuum side and causing the hydrogen to diffuse. The partial pressure of hydrogen on the vacuum side, determined with the mass spectrometer, is a measure of the hydrogen flux through the membrane. A rapid increase in hydrogen flux through the membrane would be an indication of a water leak into the sodium.

Response rates for the nickel membranes used in such hydrogen meters have been calculated. These calculations indicate that for a 10-mil membrane at 500°C, the change in hydrogen flux on the vacuum side of the membrane will reach 70% of the total change in flux with 10 sec after a step change in the hydrogen concentration of the sodium.

Equipment for a hydrogen meter based on a nickel diffusion membrane and a mass spectrometer is being assembled and will be installed and tested on the SAL facility described above in Sect. II.A.2.

## 2. Fission Product Behavior and Control

Introduction into the sodium coolant of fission product activities from fuel elements and of activated corrosion products can lead to technical problems in LMFBR plant operation. Work to define these problems is under way, and includes calculational evaluations of the release rates and migration of fission products in the reactor sodium. Preliminary results of this continuing calculational study indicate the importance of investigating the behavior of

short-lived fission products. A model will be developed for computer programming to predict fission product concentrations and radiation levels throughout the reactor.

Experimental determinations of the transport and deposition of short-lived fission products in flowing sodium are being planned. The design and construction of a small experimental facility containing 1-2 gal of flowing sodium is being considered for these studies. The irradiation source has not been chosen yet. Gamma spectroscopy would be used in the identification of key isotopes. Since the presence of  $^{22}\text{Na}$  and  $^{24}\text{Na}$  from the irradiation of sodium would further complicate the already complex gamma spectra of mixed fission products, fuel targets will be irradiated while separated from the sodium and then quickly inserted into the flowing sodium.

This effort is expected to result in improved methods of detecting failed fuel elements, and of differentiating between innocuous leaks and serious failures that can propagate damage by restricting or stopping sodium flow.

## 3. Nature and Control of Formation of Sodium Aerosol

The objective of this work is to assess the magnitude of formation of sodium aerosol at proposed LMFBR conditions. Proposed LMFBR sodium temperatures during normal reactor operation range from about 425 to 650°C. The corresponding range of sodium vapor pressure is 0.73 to 52 Torr. In the pool-containment approach (used at EBR-II and proposed for LMFBRs), the cover gas is exposed to the full range of sodium temperatures.

The fraction of sodium vapor condensed to aerosol on cooling the sodium vapor-carrier gas mixture will depend on the ratio of thermal diffusivity to mass diffusivity in the mixture. High mass diffusivity will tend to promote direct condensation on the cooler surfaces above the sodium pool, whereas a low mass diffusivity will tend to promote aerosol formation within the cool gas-boundary layers. However, no experimental data on the diffusivity of sodium vapor have been found. For nonpolar simple gases, diffusivities may be estimated from viscosities; correlations for making such estimates for sodium are being examined.

The first experiments will be done in an inert-atmosphere glovebox. Sodium will be heated in a long tube cooled at one end, and an attempt will be made to view aerosol formation through a Pyrex window in the tube. The gas phase will be sampled and analyzed to determine the mass concentration of sodium aerosol.

## REFERENCES AND FOOTNOTES

1. C. Luner, H. M. Feder, and F. A. Cafasso, "Carbon Transport in Liquid Sodium," in *Proceedings of the International Conference on Sodium Technology and Large Fast Reactor Design*, ANL-7520, Part I, p. 455 (1968).
2. W. W. Mullins, *J. Appl. Phys.* **28**, 333 (1957).
3. W. W. Mullins, *Trans. Met. Soc. AIME* **218**, 354 (1960).
4. J. M. Blakely and H. Mykura, *Acta Met.* **11**, 399 (1963).
5. B. C. Allen, *Trans. Met. Soc. AIME* **236**, 915 (1966).
6. E. Veleckis, R. Blomquist, R. Yonco, and M. Perin, *Solubility of Argon in Liquid Sodium*, ANL-7325, p. 128.
7. E. Veleckis, K. Anderson, F. A. Cafasso, and H. M. Feder, "Solubilities of Nitrogen Gas and Sodium Cyanide in Liquid Sodium," *Proceedings of the International Conference on Sodium Technology and Large Fast Reactor Design*, ANL-7520, Part I, p. 295 (1968).
8. W. R. Grimes, N. W. Smith, and G. M. Watson, *J. Phys. Chem.* **62**, 862 (1958).
9. The trap consisted of a coiled copper tube filled with ~100 g of Linde Molecular Sieve Type 5A.
10. Equation 6 can also be expressed by  $\log \text{He solubility (ppb/atm)} = 5.08 - 2840 T^{-1}$ , with the atomic weight of natural helium taken as 4.003.
11. J. Birault, A. Brachet, E. Cambillard, J. Coron, L. Lannou, and C. Rault, "Detection of Small Leaks by Hydrogen Measurements in a Sodium-heated Steam Generator," *Proceedings of the International Conference on Sodium Technology and Large Fast Reactor Design*, ANL-7520, Part I, p. 345 (1968).

### III. MATERIALS CHEMISTRY AND THERMODYNAMICS

#### A. HIGH-TEMPERATURE THERMODYNAMIC STUDIES

The objective of this program is to obtain phase-diagram, thermodynamic, and chemical data that can be used to interpret and evaluate performance of fast-breeder-reactor fuels. This information will aid in understanding and in selecting methods for control of fission product distribution in the fuel, cladding attack by corrosive fission products, plutonium segregation, and fuel swelling. In addition, these data will help to identify phases formed in fuel under operating conditions and to choose additives for controlling the chemical potentials of fuel anions and those fission products that are deleterious to prolonged fuel-pin lifetimes. The high-temperature investigations of the U-Pu-O and U-Pu-C fuel systems include mass-spectrometric vapor-pressure measurements, phase-diagram studies, and activity measurements by transpiration.

##### 1. Volatilization Studies of Plutonium Compounds by Mass Spectrometry

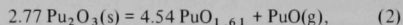
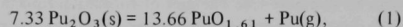
###### a. Pu-O and U-Pu-O Systems

Mass-spectrometric studies of the volatilization behavior of the Pu-O system are nearly complete. Measurements of the Pu-U-O system have been initiated. The purpose of these studies is to determine (1) the composition of the vapor phase in equilibrium with the condensed phase(s), (2) the partial pressures of the vapor species as a function of temperature, and (3) the thermodynamic properties of the vapor species and condensed phases.

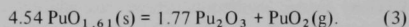
To determine the heats of formation of  $\text{PuO}_2(\text{g})$  and  $\text{PuO}(\text{g})$ , the vapor pressures have been measured over three condensed-phase compositions: (1) single-phase  $\text{PuO}_{1.83}(\text{s})$  where congruent effusion apparently occurs; (2) two-phase  $\text{PuO}_{1.61}(\text{s})\text{-Pu}_2\text{O}_3(\text{s})$ , and (3) two-phase  $\text{Pu}_2\text{O}_3(\text{s})\text{-Pu}(\ell)$ . The results of the  $\text{PuO}_{1.83}$  and  $\text{PuO}_{1.61}\text{-Pu}_2\text{O}_3$  measurements were previously reported (see ANL-7550, p. 35).

However, additional measurements have now been made over  $\text{PuO}_{1.61}\text{-Pu}_2\text{O}_3$  to extend the temperature range for detection of  $\text{PuO}_2(\text{g})$  [the  $\text{PuO}_2$  pressure is considerably lower than that of  $\text{PuO}(\text{g})$  and  $\text{Pu}(\text{g})$  over  $\text{PuO}_{1.61}(\text{s})\text{-Pu}_2\text{O}_3(\text{s})$ ].

The pressures over  $\text{PuO}_{1.61}\text{-Pu}_2\text{O}_3$  have been measured mass spectrometrically for the reactions



and

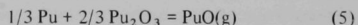


The enthalpies of reaction for Reactions 1 and 2, obtained from a numerical average of all the data, differ insignificantly from the values reported in ANL-7550. For Reaction 3, an enthalpy of reaction of  $132.0 \pm 4.4$  kcal/mol was obtained from an average of four values; this differs considerably from the previously reported value ( $126.2 \pm 4.9$  kcal/mol) obtained from the first experiment.

Preliminary results of the  $\text{Pu}_2\text{O}_3(\text{s})\text{-Pu}(\ell)$  vaporization experiments yielded heats of vaporization for the reactions



and



of 76.3 kcal/mol Pu and 106.7 kcal/mol PuO, respectively. Some further work is planned to verify the heats and entropies for Reactions 4 and 5.

The results of this study may be used to calculate provisional free energies of formation for  $\text{PuO}_2(\text{g})$  and  $\text{PuO}(\text{g})$ . Free energies of vaporization for each of the three condensed-phase compositions are given in Table III-1.

TABLE III-1. Free Energy of Vaporization from Plutonium Oxides

Condensed Phase	Author	Gaseous Phase	$\Delta G$ or $\Delta \bar{G}$ (cal/mol)	$\Delta G_{2000}$ or $\Delta \bar{G}_{2000}$ (cal/mol)
$\text{PuO}_{1.92}$	AFR <sup>1</sup>	$\text{PuO}_2$	$135600 \pm 1300^a - (31.8 \pm 0.7)T$	65400
$\text{PuO}_{1.83}$	This Research	$\text{PuO}_2$	$138800 \pm 1000 - (35.6 \pm 0.5)T$	67600
	This Research	$\text{PuO}$	$127200 \pm 2700 - (30.7 \pm 1.2)T$	65800
$\text{Pu}_2\text{O}_3\text{-PuO}_{1.61}$	AFR <sup>1</sup>	$\text{PuO}$	$127100 \pm 2500 - (37.0 \pm 1.2)T$	53100
	This Research	$\text{PuO}_2$	$132000 \pm 4400 - (28.0 \pm 2.2)T$	76000
	This Research	$\text{PuO}$	$118400 \pm 1000 - (32.7 \pm 0.5)T$	53000
	This Research	$\text{Pu}$	$110000 \pm 1700 - (24.0 \pm 0.9)T$	62000
$\text{Pu}(\ell)\text{-Pu}_2\text{O}_3$	This Research	$\text{PuO}$	$106200 \pm 2000^b - (29.5 \pm 1.0)T$	47200
	This Research	$\text{Pu}$	$76300 \pm 2600^b - (19.9 \pm 2.0)T$	36500

<sup>a</sup>Uncertainties are standard deviation.

<sup>b</sup>Estimated uncertainty.



These free energies are compared with those computed by Ackermann, Faircloth, and Rand (AFR)<sup>1</sup> from their measurements of total pressure. [They assumed that the gas over  $\text{PuO}_{1.92}$  is essentially all  $\text{PuO}_2(\text{g})$  and that over  $\text{Pu}_2\text{O}_3\text{-PuO}_{1.61}$  is all  $\text{PuO}(\text{g})$ .]

Partial molar free energies of oxygen and plutonium were calculated for each region from the plutonium pressures, oxide pressures, and the free energy of formation of  $\text{PuO}_2(\text{s})$ .<sup>2</sup> These partial molar quantities were used in turn to compute free energies of formation for  $\text{PuO}(\text{g})$  and  $\text{PuO}_2(\text{g})$ . Our values for  $\text{PuO}(\text{g})$  and  $\text{PuO}_2(\text{g})$  are compared with those of AFR in Table III-2. This table also contains other thermodynamic quantities for the Pu-O system. The AFR data are based on measurements<sup>3</sup> of oxygen over Pu-O by an emf method, which we have adjusted to more recent  $\Delta G_f^\circ(\text{PuO}_2)$  values.<sup>2</sup> Whereas our slopes and intercepts in the equations for the partial molar free energies of oxygen and plutonium over two-phase  $\text{Pu}_2\text{O}_3\text{-PuO}_{1.61}$  differ considerably from those of AFR, the free energies calculated at 2000°K are in reasonably good agreement.

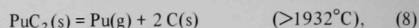
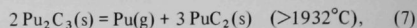
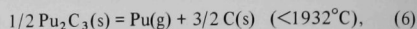
#### b. Pu-C System

As part of an investigation of the thermodynamic properties of mixed carbides, the volatilization behavior of the plutonium carbides has been investigated by combined mass-loss and mass-spectrometric Knudsen effusion studies. In particular, attention was focused on the univariant condensed systems  $\text{Pu}_2\text{C}_3 + \text{C}$ ,  $\text{PuC}_2 + \text{C}$ , and  $\text{Pu}_2\text{C}_3 + \text{PuC}_2$ . Preliminary results obtained for the condensed systems  $\text{Pu}_2\text{C}_3 + \text{C}$  and  $\text{Pu}_2\text{C}_3 + \text{PuC}_2$  were previously reported (see ANL-7550, p. 37). The investigation of the three condensed systems noted above has now been completed, and a paper entitled "A Mass-Spectrometric Study of the Volatilization Behavior in the Plutonium-

Carbon System"<sup>4</sup> has been written. A summary of this study follows.

Our mass-spectrometric analysis of the vapor phase in equilibrium with the solid mixtures  $\text{Pu}_2\text{C}_3 + \text{C}$ ,  $\text{Pu}_2\text{C}_3 + \text{PuC}_2$ , and  $\text{PuC}_2 + \text{C}$  in the temperature ranges 1579 to 1933°K, 1933 to 2299°K, and 1933 to 2348°K, respectively, showed that  $\text{Pu}(\text{g})$  was the predominant vapor species.

From considerations of the mass-spectrometric data, X-ray diffraction, and chemical analyses of sample residues, and a phase diagram, we have concluded that vaporization of  $\text{Pu}(\text{g})$  occurs primarily by the following reactions:



although the exact composition of each of the condensed phases is unknown.

The enthalpies of reaction for the three reactions were determined by the second-law method from mass-spectrometric measurements of the ion intensity of  $\text{Pu}^+$  as a function of temperature. Mass-effusion rates were used to determine vapor pressures and these, combined with the slopes derived from the temperature-dependence data, were used to evaluate the intercepts. The following equations for the vapor pressures as a function of temperature were derived for Reactions 6, 7, and 8, respectively:

$$R \ln P = -\frac{97590 \pm 1080}{T} + 20.6 \pm 0.64; \quad (9)$$

TABLE III-2. Thermodynamic Properties of Plutonium-Oxygen System

Phase and Composition	Author	Free Energy of Formation or Partial Molar Free Energy Equation (cal/mol)	$\Delta G_{2000}^\circ$ or $\Delta \bar{G}_{2000}^\circ$ (cal/mol)
$\text{PuO}_2(\text{s})$	See Ref. 2	$\Delta G_f^\circ = -244200 + 41.4T$	-161400
$\text{PuO}_{1.92}(\text{s})$	AFR <sup>1</sup>	$\Delta \bar{G}_{\text{O}_2}^\circ = -225000 + 76.1T$	-72800
	AFR <sup>1</sup> Revised <sup>a</sup>	$\Delta \bar{G}_{\text{Pu}}^\circ = -18400 - 35.6T$	-89600
$\text{PuO}_{1.83}(\text{s})$	This Research	$\Delta \bar{G}_{\text{O}_2}^\circ = -199700 \pm 8000 + (48.2 \pm 4.0)T$	-103300
	This Research	$\Delta \bar{G}_{\text{Pu}}^\circ = -44500 \pm 8000 - (7.5 \pm 4.0)T$	-59500
$\text{Pu}_2\text{O}_3(\text{s})\text{-PuO}_{1.61}(\text{s})$	AFR <sup>1</sup>	$\Delta \bar{G}_{\text{O}_2}^\circ = -183500 + 21.6T$	-140300
	AFR <sup>1</sup> Revised <sup>a</sup>	$\Delta \bar{G}_{\text{Pu}}^\circ = -57400 + 14.5T$	-28400
	This Research	$\Delta \bar{G}_{\text{O}_2}^\circ = -203700 \pm 5500 + (29.0 \pm 2.8)T$	-145700
	This Research	$\Delta \bar{G}_{\text{Pu}}^\circ = -33700 \pm 3100 + (4.1 \pm 1.6)T$	-25500
$\text{Pu}(\ell)\text{-Pu}_2\text{O}_3(\text{s})$	This Research	$\Delta \bar{G}_{\text{O}_2}^\circ = -248600 \pm 9600 + (34.5 \pm 4.9)T$	-179600
	This Research	$\Delta \bar{G}_{\text{Pu}}^\circ = 0$	0
$\text{PuO}_2(\text{g})$	AFR <sup>1</sup> Revised <sup>a</sup>	$\Delta G_f^\circ = -107800 + 5.4T$	-97000
	This Research	$\Delta G_f^\circ = -105400 \pm 3500 + (5.1 \pm 1.7)T$	-95200
$\text{PuO}(\text{g})$	AFR <sup>1</sup> Revised <sup>a</sup>	$\Delta G_f^\circ = -22000 - 11.7T$	-45400
	This Research	$\Delta G_f^\circ = -17500 \pm 3500 - (13.5 \pm 1.8)T$	-45300

<sup>a</sup>AFR data adjusted to more recent  $\Delta G_f^\circ(\text{PuO}_2)$  values.<sup>2</sup>



$$R \ln P = -\frac{118720 \pm 1080}{T} + 31.6 \pm 0.64; \quad (10)$$

$$R \ln P = -\frac{88290 \pm 540}{T} + 15.8 \pm 0.41. \quad (11)$$

The eutectoid temperature, i.e., the temperature at which  $\text{Pu}_2\text{C}_3(\text{s})$ ,  $\text{PuC}_2(\text{s})$ , and  $\text{C}(\text{s})$  are in equilibrium, was estimated to be 1932°K by averaging four values for the intersection of the plutonium vapor pressure curves. This agrees with the value of 1933  $\pm$  15°K estimated by Reavis.<sup>5</sup>

The enthalpy and entropy of formation of  $\text{Pu}_2\text{C}_3(\text{s})$  from the elements were evaluated at the reference temperature 298°K by combining vapor-pressure data with  $H_T^\circ - H_{298}^\circ$  and  $S_T^\circ - S_{298}^\circ$  data. The values are  $\Delta H_{298}^\circ = -32.28 \pm 2.20$  kcal/mol and  $\Delta S_{298}^\circ = +10.18 \pm 1.20$  eu.

The enthalpy of formation of  $\text{Pu}_2\text{C}_3$  calculated from this research is compared with literature<sup>6-9</sup> values in Table III-3. Good agreement with the average of the experimental values (excluding that of Huber and Holley) is evident. However, it is evident from the range of values that definitive measurements of the heat of combustion would be desirable.

## 2. Phase Diagram of the Uranium-Plutonium-Oxygen System

The dominant feature of the U-Pu-O ternary phase diagram<sup>10</sup> is the existence of a fluorite solid-solution phase field which extends across the diagram from the uranium-oxygen side to the plutonium-oxygen side. The hypostoichiometric boundary of this phase field at elevated temperatures, although of considerable interest in the field of fast-reactor fuels, had not been established except at the two sides of the diagram. The establishment of this boundary was chosen as the major goal of our study of the U-Pu-O system. To establish the hypostoichiometric boundary of the ternary phase [i.e.,  $(\text{U}_{0.8}\text{Pu}_{0.2})\text{O}_{2-x}$ ], alloys of uranium and plutonium were equilibrated with U-Pu oxide crucibles. Crucibles were prepared from mixed-oxide powder [ $U/(U + \text{Pu}) = 0.198$ ] by pressing in a 0.50-in. die at 51,000 psi. In order to avoid contamination, no binder or die lubricant was used. The crucibles were sintered for one hour in vacuum at 1370°C followed by

4 hr in helium at 1685°C. The uranium-plutonium alloys were prepared by melting uranium with portions of a 40 at. % U-60 at. % Pu alloy in an arc furnace on a water-cooled copper hearth. The equilibration between alloys and crucibles was carried out in a tungsten resistance furnace in a helium atmosphere. The average charge in one of these experiments was 5.5 g, about 2.3 g of alloy and a 3.2-g crucible.

The equilibration tests were carried out at constant temperature. After cooling, the products were mounted in a cold-setting resin, sectioned with a 10-mil diamond saw, polished, and then examined metallographically. Many similarities to comparable products from equilibrations of uranium with uranium dioxide crucibles were apparent. Oxide growths had formed between the alloys and the crucibles. Numerous metallic particles were observed in both the crucibles and the oxide growths; the particles were primarily located at grain boundaries of the fluorite oxide phase. Apparently, the oxide crucible and the oxide growth had both been single-phase fluorite oxide at the temperature of the equilibration, and the metallic particles, identified by electron-probe microanalysis (EPM) as U-Pu alloys, had precipitated during cooling to room temperature.

Examination of crucibles and alloys after initial equilibration, using electron-probe microanalysis, showed that the  $\text{Pu}/(\text{Pu} + \text{U})$  ratios in the alloy and in the oxide crucibles were different. Further experiments and analysis revealed that the  $\text{Pu}/(\text{Pu} + \text{U})$  ratio was 0.1 in the metal alloy equilibrated with the metal-rich oxide having a  $\text{Pu}/(\text{Pu} + \text{U})$  ratio of 0.2. This relation was found to be nearly independent of temperature in the range from 1588 to 2215°C. Since the plutonium ratios are lower in the alloy than those in the oxide, the oxide growing between the alloy and crucible as the alloy reacts with the crucible forms with a decreasing plutonium gradient (from crucible to alloy) and an increasing uranium gradient. This will occur whether the initial alloy has more or less plutonium than that in equilibrium with  $(\text{U}_{0.8}\text{Pu}_{0.2})\text{O}_{2-x}$ . Thus, the initial reaction produces an oxygen-depleted crucible separated from the U-Pu alloy by an oxide of variable plutonium and uranium concentration. To be certain that the oxide crucible and alloy are in equilibrium, a second-stage equilibration is performed after replacing the oxide growth and alloy with an alloy of equilibrium composition, i.e.,  $\text{Pu}/(\text{Pu} + \text{U}) = 0.1$ .

The results of six phase-boundary measurements of  $(\text{U}_{0.802}\text{Pu}_{0.198})\text{O}_{2-x}$  are shown in Fig. III-1. The phase boundary of  $\text{UO}_{2-x}$  is also shown for comparison. The 20% plutonia-80% urania hypostoichiometric boundary contains less oxygen than  $\text{UO}_{2-x}$ , being 0.17 to 0.20 O/M units lower in the temperature range of our study.

TABLE III-3. Heat of Formation of  $\text{Pu}_2\text{C}_3$

Author	$\Delta H_{298}^\circ(\text{Pu}_2\text{C}_3)$ (kcal/mol)
Olsen and Mulford <sup>6</sup>	-24.6, -27.4 <sup>a</sup>
Harris, Phillips, Rand, and Tetenbaum <sup>7</sup>	-34.6
Lapage <sup>8</sup>	-42
Huber and Holley <sup>9</sup>	+3.4
This Research	-32.3

<sup>a</sup>Calculated from  $\text{Pu}_2\text{C}_3\text{-C}$  and  $\text{PuC-Pu}_2\text{C}_3$  regions, respectively.

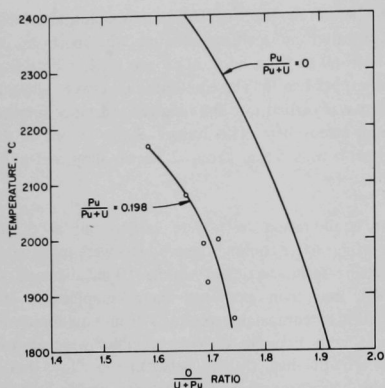


Fig. III-1. Hypostoichiometric Boundary of the Fluorite Phase in the U-Pu-O System at High Temperatures.

### 3. Equilibrium Studies of Uranium-Fission Product-Oxygen Systems

The objective of this study is to obtain, for the chemical interactions among fast breeder reactor fuel, its fission products, and the cladding material, thermodynamic data which may be useful in designing a fuel system having a suitably long lifetime.

Analyses of irradiated fuels suggest that iodine, which can penetrate the grain boundary of stainless steel (see Sect. IV.A of this report), is closely related to the corrosion of the cladding. In connection with this possible interaction of stainless steel and iodine, a preliminary examination was carried out by chemical-transport experiments and by thermodynamic calculations. Although it was found that iodine vapor will transport iron (by the Van Arkel process) from stainless steel against a temperature gradient, it seemed unlikely that free iodine would be available for such a transport in the presence of fission product cesium, which should form stable CsI. However, it was also found experimentally that free iodine was released (observed visually) from CsI and  $\text{UO}_2+x$  at about 900°C when  $x \geq 0.18$  (the lowest value of  $x$  yet studied). The released iodine attacked stainless steel extensively, but did not transport iron efficiently. When transport did not occur, an unidentified white deposit was observed.

A plausible explanation for these observations is as follows. A ternary Cs-U-O compound may form which is stable enough to cause the release of iodine from CsI. Under the high oxygen potential over  $\text{UO}_{2.18}$ , the iodine will attack stainless steel and form an Fe-O-I compound instead of  $\text{FeI}_2$ , which is essential in the transport of iron.

This model, which assumes that  $\text{Cs}_2\text{O}$  can be stabilized by the formation of a ternary compound with  $\text{UO}_{2+x}$ , provides a feasible explanation for the observation that there is cesium in the center of the irradiated fuel where the temperature is much higher than the boiling point of either CsI or  $\text{Cs}_2\text{O}$ . There is also evidence (see ANL-7550, p. 51) that similar stabilization of  $\text{Cs}_2\text{O}$  can proceed through the formation of a compound such as  $\text{Cs}_2\text{O-Al}_2\text{O}_3$ . ( $\text{Al}_2\text{O}_3$  has been observed as an impurity in irradiated fuels.)

The work that has been carried out thus far has been helpful in constructing a model for the corrosion of the cladding by the fission products. However, it is evident that additional work is necessary to further the understanding of the Cs-U-O system and, in particular, the thermodynamic properties of its ternary compounds. More experiments are being planned to determine the thermodynamic properties of the Cs-U-O system.

### 4. Transpiration Studies of the Uranium-Carbon System

The study of the vaporization behavior of the uranium-carbon system (see ANL-7550, p. 40) is nearly complete. Measurements of the total pressure of uranium-bearing species and carbon activity are being made as functions of temperature and  $\text{UC}_x$  composition, using the transpiration method with hydrogen-methane mixtures as carrier gases. Emphasis has been placed on measuring carbon activities in the uranium-carbon system. These measurements will ultimately be extended to the plutonium-carbon and U-Pu-C systems. The effects of oxygen as an impurity, as well as fission product carbides, on carbon activity in these systems will also be considered.

The results of the latest measurements of carbon activity as functions of  $\text{UC}_x$  composition at 2155, 2255, 2355, and 2455°K are shown in Fig. III-2. The plateaus of the 2155,

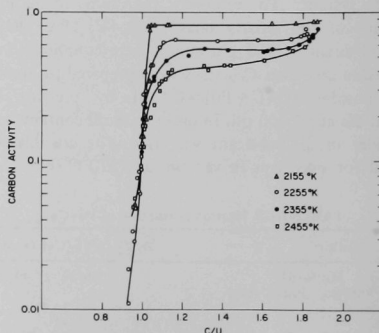


Fig. III-2. Activity of Carbon as a Function of Composition.

2255, and 2355°K isotherms are consistent with the miscibility gap ( $UC + \beta UC_2$ ) shown by the phase diagram proposed by Storms<sup>11</sup> for the uranium-carbon system. Over the composition range investigated at 2455°K, the shape of the carbon activity curve is typical of bivalent behavior and is also consistent with the phase diagrams, which show a single-phase region above the miscibility gap, with a critical temperature of  $\sim 2100^\circ\text{C}$  ( $\sim 2373^\circ\text{K}$ ) at  $C/U = 1.3$ .

Free energies and heats of formation were calculated from our carbon-activity measurements shown in Fig. III-2, the adjusted uranium vapor pressure values of Storms,<sup>11</sup> and 126.3 kcal/mol as the heat of vaporization of uranium.<sup>12</sup> Heat of formation values (at 298°K) were estimated from the calculated free energy of formation values and the known free energy functions<sup>11,13</sup> for  $U(\ell)$ ,  $UC_{1.00}(s)$ , " $UC_2$ "(s), and graphite. The  $\Delta[(G_T^\circ - H_{298}^\circ)/T]$  values for  $UC_X$  compositions were interpolated on the assumption that a linear relationship exists for these values between  $UC_{1.00}$  and  $UC_{1.93}$ .

The average heats of formation of  $UC_{1.00}$  and  $UC_{1.85}$  are  $-22.6 \pm 0.5$  and  $-23.7 \pm 1.0$  kcal/mol, respectively. The value chosen by the Vienna Panel<sup>14</sup> for  $UC_{1.00}$  is  $-21.7 \pm 1.0$  kcal/mol; for  $UC_{1.91}$ , the value of  $-23 \pm 2$  kcal/mol was adopted. A more recent value of  $-23.2 \pm 1.0$  kcal/mol was estimated for  $UC_{1.00}$  by Storms and Huber;<sup>15</sup> they obtained values of  $-23.2 \pm 0.9$  and  $-23.0 \pm 1.0$  kcal/mol for the heats of formation of  $UC_{0.996}$  and  $UC_{1.032}$ , respectively, from combustion measurements.

## B. STUDIES OF REACTOR SAFETY AND PHYSICAL PROPERTIES

The primary objective of these studies is to provide data about physical properties at high temperatures for use in evaluating the safety of various prospective fast-breeder-reactor materials. It is expected that these data obtained at temperatures above normal operating conditions can be suitably extrapolated to the very high temperatures involved in accident situations. In addition, physical-property data in support of other Divisional programs are being obtained.

### 1. Enthalpies and Heat Capacities by Drop Calorimetry

#### a. Resistance-heated Calorimetric System

As a check on the accuracy of the resistance-heated drop-calorimetric system, enthalpy measurements were made of standard sapphire crystals obtained from the National Bureau of Standards. The resulting data over the temperature range from 472 to 1334°K agree quite well

with the results of other laboratories and can be represented by the following equation:

$$(H_T^\circ - H_{298.15}^\circ) = 27.6002 T + 1.61393 \times 10^{-3} T^2 + 9.65836 \times 10^5 T^{-1} - 11554.31 \text{ (cal/mol).} \quad (12)$$

Enthalpies were determined for  $Na_3Bi$ , a material of interest in the program on energy conversion. For solid  $Na_3Bi$  over the range from 488 to 1095°K, the data can be represented by the equation

$$(H_T^\circ - H_{298.15}^\circ) = 1.86638 \times 10^2 T - 0.238758 T^2 + 1.04442 \times 10^7 T^{-1} + 4.29343 \times 10^{-3} T^{5/2} - 73500.95 \text{ (cal/mol).} \quad (13)$$

In the liquid range from 1135 to 1227°K, the data can be represented by the linear expression

$$(H_T^\circ - H_{298.15}^\circ) = 41.6431 T - 13942.38 \text{ (cal/mol).} \quad (14)$$

The standard deviations for Eqs. 13 and 14 are 26 and 38 cal/mol, respectively. Extrapolation of these equations to 1123°K, the melting temperature of  $Na_3Bi$ , yielded an apparent heat of fusion of 7085 cal/mol (see Fig. III-3).

Enthalpies of  $UO_{2.005}$  (referred to 298.15°K) were determined over the range from 675 to 1450°K. The data are being analyzed.

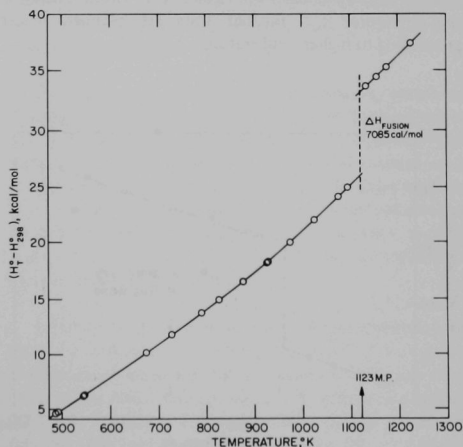


Fig. III-3. Enthalpy of  $Na_3Bi$ .

### *b. Induction-heated Calorimetric System: Enthalpy and Heat Capacity of Uranium Dioxide*

Enthalpy data for liquid  $\text{UO}_2$  have been extended to 3475°K; the data obtained to date in the liquid region are shown in Fig. III-4 along with the data of Hein and Flagella.<sup>16</sup> Our values for the liquid enthalpies are in good agreement with theirs in the region of overlap. A straight line fits the enthalpy data of the liquid within about 1%, from which a value of 33.6 cal/(mol)(°K) for the heat capacity is deduced. The heat of fusion obtained (~18 kcal/mol) is in good agreement with the literature<sup>16</sup> value of 18.2 kcal/mol.

Currently, the apparatus is being modified for use with  $(\text{U,Pu})\text{O}_2$ .

## *2. Other Studies of Physical Properties*

### *a. Vapor Pressure Over $\text{UO}_2$ at High Temperatures*

An important parameter for equation-of-state calculations for reactor fuels is the vapor pressure of the fuel. A program has been initiated to measure vapor pressures at temperatures of interest in reactor safety calculations. The first material to be studied will be uranium dioxide. The transpiration technique will be used to make such measurements up to about 3250°C. The transpiration equipment will be operated in an induction furnace; the carrier gas may be either high-purity argon or mixtures of hydrogen and water vapor. To date, vapor pressures have been measured for testing purposes at about 2350°C. Satisfactory agreement has been found with values already in the literature.<sup>17,18</sup> Further tests are planned before proceeding to higher temperatures.

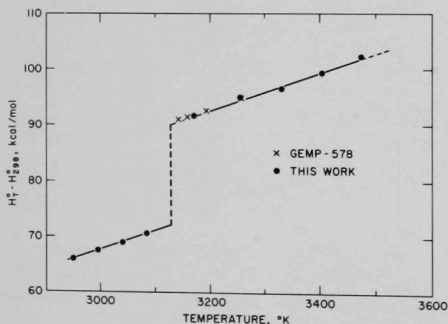


Fig. III-4. Enthalpy of  $\text{UO}_2$ .

### *b. Matrix Isolation Spectroscopy of $\text{UO}_2$*

A program to carry out experimental determination of molecular parameters of uranium and plutonium oxides in order to calculate their thermodynamic functions in the gaseous state is under way. Such data are of value in estimating fuel pressures under reactor accident conditions. Apparatus to utilize the matrix isolation technique<sup>19</sup> in conjunction with high-resolution infrared spectroscopy is under test. Future plans include spectroscopic studies of visible and ultraviolet emission of these same vapor species.

### *c. Theoretical Calculation of Measured Physical-property Data to Higher Temperatures*

The thermodynamic data needed for the calculation of partial vapor pressures of the fission products and of the fuel at the very high temperatures which may be reached during a reactor accident cannot be directly obtained by experimental means. Consequently, it is necessary either to find some basis for extrapolating existing experimental data obtained at low temperatures to higher temperatures or to perform statistical mechanical calculations of the thermodynamic properties based upon observed spectroscopic parameters.

Efforts are being made initially to develop a basic computer program suitable for calculating vapor pressures of fuel and fission products at normal operating temperatures; this same program will later be applicable to very high temperatures when appropriate thermodynamic data are available.

### *d. Speed of Sound in Molten Sodium and $\text{UO}_2$*

A knowledge of the sound velocity and compressibility of liquid sodium and liquid  $\text{UO}_2$  are of considerable value in reactor hazards analyses for equation-of-state calculations. An experimental program has been initiated to measure these quantities. First efforts will be directed toward measuring the speed of sound in sodium at higher temperatures than those for which data are presently available (700°C). We are currently evaluating materials of construction for the sodium work and designing cells to contain the material. Electronic equipment and the furnace are being tested.

### *3. Segregation in Ceramic Fuels: Studies of Fuel Migration*

Migration and segregation of fissile and fertile materials within a fast-reactor fuel during its operational lifetime could have significant effects on the operational safety of the fuel. Redistribution of plutonium in  $(\text{U,Pu})\text{O}_2$  fuels might change the chemical and physical properties of the

affected regions enough to alter the neutronics of the system, affect fuel-cladding compatibility, and change the resultant distribution of fission products. Investigation of mixed-oxide fuels in a thermal gradient has been under way to evaluate the extent of migration of plutonium and fission products, and to elucidate the mechanisms involved in the migration processes.

Results reported previously (see ANL-7550, p. 47) indicated that, for  $(U_{0.8}Pu_{0.2})O_{2.01}$  specimens 1/2 in. high by 1/2 in. in diameter heated in thermal gradients of the order of  $1000^{\circ}\text{C}/\text{cm}$ , enhancement of plutonium concentration occurred in the hottest regions. The concentration increases observed were small ( $\sim 2$  wt %  $PuO_2$  increase), and the annealing times required were 1020 hr for a sample with a temperature of  $1970^{\circ}\text{C}$  at the top surface, and 123 hr for a sample with a temperature of  $2350^{\circ}\text{C}$  at the top surface.

Additional experiments were done with similar specimens whose initial O/M ratios were 1.97. Each pellet was heated in an inverted tungsten crucible which served as a barrier to evaporative losses during the annealing period; a similar procedure had been used with the hyperstoichiometric specimens. The samples were annealed at the temperatures and times indicated:

P-10 ( $T_{\text{top}} = 2330^{\circ}\text{C}$ ,  $T_{\text{bottom}} = 1120^{\circ}\text{C}$ , 262 hr),

P-11 ( $T_{\text{top}} = 2360^{\circ}\text{C}$ ,  $T_{\text{bottom}} = 1310^{\circ}\text{C}$ , 125 hr),

P-12 ( $T_{\text{top}} = 2350^{\circ}\text{C}$ ,  $T_{\text{bottom}} = 1180^{\circ}\text{C}$ , 97 hr).

Subsequent electron-microprobe analyses showed no significant changes in plutonium concentration throughout the longitudinal sections of the specimens.

Thus, in our experiments with mixed-oxide specimens, we have observed apparent changes in plutonium concentration at the hotter end of hyperstoichiometric pellets annealed in a thermal gradient, but no such change for slightly hypostoichiometric samples. This implies that the oxygen activity of the specimen could be involved in the mechanism for enhancement of plutonium concentration. It also may imply that vaporization processes play a significant role in the observed changes. More definitive experiments would require redesign of the apparatus to achieve higher temperatures and larger thermal gradients. In view of the continuing studies of this problem at Karlsruhe, West Germany and the current assessment of this problem at a lower level of importance, it has been decided not to proceed with the design of the new apparatus. This program, therefore, will be terminated with the writing of a topical report describing the studies completed to date.

Several preliminary experiments were performed in a similar fashion with mixed-carbide fuel pellets of approximate composition  $(U_{0.85}Pu_{0.15})C$ , 0.43 in. in diameter and 0.42 in. long. In four experiments, the top surface temperatures of the samples averaged about  $2000^{\circ}\text{C}$ , and the gradients were of the order of  $700^{\circ}\text{C}/\text{cm}$ . To date, electron-microprobe analytical data are available on the two longer-term annealed specimens. These are pellet P-14 ( $T_{\text{top}} \sim 2000^{\circ}\text{C}$ ,  $T_{\text{bottom}} \sim 1370^{\circ}\text{C}$ , 437 hr) and pellet P-16 ( $T_{\text{top}} \sim 2000^{\circ}\text{C}$ ,  $T_{\text{bottom}} \sim 1320^{\circ}\text{C}$ , 460 hr). Pellet P-14 was annealed without a vaporization barrier, while pellet P-16 used an inverted tungsten crucible as a barrier. The probe results indicated that considerable loss of plutonium occurred in the upper (hottest) region of pellet P-14 (plutonium concentrations reduced to a few percent), whereas virtually no loss was observed for pellet P-16. This is not too surprising, since it is known that plutonium is the chief high-temperature vapor species over such mixed carbides. Ceramographic examination showed considerable densification and columnar grain growth in the top portion of pellet P-14, but little change was evident in pellet P-16.

### C. CALORIMETRY

The calorimetric program is directed toward the experimental, empirical, or theoretical determination of thermodynamic properties of substances that are of interest in high-temperature chemistry and nuclear technology. Measurements are being made of standard enthalpies of formation ( $\Delta H_{f,98}^{\circ}$ ) of the substances. Complementary experimental determinations of high-temperature increments ( $\Delta H_T^{\circ} - \Delta H_{98}^{\circ}$ ) are reported in Sect. III.B.1. Complementary low-temperature thermal measurements (of  $C_p^{\circ}$ ,  $\Delta H_{tr}^{\circ}$ , and  $S^{\circ}$ ) are being performed in the Chemistry Division and elsewhere.

The method of fluorine bomb calorimetry, which was developed here especially for measurements with substances not amenable to more conventional calorimetric techniques, has now been used to determine the enthalpies of formation of more than thirty elemental fluorides and more than twenty other compounds. The more conventional method of oxygen bomb calorimetry has been used for studies with 12 compounds and solution calorimetry for measurements on six aqueous reactions.

Attempts at the determination of thermodynamic properties by empirical correlations (e.g., the correlation and estimation of enthalpies of formation for the rare earth trifluorides; ANL-7450, p. 64) and by theoretical calculations (e.g., extended Hückel molecular-orbital calculations for the chalcogen hexafluorides; ANL-7450, p. 66) now include an *ab initio* calculation for NS based on the Hartree-Fock-Roothaan approach.

### 1. Thermochemistry of Uranium Compounds: Enthalpy of Formation of Uranium Diboride

As part of the continuing program to obtain thermodynamic data for uranium compounds, the enthalpy of formation of uranium diboride was determined by fluorine bomb calorimetry. Complementary high-temperature enthalpy increment and low-temperature thermal measurements were also carried out by other groups in the Chemical Engineering and Chemistry Divisions of Argonne National Laboratory.

The preparation, fluorine bomb calorimetric measurements, and low-temperature work with uranium diboride are described in a joint paper;<sup>20</sup> the high-temperature enthalpy measurements are described separately.<sup>21</sup> This research is a good example of cooperative effort among several groups to obtain consistent thermodynamic data for an important compound over a very wide temperature range: 1 to 1500°K.

The results of the fluorine bomb calorimetric measurements yielded the standard energy and enthalpy of combustion of  $UB_{1.979}$  in fluorine to give solid  $UF_6$  and gaseous  $BF_3$ ; the values are  $-3927.2 \pm 4.0$  cal g<sup>-1</sup> and  $-1021.2 \pm 1.1$  kcal mol<sup>-1</sup>, respectively. The corresponding standard enthalpy of formation,  $\Delta H_{f,298}^\circ(UB_{1.979},c)$ , is  $-39.0 \pm 4.0$  kcal mol<sup>-1</sup>, from which  $\Delta H_{f,298}^\circ(UB_2,c)$  was deduced to be  $-39.3 \pm 4.0$  kcal mol<sup>-1</sup>.

### 2. Thermochemistry of Plutonium Compounds: Enthalpy of Formation of Plutonium Monocarbide

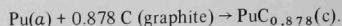
As part of a continuing program to provide accurate thermochemical data for plutonium compounds, the standard enthalpy of formation of plutonium monocarbide was determined by oxygen bomb calorimetry. Plutonium monocarbide exists as a nonstoichiometric compound with a narrow range of composition near  $PuC_{0.87}$ . Holley and Storms<sup>22</sup> have recently reviewed the thermodynamic properties of actinide carbides and from consideration of high-temperature equilibrium studies concluded that  $\Delta H_{f,298}^\circ(PuC_{0.87}) = -10.2$  kcal mol<sup>-1</sup>. They recommended, however, that the enthalpies of formation of all plutonium carbides should be measured, preferably by combustion calorimetry.

A sample of plutonium monocarbide was prepared<sup>23</sup> by arc melting high-purity plutonium and graphite. Metallographic analysis showed that the sample was single phase. Chemical and spark-source mass-spectrometric analyses indicated a total impurity content of 0.35 wt %, of which 0.30 wt % was tungsten, presumably introduced by the arc-melting electrode. The carbon content of the sample was found to be  $4.20 \pm 0.01$  wt %, which gave a plutonium

content, taken by difference, of 95.45 wt %. The C/Pu atom ratio was calculated to be  $0.878 \pm 0.001$ . The sample was stored and handled in a dry-helium atmosphere to avoid oxidation.

The combustion technique used was similar to that described previously for plutonium metal.<sup>24</sup> The product of combustion was  $PuO_2$  with a small residue (10-20 mg out of an original ~3 g) of unreacted plutonium monocarbide, which was determined by carbon analysis.

The results of five acceptable combustion experiments were combined with the enthalpies of formation of the product oxides<sup>24,25</sup> [ $PuO_2 = -252.35 \pm 0.17$  kcal mol<sup>-1</sup> and  $CO_2(g) = -94.051$  kcal mol<sup>-1</sup>] to yield  $\Delta H_{f,298}^\circ(PuC_{0.878},c) = -11.53 \pm 0.64$  kcal mol<sup>-1</sup> for the reaction



This result is in reasonable agreement with previous high-temperature equilibria studies,<sup>22</sup> but is subject to much less uncertainty.

### 3. Thermochemistry of Hydrogen Fluoride

In spite of the importance of hydrogen fluoride as a key thermochemical compound, much of its thermochemistry is still uncertain. This is particularly serious when one of its values enters a thermochemical cycle several times, e.g., in the cycle involving the solution of  $UF_6$ , the enthalpy of formation of aqueous HF (uncertain by approximately 0.5 kcal mol<sup>-1</sup>) enters six times.

Much of our work with fluorine bomb calorimetry is related to the thermochemistry of HF in one state or another. The enthalpies of combustion of Si and  $SiO_2$  in fluorine led to a paper on the enthalpy of formation of gaseous  $HF$ .<sup>26</sup> Similarly, the combustions of these same two compounds and of boron, boric oxide, carbon, iodine, magnesium, uranium, and other compounds can be used to calculate values for the enthalpy of formation of aqueous HF; the values obtained from boron, boric oxide, and carbon have, in fact, been published.<sup>27-29</sup> Most of the values for  $\Delta H_f^\circ(HF \cdot 10H_2O)$  indicate that the selected values tabulated by the National Bureau of Standards<sup>25</sup> ( $-76.235$  kcal mol<sup>-1</sup>) and by the Soviet Academy of Sciences<sup>30</sup> ( $-76.159 \pm 0.3$  kcal mol<sup>-1</sup>) are approximately 0.6 kcal mol<sup>-1</sup> too positive. In an effort to clear up the discrepancy, the enthalpy of formation of liquid HF and its enthalpy of solution have been measured directly.

#### a. Enthalpy of Formation of Liquid Hydrogen Fluoride

The enthalpy of formation of liquid hydrogen fluoride was determined by measuring the energy evolved on



reaction of fluorine with hydrogen in a bomb calorimeter whose combustion chamber had been presaturated with gaseous HF (by addition of liquid HF). With this technique, the only product of combustion was liquid HF. As a result of these measurements, the standard enthalpy of formation of liquid HF,  $\Delta H_{f,298}^{\circ}(\text{HF}, \ell)$  was calculated to be  $-71.98 \pm 0.05 \text{ kcal mol}^{-1}$ . (However, it should be noted that this value may be insufficiently negative, since recent experimental evidence has revealed a positive bias in the data.)

Because the hypergolic gas-phase reaction between hydrogen and fluorine began at the valve between the two compartments of the bomb, the design of the valve was changed from that described earlier<sup>31</sup> to minimize attack on its seat. This modification, shown in Fig. III-5, is detailed in a note titled, "An Improved Interconnecting Valve for a Two-Compartment Calorimetric Bomb."<sup>32</sup>

#### b. Enthalpy of Solution of Liquid Hydrogen Fluoride

The study of the enthalpy of solution of HF( $\ell$ ) in water was conducted in several parts: firstly, the enthalpy of solution of HF( $\ell$ ) was established by measurements at the concentration HF·200H<sub>2</sub>O; secondly, through additional solution experiments, the enthalpies of dilution of HF(aq) were obtained in the range HF·200H<sub>2</sub>O to HF·5551H<sub>2</sub>O; thirdly, enthalpies of dilution of HF(aq) were selected from

the literature in the range HF·2H<sub>2</sub>O to HF·200H<sub>2</sub>O; finally, the enthalpies of dilution from HF·5551H<sub>2</sub>O to HF· $\infty$ H<sub>2</sub>O were calculated by consideration of the enthalpy of the ionization of HF (a complex picture involving two separate equilibria) and Debye-Huckel dilution terms.

The solution measurements were conducted in an LKB-8700 heat-of-solution calorimeter equipped with a gold reaction vessel. The sample of anhydrous liquid HF used (conductivity of  $1 \times 10^{-6} \text{ ohm}^{-1} \text{ cm}^{-1}$ ) was obtained from Argonne's Chemistry Division. The HF was distilled into small ampoules constructed entirely of Kel-F plastic. The ampoules were made by hot-air welding a 1/8-in.-OD filling tube to a 3/8-in.-OD tube and then heat sealing 3-mil film windows over the open ends of the larger tube. When the ampoule was charged with HF, the filling tube was sealed with hot pliers. The reaction was initiated in the calorimeter by puncturing the film windows.

The average of six measurements of the enthalpy of solution of liquid HF in 200 moles of H<sub>2</sub>O was  $-4506.1 \pm 2.0 \text{ cal mol}^{-1}$ . Some 35 additional measurements of the enthalpy of solution were performed in which the final product was varied from HF·200H<sub>2</sub>O to HF·5551H<sub>2</sub>O. From these measurements, the enthalpies of dilution of aqueous HF, as given in Table III-4, were obtained.

The calculated enthalpy of dilution of HF·5551H<sub>2</sub>O to HF· $\infty$ H<sub>2</sub>O was  $-2349 \pm 64 \text{ cal mol}^{-1}$ . The enthalpy of dilution of HF·10H<sub>2</sub>O to HF·200H<sub>2</sub>O selected from the literature was  $-99 \text{ cal mol}^{-1}$ ; this yields a value of the enthalpy of solution of HF( $\ell$ ) in 10 moles of H<sub>2</sub>O of  $-4407 \text{ cal mol}^{-1}$ .

These results can be combined with the enthalpy of formation of HF( $\ell$ ) reported above,  $-71.98 \pm 0.05 \text{ kcal mol}^{-1}$ , to yield  $\Delta H_{f,298}^{\circ}(\text{HF} \cdot \infty \text{H}_2\text{O}) = -79.38 \pm 0.08 \text{ kcal mol}^{-1}$ ,  $\Delta H_{f,298}^{\circ}(\text{HF} \cdot 200\text{H}_2\text{O}) = -76.49 \pm 0.05 \text{ kcal mol}^{-1}$ , and

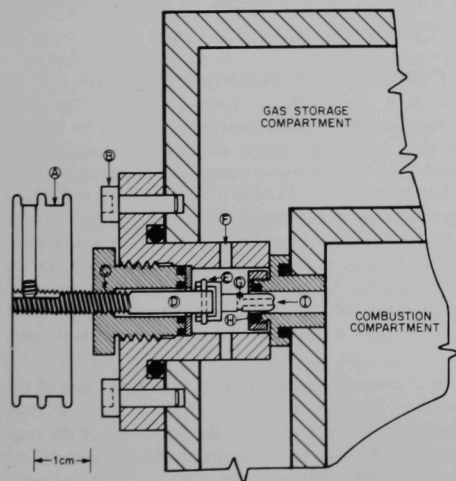


Fig. III-5. Improved Interconnecting Valve for Two-compartment Calorimetric Bomb. A, pulley; B, bolt; C, double-lead threads; D, stem; E, flexible joint; F, gas passage through valve housing; G, transverse hole; H, O-ring; I, longitudinal hole.

TABLE III-4. Enthalpies of Dilution of HF·200H<sub>2</sub>O

$n_2\text{H}_2\text{O}$	$\Delta H_{\text{diln}}^a$ (cal mol <sup>-1</sup> )
300	-25
400	-47
500	-66
600	-81
800	-113
1000	-144
2000	-286
3000	-400
4000	-471
5551 <sup>b</sup>	-545

<sup>a</sup>For the process  $\text{HF} \cdot 200\text{H}_2\text{O} + (n_2 - 200)\text{H}_2\text{O} \rightarrow \text{HF} \cdot n_2\text{H}_2\text{O}$ .  
<sup>b</sup>0.01 molal.

$\Delta H_{f,98}^{\circ}(\text{HF} \cdot 10\text{H}_2\text{O}) = -76.39 \pm 0.06 \text{ kcal mol}^{-1}$ . Thus, our results would seem to substantiate the selected value of the National Bureau of Standards.<sup>25</sup> Our results, however, must be considered preliminary and subject to revision. Both the solution results and the  $\Delta H_f^{\circ}(\text{HF}, \ell)$  result are being carefully scrutinized for evidence of a systematic bias. As noted above, a positive bias in  $\Delta H_f^{\circ}(\text{HF}, \ell)$  has been shown experimentally; however, the magnitude of the error has not been established.

#### 4. Chemical Bonding in $\text{NSF}_3$ , $\text{NSF}$ , and $\text{NS}$

##### a. The Enthalpies of Formation of $\text{NSF}_3$ and $\text{NSF}$ , and the $\text{N}=\text{S}$ Bond Strengths

The sulfur-nitrogen halides, for which there are few thermodynamic data, have been the subject of several physicochemical investigations in recent years.<sup>3,3</sup> The multiplicity of nitrogen-sulfur bonds, up to and including formal triple bonds, is of considerable interest. The compounds  $\text{NSF}_3$  and  $\text{NSF}$  have formal triple bonds. The energy of combustion in fluorine of a sample of  $\text{NSF}_3$ , prepared by O. Glemser and J. Wegener of the University of Göttingen, Germany, was measured in a bomb calorimeter; a value of  $-85.2 \pm 0.5 \text{ kcal mol}^{-1}$  was determined for  $\Delta H_{f,98}^{\circ}(\text{NSF}_3, \text{g})$ . Combination of this result with reported mass-spectrometric appearance-potential data<sup>34</sup> yielded  $\Delta H_{f,98}^{\circ}(\text{NSF}, \text{g}) = +41 \pm 2 \text{ kcal mol}^{-1}$ ,  $\Delta H_{f,98}^{\circ}(\text{SF}_4, \text{g}) = -162 \text{ kcal mol}^{-1}$ , and  $\text{N}=\text{S}$  bond-dissociation enthalpies of approximately 93 and 71  $\text{kcal mol}^{-1}$  for  $\text{NSF}_3$  and  $\text{NSF}$ , respectively. The results for  $\Delta H_f^{\circ}(\text{SF}_4, \text{g})$  is substantially different from previously reported values<sup>35-37</sup> and indicates that it should be redetermined by a direct technique, such as the fluorination of  $\text{SF}_4$  to  $\text{SF}_6$ .

##### b. Nitrogen Sulfide ( $\text{NS}$ ): Dissociation Energy, Enthalpy of Formation, Ionization Potential, and Dipole Moment

Although nitrogen sulfide,  $\text{NS}$ , an unstable radical, has been known for some time,<sup>38</sup> apparently no thermochemical properties have been determined, owing, undoubtedly, to the transient nature of the molecule. Consequently, a study was initiated to deduce some thermochemical data for  $\text{NS}$  and also for  $\text{NS}^+$  (the latter ion was first observed spectroscopically by Dressler<sup>39</sup>). The study is detailed in a paper<sup>40</sup> titled, "Dissociation Energies, Enthalpies of Formation, Ionization Potentials, and Dipole Moments of  $\text{NS}$  and  $\text{NS}^+$ " which may be summarized as follows:

A dissociation energy of  $4.8 \pm 0.25 \text{ eV}$  at  $0^\circ\text{K}$  has been deduced for  $\text{NS}(^2\pi)$  from spectroscopic data in the literature; the corresponding value for  $\Delta H_f^{\circ}(\text{NS})$  is

$2.91 \pm 0.26 \text{ eV}$ . Recent experimental results for  $\Delta H_f^{\circ}(\text{NSF})$  reported above indicate  $\Delta H_f^{\circ}(\text{NS}^+, ^1\Sigma^+) = 12.72 \pm 0.10 \text{ eV}$ . Thus, the ionization potential of  $\text{NS}$  is  $9.81 \pm 0.28 \text{ eV}$ . A Hartree-Fock-Roothaan *ab initio* calculation for  $\text{NS}$  yielded an ionization potential of 10.10 eV, based on Koopman's theorem, in good agreement with the experimental value, and a dipole moment of 1.732 D. Combining the value of  $\Delta H_f^{\circ}(\text{NS}^+)$  with enthalpies of formation of the assumed products,  $\text{S}^+(\text{g})$  and  $\text{N}(\text{g})$ , gives the previously unreported dissociation energy of  $\text{NS}^+$  as  $5.31 \pm 0.31 \text{ eV}$ . It is not surprising that the dissociation energy for  $\text{NS}^+$  is greater than that for  $\text{NS}$ , since the latter contains one more antibonding electron.

#### 5. Enthalpy of Formation of Molybdenum Disulfide

Several years ago at this Laboratory, an oxygen bomb study was carried out with  $\text{MoS}_2$  (see ANL-6029, p. 65). However, the chemical processes in the bomb were very difficult to define; consequently, a reliable result for  $\Delta H_f^{\circ}(\text{MoS}_2)$  could not be obtained. There are also several conflicting values in the literature<sup>41-43</sup> for  $\Delta H_f^{\circ}(\text{MoS}_2)$ , ranging from -91 to -48  $\text{kcal mol}^{-1}$ .

Because  $\text{MoS}_2$  burns completely in fluorine to yield only  $\text{MoF}_6$  and  $\text{SF}_6$ , and since a calorimetric-grade sample of  $\text{MoS}_2$  was available, a study of the heat of combustion was undertaken. Preliminary results indicate a value for  $\Delta H_f^{\circ}(\text{MoS}_2)$  of about -65  $\text{kcal mol}^{-1}$ . This result is subject to substantial change depending on analytical results not yet available.

#### 6. Thermochemistry of Aqueous Xenon Trioxide

Xenon trioxide,  $\text{XeO}_3$ , and its derivatives are perhaps the most unexpected of the noble gas compounds. Solid xenon trioxide is explosively unstable and has an enthalpy of formation of  $96 \pm 2 \text{ kcal mol}^{-1}$ .<sup>44</sup> Solutions of  $\text{XeO}_3$  in dilute aqueous acid, although they are potent oxidizers,<sup>45</sup> show no evidence of spontaneous decomposition; because of this, they have received more experimental attention than has the dangerous solid. A reliable quantitative determination of the thermodynamic oxidizing power of these solutions is therefore of considerable practical value.

In a cooperative venture with E. H. Appelman of the Chemistry Division, who prepared the samples, solution calorimetric measurements of the enthalpies of the reactions of  $\text{XeO}_3(\text{aq})$  with  $\text{HI}(\text{aq})$  and of  $\text{I}_2(\text{c})$  with  $\text{HI}(\text{aq})$  have been used to obtain a value of  $99.94 \pm 0.24 \text{ kcal mol}^{-1}$  for  $\Delta H_{f,98}^{\circ}(\text{XeO}_3 \cdot 96.15\text{H}_2\text{O})$ . The electrode potentials of the  $\text{Xe}-\text{XeO}_3$  couple in acidic solution and of the  $\text{Xe}-\text{HXeO}_3^-$  couple in basic solution were deduced to be  $2.10 \pm 0.01$  and  $1.24 \pm 0.01 \text{ V}$ , respectively.

7. *Enthalpies of Formation of  $\text{KBrO}_4(c)$  and  $\text{KBrO}_3(c)$  and the Thermodynamic Properties of the Perbromate and Bromate Ions*

The recent discovery of preparative methods for perbromic acid and perbromates by E. H. Appelman of the Chemistry Division<sup>46,47</sup> has ended a long search for these compounds. In a second cooperative effort with Appelman, the determination of the energies of decomposition of  $\text{KBrO}_4(c)$  and  $\text{KBrO}_3(c)$  to  $\text{KBr}$  and  $\text{O}_2(g)$ , and of the enthalpies of solution of  $\text{KBrO}_4(c)$  and  $\text{KBrO}_3(c)$  in  $\text{H}_2\text{O}$ , was carried out to help in the exploitation of these new compounds and in the explanation of the past difficulties encountered in their synthesis. The results of the study were used to derive  $\Delta H_f^\circ_{298}(\text{KBrO}_4, c) = -68.74 \pm 0.14 \text{ kcal mol}^{-1}$  and  $\Delta H_f^\circ_{298}(\text{KBrO}_3, c) = -86.02 \pm 0.12 \text{ kcal mol}^{-1}$ . The enthalpies of solution at  $25^\circ\text{C}$  of  $\text{KBrO}_4(c)$  in 2144 moles of  $\text{H}_2\text{O}$  and of  $\text{KBrO}_3(c)$  in

1808 moles of  $\text{H}_2\text{O}$  were measured to be  $11606 \pm 20$  and  $9765 \pm 42 \text{ cal mol}^{-1}$ , respectively. These values were used to derive standard ( $298.15^\circ\text{K}$ ) thermodynamic properties for the perbromate ion:  $\Delta H_f^\circ = 3.19 \pm 0.15 \text{ kcal mol}^{-1}$ ,  $S^\circ = 44.7 \pm 2.0 \text{ cal deg}^{-1} \text{ mol}^{-1}$ , and  $\Delta G_f^\circ = 29.18 \pm 0.63 \text{ kcal mol}^{-1}$ ; and for the bromate ion:  $\Delta H_f^\circ = -15.95 \pm 0.13 \text{ kcal mol}^{-1}$ ,  $S^\circ = 38.6 \pm 0.3 \text{ cal deg}^{-1} \text{ mol}^{-1}$ , and  $\Delta G_f^\circ = 4.55 \pm 0.14 \text{ kcal mol}^{-1}$ . The standard electrode potential of the bromate-perbromate couple in acid solution was calculated to be  $1.763 \pm 0.014 \text{ V}$  at  $298.15^\circ\text{K}$ .

Selected values for the thermodynamic properties of the halates and perhalates of chlorine and iodine are also tabulated.<sup>48</sup> Although the perbromate ion is more oxidizing than either perchlorate or periodate ion, the difference is not great enough to explain why the synthesis of perbromates has been so difficult.

## REFERENCES AND FOOTNOTES

1. R. S. Ackermann, R. L. Faircloth, and M. H. Rand, *J. Phys. Chem.* **70**, 3698 (1966).
2. Free energy of formation of  $\text{PuO}_2$  computed from the heat of formation of  $\text{PuO}_2$  at  $298^\circ\text{K}$ , G. K. Johnson, E. H. Van Deventer, O. L. Kruger, and W. N. Hubbard, *J. Chem. Thermodyn.* **1**, 89 (1969); entropies and heat contents for  $\text{PuO}_2$ , O. L. Kruger and H. Savage, *J. Chem. Phys.* **49**, 4540 (1968); entropies and heat contents for  $\text{Pu}$ , F. L. Oetting, *Chem. Rev.* **67**, 261 (1967); entropies and heat contents for  $\text{O}_2$ , D. R. Stull and G. K. Sinke, *Thermodynamic Properties of the Elements*, American Chemical Society, Washington, D.C. (1956), p. 143.
3. T. L. Markin and M. H. Rand, *Proceedings of the Symposium on Thermodynamics with Emphasis on Nuclear Materials and Atomic Transport in Solids*, International Atomic Energy Agency, Vienna (1965), p. 145.
4. J. E. Battles, W. A. Shinn, P. E. Blackburn, and R. K. Edwards, *High Temp. Sci.* (in press).
5. J. G. Reavis, Los Alamos Scientific Laboratory, private communication (1969).
6. W. M. Olsen and R. N. R. Mulford, *Thermodynamics of Nuclear Materials*, IAEA, Vienna (1967), p. 467.
7. P. S. Harris, B. A. Phillips, M. H. Rand, and M. Tetenbaum, UKAEA Report AERE-R 5353, Part 1 (1967).
8. R. Lapage, UKAEA, Aldermaston, Berkshire, England, private communication (1969).
9. E. J. Huber and C. E. Holley, Jr., *Thermodynamics of Nuclear Materials*, IAEA, Vienna (1962), p. 581.
10. T. L. Markin and R. S. Street, *J. Inorg. Nucl. Chem.* **29**, 2265 (1967).
11. E. K. Storms, *The Refractory Carbides*, Ch. XI, Academic Press, New York (1967), pp. 205-213.
12. R. J. Ackermann and E. G. Rauh, *J. Phys. Chem.* **73**, 769 (1969).
13. H. L. Schick, *Thermodynamics of Certain Refractory Compounds*, Vol. II, Academic Press, New York (1966).
14. Vienna Panel, Technical Series No. 14, *The Uranium-Carbon and Plutonium-Carbon Systems*, IAEA, Vienna (1963).
15. E. K. Storms and E. J. Huber, *J. Nucl. Mater.* **23**, 19 (1967).
16. R. A. Hein and P. N. Flagella, *Enthalpy Measurements of  $\text{UO}_2$  and Tungsten to  $3260^\circ\text{K}$* , GEMP-578 (1968).

17. ANL-7055, p. 165 (1965).
18. M. Tetenbaum and P. D. Hunt, *Total Pressure of Uranium-Bearing Species Over Oxygen-Deficient Urania*, J. Nucl. Mater. (in press).
19. E. D. Becker and G. C. Pimentel, J. Chem. Phys. 25, 224 (1948).
20. H. E. Flotow, D. W. Osborne, P. A. G. O'Hare, J. L. Settle, F. C. Mrazek, and W. N. Hubbard, J. Chem. Phys. 51(2), 583 (1969).
21. D. R. Fredrickson, R. D. Barnes, M. G. Chasanov, R. L. Nuttall, R. Kleb, and W. N. Hubbard, High Temp. Sci. 1(3), 373-380 (1969).
22. C. E. Holley, Jr. and E. K. Storms, "Actinide Carbides. A Review of Thermodynamic Properties," in *Thermodynamics of Nuclear Materials, 1967*, IAEA (1968), p. 397.
23. By O. L. Kruger of the ANL Metallurgy Division.
24. G. K. Johnson, E. H. Van Deventer, O. L. Kruger, and W. N. Hubbard, J. Chem. Thermodyn. 1, 89 (1969).
25. D. D. Wagman, W. H. Evans, V. P. Parker, I. Halow, S. M. Bailey, and R. H. Schumm, NBS Technical Note 270-3, U.S. Government Printing Office, Washington, D.C. (1968).
26. H. M. Feder, S. S. Wise, J. L. Margrave, and W. N. Hubbard, J. Phys. Chem. 67, 1148 (1963).
27. G. K. Johnson, H. M. Feder, and W. N. Hubbard, J. Phys. Chem. 70, 1 (1966).
28. G. K. Johnson and W. N. Hubbard, J. Chem. Thermodyn. 1, 459 (1969).
29. E. Greenberg and W. N. Hubbard, J. Phys. Chem. 72, 222 (1968).
30. V. A. Medredev et al., *Thermochemical Constants of Substances*, Vol. 1, Acad. Sci. High Temp. Inst., Moscow (1965), p. 42.
31. J. L. Settle, E. Greenberg, and W. N. Hubbard, Rev. Sci. Instr. 38, 1805 (1967).
32. T. L. Denst, E. Greenberg, J. L. Settle, and W. N. Hubbard, Rev. Sci. Instr. (in press).
33. O. Glemser and M. Fild, in *Halogen Chemistry*, Vol. II, Chap. 1, V. Gutmann, ed., Academic Press, New York (1967).
34. O. Glemser, A. Müller, D. Böhrer, and B. Krebs, Z. Anorg. Allgem. Chem. 357, 184 (1968).
35. M. J. Nichols, Ph.D. Thesis, The University of Durham, England (1958).
36. J. D. Vaughn and E. L. Muetterties, J. Phys. Chem. 64, 1787 (1960).
37. J. Kay and F. M. Page, Trans. Faraday Soc. 60, 1042 (1964).
38. A. Fowler and C. J. Bakker, Proc. Roy. Soc. (London) A136, 28 (1932).
39. K. Dressler, Helv. Phys. Acta 28, 563 (1955).
40. P. A. G. O'Hare, J. Chem. Phys. (in press).
41. I. A. Makolkin, Acta Physicochimica U.S.S.R. 13, 361 (1940).
42. J. R. Stubbles and F. D. Richardson, Trans. Faraday Soc. 56, 1460 (1960).
43. H. R. Larson and J. F. Elliott, Trans. Met. Soc. AIME 239, 1713 (1967).
44. S. R. Gunn in *Noble Gas Compounds*, H. H. Hyman, ed., University of Chicago Press, Chicago (1963), p. 149.
45. E. H. Appelman and J. G. Malm, J. Amer. Chem. Soc. 86, 2141 (1964).
46. E. H. Appelman, J. Amer. Chem. Soc. 90, 1900 (1968).
47. E. H. Appelman, Inorg. Chem. 8, 223 (1969).
48. G. K. Johnson, P. N. Smith, E. H. Appelman, and W. N. Hubbard, Inorg. Chem. 9, 119 (1970).

#### IV. ANALYTICAL AND REACTOR CHEMISTRY

##### A. CHEMISTRY OF IRRADIATED FAST-REACTOR FUELS AND MATERIALS

An understanding of the chemical and physical behavior of fast-reactor fuels during irradiation is necessary for the selection, fabrication, and utilization of fuel and reactor materials that will meet the high-performance criteria required in future commercial fast breeder reactors. The program has been concerned primarily with establishing the properties of irradiated uranium-plutonium oxides clad in stainless steel; however, the program has been extended recently to include the study of irradiated uranium-plutonium carbide fuels.

##### 1. Electron-microprobe Analysis of Irradiated $\text{UO}_2\text{-PuO}_2$ Fuel

The electron microprobe, which accomplishes micro-sampling and analysis directly, is being used to provide information about fuel-cladding interactions, the distribution of fission products, and the formation of inclusions in irradiated fuel. A detailed study has been made of a cross section of a vibratorily compacted  $\text{UO}_2\text{-20 wt } \%\text{ PuO}_2$  fuel pin (SOV-3) clad in type 304 stainless steel and irradiated in EBR-II to a maximum burnup of 3.7 at. %. The centerline temperature of the fuel during irradiation was estimated to be  $2790^\circ\text{C}$ ; the fuel surface temperature,  $1060^\circ\text{C}$ ; and the cladding temperature,  $600^\circ\text{C}$ . Results of a study of a similar pin, irradiated to 2.7 at. % burnup, were reported in ANL-7550, pp. 48-51.

Examination of metallic inclusions in the fuel indicated that constituents of the cladding had been transported into the fuel matrix. Inclusions in the columnar-grain region (the innermost zone of the fuel, which reached the highest temperature during irradiation) contained molybdenum, ruthenium, rhodium, technetium, small quantities of iron, and traces of palladium. Near the boundary of the columnar and equiaxed grains (an intermediate temperature zone), the inclusions were either pure iron or iron and palladium with lesser amounts of the other noble metal fission products. In cooler regions, iron was alloyed with palladium or molybdenum. In contrast, chromium penetrated into the fuel matrix only slightly and was found primarily as an oxidized species in the fuel-cladding interface. Nickel was found segregated in the cladding grain boundaries, but, in general, did not migrate into the fuel matrix.

Electron-microprobe examination of the fuel-cladding interface indicated that an intergranular attack of the cladding had occurred and that the mechanism of attack was interaction of the cladding with fission products in the

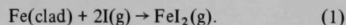
fuel. A typical area of intergranular attack is shown in the X-ray scanning images of Fig. IV-1. The average depth of cladding attack was  $\sim 90\text{ }\mu\text{m}$ . The feature of greatest interest in this fuel can be seen in Fig. IV-1g, which shows, for the first time, the presence of iodine in the area of intergranular attack. The other X-ray scans show the distribution of iron, nickel, chromium, cesium, barium, and tellurium.

The presence of iodine in the areas of intergranular attack has led to the hypothesis that iodine is involved in the metal transport from the cladding to the fuel matrix. It is suggested that the transport mechanism is similar to that of the van Arkel-de Boer process, in which purification and vapor deposition of a metal is achieved by transport and decomposition of a metal iodide in a thermal gradient. In the fuel during irradiation, the transport mechanism would involve an iodine-cycling process in which fission product iodine migrates to the cladding-fuel interface and reacts with the cladding to form gaseous iodides which are then transported to higher-temperature regions of the fuel, where decomposition of the iodides occurs. The process appears to be initiated only if the cladding temperature is high enough to produce (1) appreciable attack on the stainless steel and (2) vaporization of the metallic iodides.

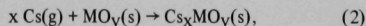
The proposed mechanism for iron transport may be formulated as follows:

(a) Ferrous iodide is the gaseous species which is transported through the fuel.

(b) The ferrous iodide is formed at the cladding surface by the reaction

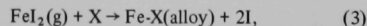


(c) The atomic iodine for Reaction 1 is formed by the decomposition of cesium iodide. The production of iodine is enhanced by the removal of cesium through reactions of the general type

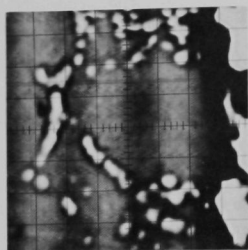


where M is U, Cr, or other elements that form acidic oxides.

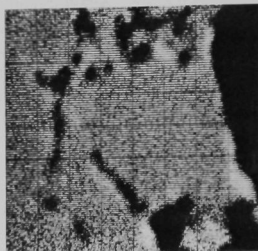
(d) The ferrous iodide decomposes in the higher-temperature regions of the fuel by the reverse of Reaction 1 or by the reaction



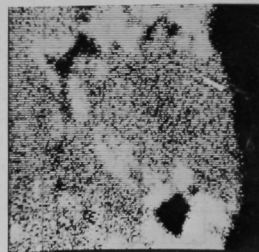
where X is Pd, Mo, Ru, Tc, or their alloys.



a) SPECIMEN CURRENT



b) IRON



c) NICKEL



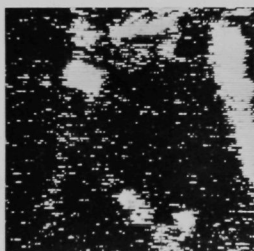
d) CHROMIUM



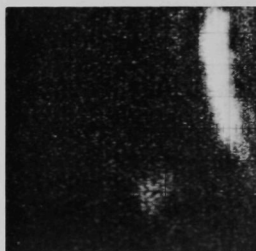
e) CESIUM



f) BARIUM



g) IODINE



h) TELLURIUM

Fig. IV-1. Electron-microprobe Scanning Images of Fuel-Cladding Interface of a  $\text{UO}_2$ -20 wt %  $\text{PuO}_2$  Fuel Pin (SOV-3) Clad with Type 304 Stainless Steel. (All images represent areas  $45 \mu\text{m}$  square.)



Investigation of the thermodynamic considerations of the proposed transport mechanism and the possible effect of other elements is being undertaken in a separate program (see Sect. III.A).

## 2. Electron-microprobe Analysis of Irradiated UC-PuC Fuel

Preliminary electron-microprobe examinations have been carried out on two vibratorily compacted uranium-plutonium carbide (UC-20 wt % PuC) fuel pins. One of the fuel pins (SMV-1) was clad with type 316 stainless steel and had been irradiated in EBR-II to 2.6 at. % burnup; the second pin (SMV-2) was clad with type 304 stainless steel and had been irradiated in EBR-II to 6.9 at. % burnup. The temperatures of the fuel-cladding interfaces for SMV-1 and SMV-2 during irradiation were 625 and 675°C, respectively. Both the UC and PuC fractions of the fuel material were hyperstoichiometric, the UC containing UC<sub>2</sub> and the PuC containing Pu<sub>2</sub>C<sub>3</sub>. The average particle size of the PuC was <44 μm and that of the UC was 500-1700 μm. As a result of this large difference in particle sizes and the method of fabrication (vibratorily compaction), the fuel material at the fuel-cladding interfaces was primarily the more finely divided PuC.

Both fuel pins showed a minor attack of the cladding at the fuel-cladding interface. The depth of reaction was about 7 μm for SMV-1 (2.6 at. % burnup) and about 15 μm for SMV-2 (6.9 at. % burnup); this extent of reaction is small compared with the fuel-cladding reaction observed for oxide fuels. The reaction in the carbide fuels resulted in the formation of separated bands of the stainless steel components and the migration of nickel into the fuel matrix. A composite X-ray image of the fuel-cladding interface of SMV-2 is shown in Fig. IV-2. The large particle seen in the fuel matrix (A to B) is uranium carbide; the remainder of the matrix shown is finely divided PuC. In the region B to C, the light areas are nickel that has moved out into the fuel matrix. In the cladding reaction zone (C to D) is the separated band of stainless steel components. Within this band, the variations in brightness are caused by variations in the nickel and chromium contents; the black areas are voids. The area of the figure from D to E is unreacted cladding. The cladding-interface regions of both pins were free of both cesium and iodine fission products.

Several mechanisms can be proposed to account for the observed migration of nickel. The first mechanism is a carbonyl transport process, similar to the Mond process for producing nickel metal. In the carbide fuel, the transport process would be the reaction of nickel in the cladding with carbon monoxide to form nickel carbonyl, followed by the vaporization and migration of the nickel carbonyl to hotter areas of the fuel, where it subsequently decomposes. There is probably sufficient oxygen in a fabricated fuel for carbon

monoxide to be present during irradiation. The extent of nickel transport by this mechanism would be expected to be less than the extent of iron and chromium transport by iodine in stainless steel-clad oxide fuels, principally because nickel carbonyl has a lower stability than ferrous or chromous iodide. The second mechanism that could account for nickel migration is the reaction of the carbide fuel (containing a slight excess of carbon) with nickel in the cladding to form a mixed plutonium-nickel carbide. Further investigations are planned to establish the exact nature of the mechanism for nickel transport.

Preliminary studies have also been conducted to determine the distribution of fission products in the carbide fuel. Spectral profiles taken of the homogeneous uranium carbide particles revealed detectable quantities of zirconium and molybdenum. Typical particles (average size, ~700 μm) located near the center and periphery of the fuel were examined for these elements. No concentration difference was observed for either element as a function of (1) location within a given particle or (2) location of the particle within the fuel pin.

Spectral analysis of the porous plutonium carbide phase indicated the presence of neodymium, palladium, and cesium. The cesium was observed throughout the plutonium carbide in localized concentrations. This is in contrast to the behavior of cesium in oxide fuels, where cesium is

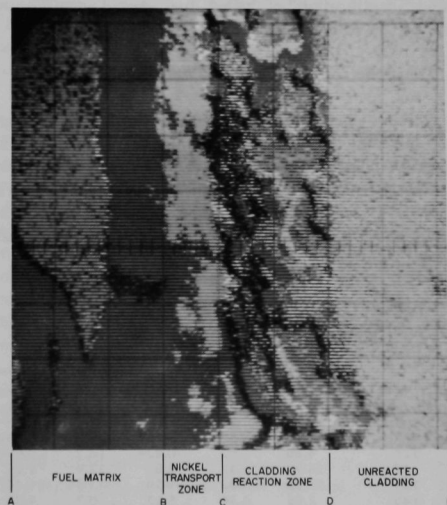


Fig. IV-2. Electron-microprobe X-ray Image of Fuel-Cladding Interface of a UC-20 wt % PuC Fuel Pin (SMV-2) Clad with Type 304 Stainless Steel. (Image represents an area 45 μm square.)

found primarily in the cooler zones (i.e., near the cladding) of the fuel. Although these studies are only preliminary in character, they do indicate some striking differences in the behavior of fission products in carbide fuels as contrasted with oxide fuels.

## B. XENON TAGGING OF FUEL ELEMENTS IN EBR-II

A cooperative program between the Chemical Engineering Division and the EBR-II Project was carried out during 1969 to develop and implement a method for identifying experimental fuel elements that fail in EBR-II. The method, which utilizes mixtures of xenon isotopes as fuel-element tags, is being applied primarily to the identification of unencapsulated gas-bonded fuel elements, most of which will contain  $\text{UO}_2\text{-PuO}_2$ .

Fuel-cladding failures in EBR-II are adequately detected by three instruments. Although detection is thorough, identification of the subassembly in which failure occurred has been difficult and time-consuming. In the xenon-tagging system, each fuel element in a subassembly is tagged with 1 ml of a mixture of xenon isotopes that is unique for a particular subassembly. If a cladding failure is indicated, a sample of the reactor cover gas will be analyzed mass spectrometrically to determine the ratios of xenon isotopes present. Positive identification of the released xenon mixture will permit identification of the affected subassembly and its location in the reactor. This method of rapid identification of failed fuel should significantly increase the EBR-II plant factor.

### 1. Preparation of Xenon-tag Mixtures

Because xenon isotopes with mass numbers 131 through 136 are abundantly produced by fission, xenon-tag mixtures for failed-fuel identification must contain significant concentrations of isotopes of lower mass numbers. Table IV-1 shows the isotopic composition of natural xenon and four mixtures enriched in the light isotopes that are available from Mound Laboratory.<sup>1</sup>

TABLE IV-1. Isotopic Composition of Natural Xenon and Four Light-isotope-enriched Mixtures from Mound Laboratory

Mass Number of Xenon Isotope	Total Xenon <sup>a</sup> (mol %)				
	Mound Mixture				Natural Xenon
	No. 1	No. 2	No. 3	No. 4	
124	12.10	5.58	1.257	21.3	0.096
126	4.80	1.92	0.834	10.2	0.090
128	16.70	10.32	8.02	23.9	1.92
129	58.78	63.02	63.50	43.4	26.44
130	2.25	4.30	5.25	0.7	4.08
131	3.13	9.43	13.11	0.4	21.18
132	1.70	5.03	7.46	0.1	26.89
134	0.29	0.34	0.496	<0.1	10.44
136	0.25	0.026	0.080	<0.1	8.87

<sup>a</sup>Xenon purity  $\geq 99.0\%$ .

Eighteen tag mixtures have been prepared by blending Mound Mixtures 1, 2, or 3 with natural xenon in varying proportions. The isotopic ranges of the resultant tag mixtures are shown in Fig. IV-3 as subseries A1, A2, and A3, respectively.

Eighteen tag mixtures will not be adequate for EBR-II tagging requirements and, therefore, consideration has been given to preparing additional tag mixtures. Tag mixtures can be prepared by blending a mixture of high enrichment from Mound Laboratory with one of low enrichment. The isotopic ranges of two subseries of such blendings are shown as A4 and A5 in Fig. IV-3; the indicated isotopic ranges would provide twenty-three additional tag mixtures. Additional tag mixtures also can be prepared by blending Mound Laboratory enriched mixtures with pure  $^{128}\text{Xe}$ , prepared by neutron irradiation of natural iodine.

### 2. Implementation of Xenon-tagging System

Three methods have been developed for charging fuel elements with xenon tags; all have been used successfully. In the first, tag gas is removed from the transfer container at negative pressure by means of a glass-enclosed mercury piston and supplied to a chamber equipped with a rubber septum at a slightly positive pressure. A hypodermic needle and syringe is used to withdraw tag gas through the septum and discharge it in 1-ml aliquots into the fuel elements comprising a subassembly. The second method utilizes the septum and syringe portion of the first system, but the gas is transferred by cryogenic means. This modified method of transfer eliminates the possibility of mercury contamination, and the all-metal construction of the system eliminates fragile components. The third method<sup>2</sup> consists of pressurizing the tag-supply container with helium in the desired helium-to-xenon proportions and backfilling

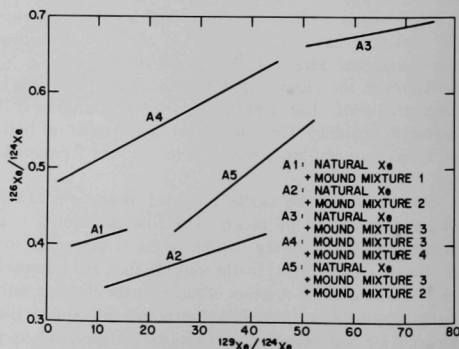


Fig. IV-3. Isotopic Relationships of Series A Xenon Tags.

evacuated fuel elements with the pressurized mixture. In each method, the tagged fuel element is immediately capped and seal-welded.

The effect of a xenon tag upon the thermal conductance of the fuel-to-cladding gap during early irradiations has been investigated in one experiment by Pacific Northwest Laboratory<sup>3</sup> (PNL) and will shortly be investigated further in an ANL experiment<sup>4</sup> by EBR-II Project personnel. In the PNL experiment, four fuel elements of abbreviated length, containing helium-xenon mixtures ranging from 0 to 100% xenon, were irradiated for 4 hr in the "rabbit" facility of a thermal reactor under conditions that guaranteed central melting of the fuel. Post-irradiation metallographic examination revealed that concentrations of xenon representative of xenon tags would not have a significant effect upon the gap conductance. In the ANL experiment, tagged and untagged fuel elements with central thermocouples will be arranged in a single subassembly so that they will experience the same neutron flux when installed in EBR-II. In this experiment, the effect of a xenon tag on the gap conductance can be continuously determined by means of the thermocouples for a wide range of power densities.

Identification of a released tag mixture will be accomplished by mass-spectrometric analysis of a sample of the EBR-II cover gas. A cover-gas sampling system, utilizing activated carbon cooled to  $-78^{\circ}\text{C}$  as a preferential xenon sorbent, has been developed at EBR-II. A mass spectrometer has been procured which incorporates a versatile dual collector system and three sample-inlet modes to permit rapid identification of released tag mixture for a variety of sample conditions.

The developmental studies on the xenon-tagging program in the Chemical Engineering Division have been completed, and the program is now under the direction of the EBR-II Project.

### **C. DETERMINATION OF BURNUP IN FAST-REACTOR FUELS**

The program for the development of methods for measuring burnup in fast-reactor fuels has two main objectives: (1) to develop accurate analytical methods for determining the concentration of fission products that can be used as burnup monitors and (2) to establish accurate values for their fast-fission yields.

#### **1. X-ray-spectrometric Determination of Fission Product Rare Earths**

A method is currently under development for measuring burnup in fast-reactor fuels by X-ray-spectrometric assay of

the four principal rare earths: lanthanum, cerium, praseodymium, and neodymium. The ten isotopes of these elements have a combined fission yield of about 40% and represent 90% of the fission product rare earths. The use of these rare earths for monitoring burnup, rather than an individual rare earth nuclide, increases the reliability of the burnup analysis: the combined fission yield is less subject to variations with fissioning nuclide, neutron energy, and integrated neutron flux.

The main steps in the procedure are as follows: (1) addition of terbium (a rare earth not produced in significant yield in fission) as an internal standard; (2) separation of the rare earths from uranium, plutonium, and the more active fission products by ion exchange in hydrochloric acid; (3) electroplating of the rare earths on aluminum; (4) X-ray-spectrometric assay for the fission product rare earths and the terbium standard; and (5) determination of the amount of each rare earth by means of the ratios of rare earth-to-terbium line intensities.

The internal-standard technique has proved to be an effective means of achieving the requisite precision. In a test of the precision of the entire method, four samples consisting of  $35\text{ }\mu\text{g}$  of terbium and  $100\text{ }\mu\text{g}$  of a simulated mixture of fission product rare earths were carried through the separation procedure, electroplated, and assayed. The ratios of rare earth-to-terbium line intensities were compared with standards of the same composition that were electroplated directly. The test showed that the line-intensity ratios of the samples could be measured with adequate precision: La/Tb, 1.7%; Ce/Tb, 2.6%; Pr/Tb, 1.6%; Nd/Tb, 0.5%.

The accuracy of the method in converting line-intensity ratios to amounts of each rare earth in a fuel sample is dependent on making suitable corrections for any inter-elemental effects in the X-ray-spectrometric assay. These include the effects of one rare earth on another, and of barium and cesium (fission products that are not separated from the rare earths in the procedure) upon the individual rare earths. Possible interferences were assessed by measurements of the individual elements at appropriate wavelengths, and a computer program based on the intensity relationships was devised to make the necessary corrections.

The entire procedure was tested on a solution of irradiated  $\text{UO}_2$  fuel of  $\sim 6$  at. % burnup to determine whether any major problems, not previously considered, would be encountered in the analysis of actual fuel samples. The sample had previously been analyzed for total rare earths by EDTA titration. The concentrations of the four rare earths, as determined by X-ray-spectrometric analysis, were compared with the concentrations calculated (on the basis of fission yields of the individual rare earths) from the

results of the total rare earth (TRE) titration analysis. This comparison is given below:

Rare Earth	Concentration ( $\mu\text{mol/ml}$ )	
	Determined by X-ray Analysis	Calculated from TRE Analysis
La	0.0842	0.0857
Ce	0.1752	0.1622
Pr	0.0762	0.0805
Nd	0.2706	0.2722
Total	0.6062	0.6006

The agreement of these results indicates that the analysis of irradiated fuels presents no unforeseen problems and lends confidence to the potential application of the method to burnup analysis.

## 2. A New Method for the Determination of Fast-fission Yields

The fission yield of a burnup monitor is established by irradiating a sample of the fissile nuclide and measuring (1) the concentration of the fission product of interest and (2) the number of fissions that produced the fission product nuclide. Of these, the number of fissions is, by far, the more difficult to measure. The most common approach has been to irradiate a fissile nuclide until 20 to 30% of the atoms are fissioned and determine the number of fissions by measuring the change in actinide-atom content of the sample. The analyses are relatively easy to carry out, but irradiations of 4- to 5-yr duration are required in a fast reactor. Another approach has been to irradiate the fissile material until 1 to 2% of the atoms are fissioned, analyze the irradiated sample for all the fission product nuclides in one of the mass peaks, and determine the number of fissions from the sum. (The sum of the fission yields of the individual nuclides in one mass peak is 100%.)

A new technique for determining the number of fissions is under development. This technique, by comparison, will be relatively easy to execute and will, therefore, provide a means for determining fission yields more readily in a

variety of fast-neutron energy spectra. Two irradiations are required: one of about 2-hr duration at a low level of reactor power and one of about 3-month duration at full reactor power.

Included in the short irradiation are fission-track counters (mica discs alternately stacked with platinum discs on which are mounted nanogram amounts of the fissile material) and fission foils (milligram amounts of the fissile material). These samples provide data for establishing a factor relating the number of fissions that occurred to the count rate of a particular fission product, e.g.,  $^{144}\text{Ce}$  ( $t_{1/2} = 285$  days). The fission tracks on the mica discs are counted under a microscope; the  $^{144}\text{Ce}$  activity of the fission foils is determined by gamma spectrometry. Included in the long irradiation are gram amounts of the fissile material, which are subsequently analyzed for the fission product whose yield is being determined and for  $^{144}\text{Ce}$  activity. The number of fissions that occurred is established from the  $^{144}\text{Ce}$  activity and the previously determined fissions-to- $^{144}\text{Ce}$  factor.

An evaluation of this approach was made in support of a Reactor Physics Division experiment which had as its objective the determination of the capture-to-fission ratio of  $^{239}\text{Pu}$  in a soft neutron spectrum. Five fission-track detectors and four 15-mg plutonium samples were included in the short irradiation (80 min), and four 15-mg samples of plutonium in the long irradiation (5 days). Because the irradiation times in this experiment were considerably shorter than those proposed for fission-yield determinations, the activity of  $^{140}\text{Ba}$  ( $t_{1/2} = 12.8$  days) was used to establish the necessary relationships between the two irradiations.

In this experiment, the number of fissions that occurred in the long irradiation was determined with an estimated accuracy of  $\pm 1.8\%$ . With refinements in technique it is expected that an accuracy comparable to that obtainable by the other methods, namely,  $\pm 1\%$ , can be obtained with the new method.

## REFERENCES AND FOOTNOTES

1. Mound Laboratory, Miamisburg, Ohio; operated by the Monsanto Research Corp. for the USAEC.
2. This work was a joint effort of personnel of the EBR-II Project and Pacific Northwest Laboratory.
3. G. R. Horn (PNL), *The Effects of Xenon on Fuel-to-Cladding Gap Conductivity*, Trans. Amer. Nucl. Soc. 12(2), 607 (1969).
4. D. E. Walker, P. I. Halfman, and J. H. Sanecki, "Xenon Tagging of Instrumented Fuel Capsules for Use in EBR-II," *Proc. Nat. Symp. Developments in Irradiation Testing Technology, Sandusky, Ohio, Sept. 9-11, 1969*, USAEC-NASA (in press).

## V. CHEMISTRY OF LIQUID METALS AND MOLTEN SALTS

Experimental and theoretical research studies on molten metals and salts, which have been in progress for several years, have been directed toward (1) understanding the behavior of liquid sodium as a coolant in nuclear reactors, (2) conducting basic research related to the development of electrochemical cells with liquid sodium and liquid lithium anodes, and (3) determining the thermodynamic and structural properties of fused salts.

The experimental program has centered around the determination of the thermodynamic properties and phase relationships for lithium- and sodium-containing binary systems and for fused alkali-halide systems by thermal-analysis, emf, solubility, and vapor-liquid equilibrium methods. In addition, measurements have been made of some structural and transport properties of fused alkali-halide mixtures. The electrochemistry of lithium/chalcogen cells has been investigated in some detail.

The theoretical program has been devoted to (1) developing a model for predicting gas solubilities in liquid metals, (2) developing an empirical equation which relates the surface tension of a liquid metal at absolute zero to its critical properties, and (3) applying and extending models for predicting phase diagrams of binary and multicomponent metal and salt systems.

Several goal-oriented secondary-battery programs are in progress. Specifically, they are the development of (1) an implantable lithium/selenium battery for powering artificial organs (National Heart Institute); (2) high-specific-power lithium/selenium batteries for military vehicle applications (U.S. Army, Ft. Belvoir, Va.); and (3) high-specific-power, high-specific-energy lithium/sulfur batteries for use in family automobiles (National Air Pollution Control Administration).

### A. STUDIES OF LIQUID METALS

Research is being directed toward broadening and systematizing knowledge of the liquid metallic state. Experimental and theoretical programs are being undertaken which include the determination of thermodynamic properties and phase diagrams for binary metallic systems, gas solubilities, and surface tensions, and the measurement of transport properties, such as electronic conductivity, of sulfur-, selenium-, and tellurium-containing liquids.

#### 1. Thermodynamics

##### a. The Sodium-Bismuth System

The sodium-bismuth system is of interest not only because of its potential application in energy-conversion

devices, but also because of its importance to sodium-cooled nuclear reactors. Moreover, it provides unique characteristics for testing solution theory in liquid metal solutions. The thermodynamic behavior of liquid sodium-bismuth alloys has been represented by two models. In the first model (see ANL-7550, p. 89), a preliminary attempt was made to apply the quasi-ideal solution theory to the calculation of a solid-liquid equilibrium curve. The model incorporated the following assumptions: (1) The species present are Na, Bi, NaBi, and  $\text{Na}_3\text{Bi}$ ; (2) the heat of fusion of  $\text{Na}_3\text{Bi}$  is 11,100 cal/mol. The second model included the dimer  $\text{Na}_2$  and tetramer  $\text{Na}_4$  in addition to the species already stipulated. The calculated solid-liquid equilibrium curves for both models are shown in Fig. V-1. The curve for the second (tetramer) model agrees well with the experimental data. However, when the calculations incorporated a

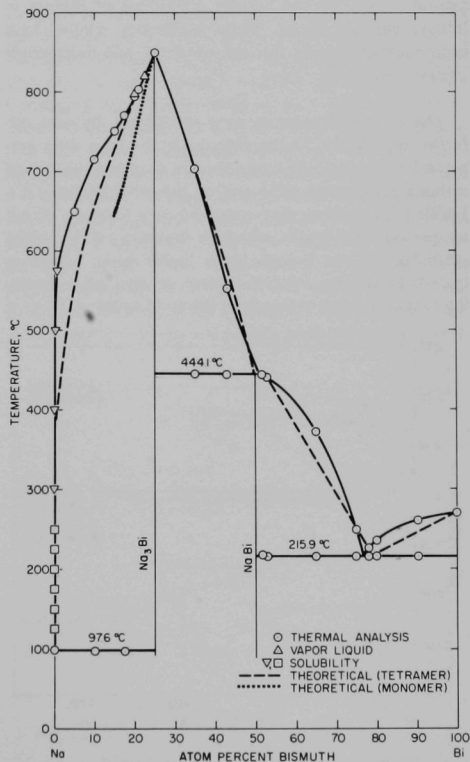


Fig. V-1. Solid-Liquid Phase Diagram for the Sodium-Bismuth System.

recently determined value for the heat of fusion of  $\text{Na}_3\text{Bi}$ , namely, 7085 cal/mol (see Sect. III.B.1 of this report), the agreement between the experimental data and the quasi-ideal solution model was not as good as that shown in the figure, particularly for the  $\text{Na}_3\text{Bi}$  peak. The calculated diagram showed a narrow compositional range for the liquidus-solidus peak. Additional work is needed to resolve this difference between model and real systems.

### b. The Lithium-Selenium System

The determination of the thermodynamic behavior of lithium-selenium alloys is important to an understanding of the interactions of elements of widely differing electro-negativities, and thermodynamic data are necessary for predicting the ideal performance of cells in which such alloys serve as the cathode material. The lithium-selenium system has been investigated by a variety of methods. Emf measurements of cells of the type  $\text{Li}/\text{LiX}/(\text{Li in Se})$  have yielded values for the activity coefficient of lithium in lithium-selenium alloys. Phase-equilibrium studies have been conducted using thermal, chemical, and microscopic analysis techniques.

The emf measurements were carried out by two different approaches. In the first, cathode alloys were prepared by mixing  $\text{Li}_2\text{Se}$  with selenium to obtain the desired cathode composition. The emf of the cell  $\text{Li}(\text{Q})/\text{LiF-LiCl-LiI}(\text{Q})/(\text{Li in Se})$  was then measured as a function of cell temperature. The results, which are shown in Fig. V-2 (solid symbols), indicate a single-phase liquid region extending from 0 to perhaps 10 at. % lithium in selenium, a liquid-liquid immiscibility region from below 15 to about 32 at. %

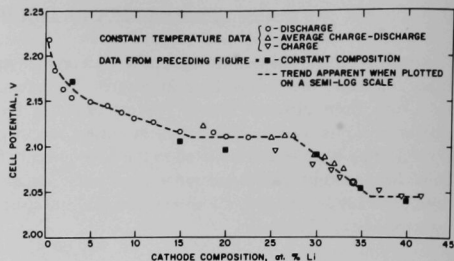


Fig. V-3. Emf of the Cell  $\text{Li}(\text{Q})/\text{LiF-LiCl-LiI}(\text{Q})/(\text{Li in Se})$  as a Function of Cathode Composition (temperature =  $390^\circ\text{C}$ ).

lithium, and a liquid-solid region above 40 at. % lithium for the temperature range  $360$  to  $475^\circ\text{C}$ . In the second approach, the cell was operated at a fixed temperature and the composition was changed by controlled discharge of the cell. The results of this approach at  $390^\circ\text{C}$  are shown in Fig. V-3 (open symbols); the figure also includes data (solid symbols) from the first approach for comparison. (Conversely, open symbols in Fig. V-2 are data from the second approach.) The data obtained by the two methods are in good agreement.

The activity coefficient of lithium in selenium at 0.5 at. % lithium is  $3.03 \times 10^{-15}$  at  $390^\circ\text{C}$ . The emf plateau in Fig. V-3 that extends from 36 at. % lithium to higher concentrations corresponds to the precipitation of solid  $\text{Li}_2\text{Se}$  from the cathode alloy; this emf corresponds to a free energy of formation of solid  $\text{Li}_2\text{Se}$  from lithium and selenium in 36 at. %  $\text{Li-Se}$  at  $390^\circ\text{C}$  of  $-94.3$  kcal/mol.

The results of the phase-equilibrium studies and the method of analysis (thermal, chemical, or microscopic) by which the data were obtained are given in Fig. V-4. These preliminary data have been interpreted in terms of a simple monotectic system. It should also be noted that room-temperature X-ray analysis of a number of samples of various compositions and thermal histories have given no evidence of intermediate phases other than  $\text{Li}_2\text{Se}$ .

The reasons for the discrepancies between the phase boundaries indicated by the emf studies and those indicated by the other experiments are not clear. The disagreement is most pronounced at the selenium-rich boundary of the miscibility gap ( $\sim 10$ - $15$  at. %  $\text{Li}$  from emf studies vs.  $\sim 2$  at. %  $\text{Li}$  from phase-equilibrium studies). Supersaturation in the emf cells is one possible explanation.

### c. Solubilities of $\text{Li}_2\text{S}$ , $\text{Li}_2\text{Se}$ , and Selenium in Fused Lithium Halides

The solubilities of  $\text{Li}_2\text{S}$ ,  $\text{Li}_2\text{Se}$ , and selenium in molten lithium halides have been measured at various temperatures.

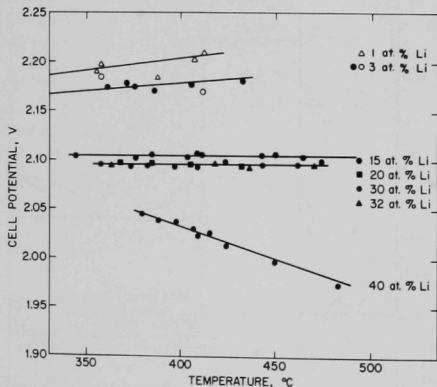


Fig. V-2. Emf of the Cell  $\text{Li}(\text{Q})/\text{LiF-LiCl-LiI}(\text{Q})/(\text{Li in Se})$  as a Function of Temperature (solid symbols indicate  $\text{Li-Se}$  alloys made by dissolving solid  $\text{Li}_2\text{Se}$  in selenium; others obtained by the controlled deposition of lithium in selenium).



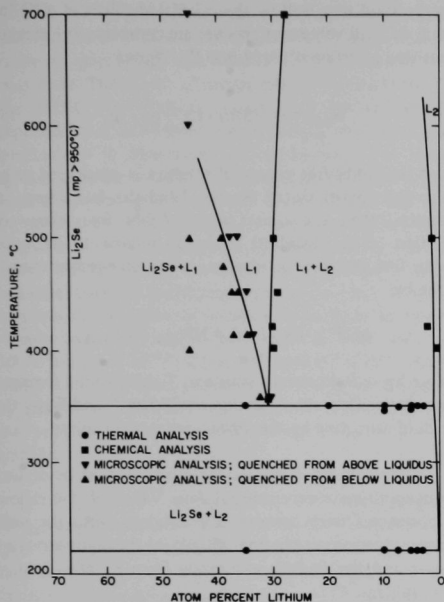


Fig. V-4. Partial Phase Diagram for the Lithium-Selenium System.

The metal or intermetallic compound was equilibrated at each temperature with the selected lithium halide, and filtered samples were taken. (The experimental apparatus provided a uniform temperature zone throughout the molten salt.) The solubilities of  $\text{Li}_2\text{S}$ ,  $\text{Li}_2\text{Se}$ , and selenium, determined from chemical analysis of the samples, are given in Fig. V-5. Also included in the figure, for comparison, are (1) previously determined solubilities (see ANL-7316, p. 119) for  $\text{Li}_2\text{Te}$  and two lithium-bismuth compounds and (2) the solubility of lithium from the data of Dworkin, Bronstein, and Bredig.<sup>1</sup>

The solubility of selenium in molten  $\text{LiF-LiCl}$  was unexpectedly low compared with the solubility of selenium in  $\text{LiF-LiCl-Li}$ . Solubility measurements<sup>2</sup> for  $\text{Na}_3\text{Bi}$  in  $\text{NaI}$  and in  $\text{NaCl-NaI}$  indicate that the solubility of  $\text{Na}_3\text{Bi}$  at a given temperature increases with increasing concentration of  $\text{NaI}$ . Thus, it appears that the presence of iodide increases the solubility of some metals and intermetallic compounds in alkali halide melts.

#### d. Theoretical Study of Gas Solubility in Liquid Metals

To begin to understand the complex corrosion phenomena associated with the use of sodium as a coolant in fast

breeder reactors, the fundamental behavior of sodium as a solvent must be studied in detail. In turn, to unravel the interrelated factors involved in sodium's role as a solvent, it is desirable to begin with a study of the most simple solutes, namely, the noble gases. By so doing, the contributions to the work required for the insertion of a single atom of a neutral solute species into a liquid metal can be conceptualized and can be separated from the additional contributions to the work of solution that arise with more complex solutes. As a start, a simple model describing the thermodynamics of solution of noble gases in liquid sodium will be presented and compared with experimental results.

In this model, the excess free energy of formation of a dilute solution is set equal to the difference of two terms: the electronic work done on the solvent in creating within it a cavity (or bubble) of appropriate size to accommodate the solute atom, less the attractive work done by the solute atom when on insertion into this cavity it polarizes the surrounding solvent atoms. The electronic work, being by far the larger term, will be given primary attention; for its calculation the work of Fumi<sup>3</sup> (on the formation energy of vacancies in solid metals) provides an excellent basis. Consider a monovalent metal to be a spatially uniform, immobile distribution of positive charge corresponding to  $N$  positive ions, neutralized by  $N$  free, mobile valence electrons, all contained in a spherical volume  $V$ .<sup>4</sup> (This is the well-known "jellium" model.) Now, remove from the center a small spherical volume,  $\delta V$ , of positive charge and distribute it uniformly over the surface of the sphere, leaving a cavity. Two effects occur. First, the excess negative charge in the cavity ( $= \delta V/\Omega$ , where  $\Omega$ , the atomic volume, is  $V/N$ ) repels, by a screened Coulombic potential, all the electrons in the conduction band and increases their

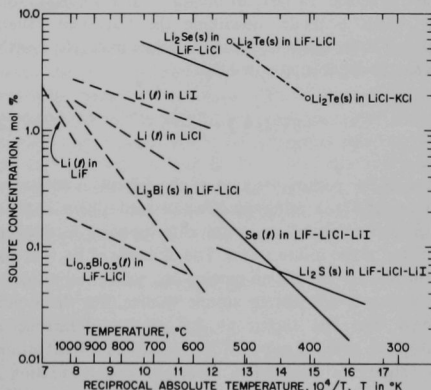


Fig. V-5. Solubilities of Lithium, Selenium, and Several Intermetallic Compounds of Lithium in Alkali Halide Mixtures.

potential energy. The amount of work done is equal to two-thirds the maximum kinetic or Fermi energy,  $E_f$ , per electron times the excess negative charge in the cavity:<sup>5</sup>

$$W_{\text{rep}} = (2/3)E_f \frac{\delta V}{\Omega}. \quad (1)$$

Secondly, the expansion of the sphere reduces the average kinetic energy per electron of the valence electrons. For free electrons  $\bar{E}_{\text{kin}} = (3/5)E_f$ , and since  $E_f$  varies as  $V^{-2/3}$ ,  $\delta E_f/E_f = -(2/3)(\delta V/V)$ . Hence,

$$\begin{aligned} W_{\text{kin}} &= \Delta \bar{E}_{\text{kin}} = (3/5)N\delta E_f \\ &= (3/5)N[-(2/3)\frac{\delta V}{V}E_f] \\ &= -(2/5)E_f \frac{\delta V}{\Omega}. \end{aligned} \quad (2)$$

So in total,

$$W_{\text{cav}} = (2/3)E_f \frac{\delta V}{\Omega} - (2/5)E_f \frac{\delta V}{\Omega} = (4/15)E_f \frac{\delta V}{\Omega}. \quad (3)$$

The Fumi model for the work of formation of a cavity in a monovalent metal has been shown<sup>6</sup> to be valid for solid metals by comparing  $W_{\text{cav}}$  to known energies for vacancy formation. The result appears to be good to within 10% provided allowance is made for the fact that in solid metals the lattice can relax in the neighborhood of the vacancy. Since the Fumi model is a reasonable description of the energetics of vacancy formation and does not depend on lattice structure, it may be directly applied to the problem of creating a cavity in a liquid metal to accommodate a solute molecule. In fact, to obtain a value for  $W_{\text{cav}}$ , one only needs a model describing the fractional volume change,  $\delta V/\Omega$ , upon introducing a solute molecule. For the present model, it is proposed that

$$\delta V/\Omega = 1 + \frac{\pi}{6} \frac{\sigma^3}{\Omega} \cdot \eta, \quad (4)$$

where  $\eta$ , the packing fraction of the solvent, is equivalent to  $(\pi/6)(a^3/\Omega)$ ,  $a$  being the effective hard-sphere diameter of the solvent atoms, and  $\sigma$  the corresponding hard-sphere diameter of the solute atoms. The rationale of Eq. 4 is that the increase in volume on moving one solvent atom out to the surface is not just an atomic volume, but the atomic volume plus the increment due to the difference in hard-sphere volumes between the solute and solvent atoms. The validity of hard-sphere theory in this connection is supported by the correct prediction of the location and height of the first peaks in the experimental liquid structure factors  $a(K)$  for both metals<sup>7</sup> and noble gases. These peaks

are matched very well by the calculated values of  $a(K)$  for fluids of hard spheres of appropriate diameters and number densities. Insertion of Eq. 4 into Eq. 3 gives

$$W_{\text{cav}} = (4/15)E_f \left(1 + \frac{\pi}{6} \frac{\sigma^3}{\Omega} \cdot \eta\right). \quad (5)$$

If the Gibbs free energy of solution is considered to be very well approximated by the Helmholtz free energy of solution, then the excess molar Gibbs free energy of solution of the dissolved noble gas relative to its molar Gibbs free energy as an ideal gas at the same temperature is given by

$$\Delta G^{\text{XS}} = -Nk_B T \ln \lambda = N W_{\text{cav}} - N W_{\text{attr}}, \quad (6)$$

where  $k_B$  is Boltzmann's constant,  $T$  the absolute temperature,  $\lambda$  the Ostwald solubility coefficient,<sup>8</sup> and  $W_{\text{attr}}$  the work of attraction by the solvent per atom of solute.

To evaluate Eq. 6, values for  $\eta$  and  $\sigma$  must be derived from appropriate experimental data. Values of  $\eta$  at various temperatures were conveniently obtained from the well-known thermodynamic limit ( $K \rightarrow 0$ ) for the liquid structure factor and the limiting expression for  $a(K)$  of a fluid of hard spheres,<sup>7,9</sup> i.e.,

$$a(0) = \rho k_B T \chi_T = (1 - \eta)^4 / (1 + 2\eta)^2, \quad (7)$$

where  $\chi_T$  is the isothermal compressibility of the solvent and  $\rho$  its number density. The length parameter in the Lennard-Jones 6-12 potential, which has been used to fit second virial coefficient data for the noble gases,<sup>10</sup> was chosen as the value for  $\sigma$ . This particular choice is justified because the location and height of the first peak in  $a(K)$  for a fluid of hard spheres of this constant diameter matches that for liquid krypton at several intervals in the temperature range 117-183°K.<sup>11</sup>

Calculated values of  $N W_{\text{cav}}$  for helium, argon, or krypton dissolved in sodium are compared with experimental data for  $\Delta G^{\text{XS}}$  in Table V-1. The errors assigned to the experimental data for helium and argon are our estimates; however, because of the possibility of systematic

TABLE V-1. Molar Excess Gibbs Free Energies of Solution of Noble Gases Dissolved in Liquid Sodium at 400°C

Gas	$\Delta G^{\text{XS}}(\text{exptl})^a$	$N W_{\text{cav}}(\text{calcd})^a$
He	$12.5 \pm 0.1^b$	14.6
Ar	$17.1 \pm 0.3^c$	19.2
Kr	$19.1^d$	20.7

<sup>a</sup>In kcal/mol.

<sup>b</sup>E. Veleckis, ANL, private communication.

<sup>c</sup>E. Veleckis, R. Blomquist, R. Yonco, and M. Perin,

ANL-7325, p. 128.

<sup>d</sup>S. K. Dhar, ANL-6900, p. 125.

error in the krypton data, error limits were not assigned. The agreement between the experimental and calculated values is quite good with respect to sign, sequence, and magnitude. The results of similar calculations made for 300 and 500°C (not shown) indicate that the temperature dependence of  $\Delta G^{XS}$  given by the  $NW_{cav}$  term is, at least, qualitatively in agreement with experiment. The overall agreement is particularly gratifying since previous theoretical models that ignored the specifically metallic nature of the solvent, e.g., the Hildebrand solubility parameter, failed to give even order-of-magnitude agreement for  $\lambda_0$ . Furthermore, the nature of the agreement encourages us to calculate Ostwald coefficients for xenon prior to actual measurement because of xenon's importance in nuclear reactor technology. The coefficients at 300, 400, and 500°C are  $8.1 \times 10^{-10}$ ,  $2.5 \times 10^{-8}$ , and  $3.3 \times 10^{-7}$ , respectively, when the values calculated for  $NW_{cav}$  are decreased by 2 kcal/mol. This correction was made to compensate for the apparent systematic overestimate of  $\Delta G^{XS}$  by this amount.

It is premature to conclude that the excess of  $NW_{cav}(\text{calcd})$  over  $\Delta G^{XS}(\text{exptl})$  is, in fact, indicative of a term  $NW_{attr}$  of the order of 2 kcal/mol. It is difficult to calculate  $NW_{attr}$  from simple principles. In addition, more detailed consideration must be given to the value 4/15 in Eqs. 3 and 5. However, the success of this simple model justifies refinements which could lead to better agreement with experiment for the monovalent metals, and which are considered essential to the extension of the model to polyvalent metals. The density of states for conduction electrons in metals is nonparabolic in the wave vector  $k$  as a result of the interaction of the electrons with locally attractive ionic potentials. Therefore, the valence electrons are not completely free in the metal, and their average kinetic energy relative to the bottom of the conduction band may be different from the free-electron value  $(3/5)E_f$ . Furthermore, the contribution of  $(2/3)E_f$  to Eqs. 1 and 3, arising from the screened repulsive interaction between the conduction electrons and the excess electronic charge in the cavity, is known to be correct to first order in perturbation theory, but higher-order terms may be significant. Some or all of these approximations may not be valid for polyvalent metals, and this is being investigated.

#### e. Surface Tension and Critical Properties of Liquid Metals

The principle of corresponding states was applied to the surface tension of liquids by Guggenheim<sup>12</sup> in 1945. By analysis of surface tension and critical-property data for "simple" liquids such as the heavier noble gases, nitrogen, and oxygen, Guggenheim<sup>12,13</sup> obtained the relation

$$\gamma_0 V_c^{2/3} = K T_c, \quad (8)$$

where  $\gamma_0$  is surface tension extrapolated to absolute zero,  $V_c$  is the critical molar volume,  $T_c$  is the critical temperature, and  $K$  is a universal constant equal to 4.3 erg/(°K)(mol<sup>2/3</sup>).

Surface tension and critical-property data have since become available for mercury and the alkali metals.<sup>14-19</sup> These are shown in Table V-2 together with the values for  $\gamma_0 V_c^{2/3}/T_c$  calculated according to Eq. 8. Clearly  $\gamma_0 V_c^{2/3}/T_c$  is not a constant for these liquid metals, but has a value consistently smaller than that for the simple liquids. Thus, Eq. 8 is not valid for liquid metals, i.e., the surface tension of liquid metals does not follow the principle of corresponding states.

Because Eq. 8 cannot be applied to liquid metals, a new empirical relationship between  $\gamma_0$ ,  $V_c$ , and  $T_c$  was sought. The equation

$$\gamma_0 (V_c - B)^{2/3} = A T_c, \quad (9)$$

where  $A$  and  $B$  are constants, was found to relate these three properties accurately. The equation may be rewritten

$$(T_c/\gamma_0)^{3/2} = A^{-3/2} (V_c - B). \quad (10)$$

Its validity for mercury and the alkali metals is evident in Fig. V-6 by the linearity of a plot of  $(T_c/\gamma_0)^{3/2}$  versus  $V_c$  for the data in Table V-2. From the intercept of the line on the  $V_c$ -axis, the constant  $B$  is 31 cm<sup>3</sup>/mol; from the slope of the line, the constant  $A$  is 1.67 erg/(°K)(mol<sup>2/3</sup>). Both constants were derived by least-squares analysis. The dashed line in Fig. V-6 is for simple liquids that follow the principle of corresponding states. Equations 8 and 9 differ in that  $K$  is about 2.5 times larger than  $A$ , and  $B = 0$  for simple liquids.

The critical volumes and temperatures of other liquid metals can be estimated from Eq. 9 and the law of the rectilinear diameter<sup>12</sup> as follows. The value of  $\gamma_0$ , obtained by extrapolating the surface tension of the liquid metal to absolute zero, is inserted into Eq. 9 together with the values for the constants  $A$  and  $B$ . This fixes one relationship between  $T_c$  and the critical density  $\rho_c = M/V_c$ , where  $M$  is the molar mass. A second relationship between  $T_c$  and  $\rho_c$  is given by the law of the rectilinear diameter, which states

TABLE V-2. Test of the Principle of Corresponding States

Metal	$\gamma_0$ (erg/cm <sup>2</sup> )	$V_c$ (cm <sup>3</sup> /mol)	$T_c$ (°K)	$\gamma_0 V_c^{2/3}/T_c$ [erg/(°K)(mol <sup>2/3</sup> )]
Hg	545(14)	43(17,18)	1763(16)	3.79
Li	470(15)	66(19)	3223(19)	2.38
Na	220(15)	116(19)	2573(19)	2.03
K	125(15)	209(19)	2223(19)	1.98
Rb	95(15)	247(19)	2093(19)	1.79
Cs	80(15)	311(19)	2057(19)	1.79

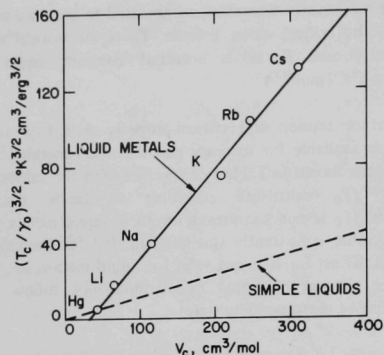


Fig. V-6.  $(T_c/\gamma_0)^{3/2}$  versus  $V_c$  for Liquid Metals. (Included for comparison is a similar plot for simple liquids that follow the principle of corresponding states.)

that the average density of the liquid and vapor phases,  $\bar{\rho} = (\rho_L + \rho_V)/2$ , is a linear function of temperature and passes through the critical point  $(T_c, \rho_c)$ . The latter relationship can be established accurately from low-temperature liquid densities, since at low temperatures  $\bar{\rho} \approx \rho_L/2$ , and it can be extrapolated reliably to higher temperatures because of its linearity. If the two relationships are constructed on a density vs. temperature plot, then  $\rho_c$  and  $T_c$  can be found from their intersection. This is illustrated in Fig. V-7 with data for liquid iron; the two curves intersect at  $T_c = 6500^\circ\text{K}$  and  $\rho_c = 1.42 \text{ g/cm}^3$ , giving  $V_c = 39 \text{ cm}^3/\text{mol}$ .

This technique of solving two simultaneous equations in the critical properties was used to estimate  $\rho_c$ ,  $V_c$ , and  $T_c$  for a variety of liquid metals whose densities and surface tensions as functions of temperature are known. The results are shown in Table V-3.

It is important that these estimates be put into proper perspective with respect to historical developments in this

area and to their probable reliability. Until recent years, mercury was the only metal whose critical properties were known. Estimates<sup>20</sup> of the critical properties of other metals had been based on data for mercury and the principle of corresponding states. However, measurement of the critical properties of the alkali metals<sup>19</sup> showed that the liquid and vapor densities and the heats of vaporization of these metals were not related as predicted by the principle of corresponding states. Moreover, the present work extends this conclusion to the surface tension as well. Hence, application of the principle to estimation of critical properties is of dubious validity. The technique of estimation presented here is based not only on data for mercury, but on data for all metals whose critical properties are known at this time. This is probably an improvement over corresponding-state methods, but there is no assurance that other liquid metals will have  $\gamma_0$ ,  $V_c$ , and  $T_c$  values accurately related by Eq. 9. Thus the validity of this relationship should be reassessed as future measurements of the critical properties of metals are made. In the meantime,

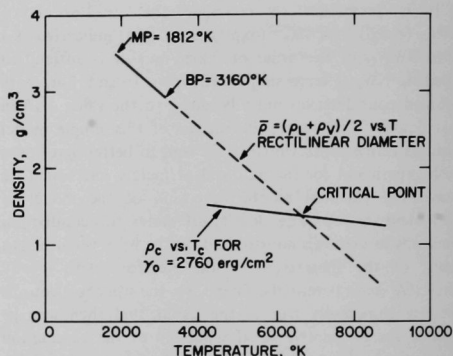


Fig. V-7. Graphical Estimation of the Critical Density and Temperature for Liquid Iron from the Law of the Rectilinear Diameter and the Relationship between Surface Tension and Critical Properties for Liquid Metals.

TABLE V-3. Estimated Critical Properties of Liquid Metals

Metal	$\rho_0$ (g/cm <sup>3</sup> )	$-10^4 d\rho/dT$ [g/(cm <sup>3</sup> )(°K)]	$\gamma_0$ (erg/cm <sup>2</sup> )	$\rho_c$ (g/cm <sup>3</sup> )	$V_c$ (cm <sup>3</sup> /mol)	$T_c$ (°K)
Mg	1.834	2.647	721	0.438	56	3600
Sr	2.648	2.62	392	0.850	103	4000
Ba	3.59	2.74	351	1.36	101	3600
Al	2.659	3.11	996	0.427	63	6000
In	7.315	6.798	602	0.77	149	8600
Tl	12.15	15.2	536	2.11	97	5200
Sn	7.309	6.127	581	0.65	183	9900
Pb	11.469	13.174	538	1.94	107	5800
Bi	10.665	11.820	423	1.18	177	7000
Fe	8.618	8.83	2758	1.42	39	6500
Ni	9.908	11.589	2348	1.38	42	6100
Cu	9.007	4.003	1629	1.10	58	8600
Ag	10.465	9.067	1139	1.83	59	6200
U	19.356	10.328	1747	3.30	72	12400

the approach outlined here provides critical-property estimates of sufficient reliability for many scientific and engineering purposes.

## 2. Transport Properties: Electronic Conductivity of Selenium- and Sulfur-containing Cathode Alloys

Little information is available on the electronic conductivity of liquid elemental semiconductors and the effects of temperature and dopants on conductivity. Theory<sup>21</sup> indicates that amorphous and liquid semiconductors should be less sensitive to doping than crystalline semiconductors, but the magnitude of the effect cannot yet be predicted. Because suitable experimental data are lacking and because future portable power sources may rely heavily on liquid semiconducting elements as cathode materials, the effects of doping on liquid selenium and sulfur are being studied.

### a. Selenium

The conductivities of liquid selenium and selenium-tellurium alloys containing up to 26 at. % tellurium have been measured. The conductivity cell consisted of a pair of spectrographic graphite rods sealed in quartz tubes. The tubes were fused parallel to one another and mounted on a micrometer-controlled stand to provide a constant inter-electrode distance and a measurable immersion depth. The cell constant was determined to be  $0.3150 \text{ cm}^{-1}$ . Conductivities were measured with an impedance bridge at an ac frequency of 1 kHz; measurements were carried out over the temperature range 300 to 400°C in a high-purity helium atmosphere. The selenium and tellurium were specified as 99.999% pure.

In Fig. V-8, our data for the conductivity of pure selenium as a function of temperature are compared with those of other workers.<sup>22-26</sup> Our results are in excellent agreement with those of Henkels<sup>22,23</sup> and Lizell,<sup>24</sup> whereas the values of Baker<sup>25</sup> and of Watanabe and Tamaki<sup>26</sup> are higher and lower, respectively.

The conductivities of several selenium-tellurium alloys are also given as a function of temperature in Fig. V-8. These results were extrapolated to 500°C (assuming a constant activation energy for conduction in the range of 300 to 500°C), and compared with those of other workers.<sup>27,28</sup> The extrapolated values from the present study were in very good agreement with the data of Perron,<sup>27</sup> who studied the conductivities at the tellurium-rich concentrations.

### b. Sulfur

The conductivities of liquid sulfur and sulfur-rich mixtures have been determined as a function of temperature

and composition. Measurements were made with a Jones electrolytic bridge operated at an ac frequency of 1 kHz. Most of the measurements were made in the temperature range from 220 to 420°C. Experimental accuracies of the conductivity measurements were limited due to the high volatility of liquid sulfur; the error limits were estimated to be approximately  $\pm 10\%$  at temperatures above 260°C and  $\pm 50\%$  at temperatures below 260°C. (The larger error limits associated with the measurements below 260°C resulted from the use of a shunt in parallel with the cell.)

Conductivities were measured for two different grades of sulfur, namely, sublimed sulfur (N.F.) supplied by Mallinckrodt Chemical Works (no purity specification available) and sulfur of 99.999+ % purity obtained from

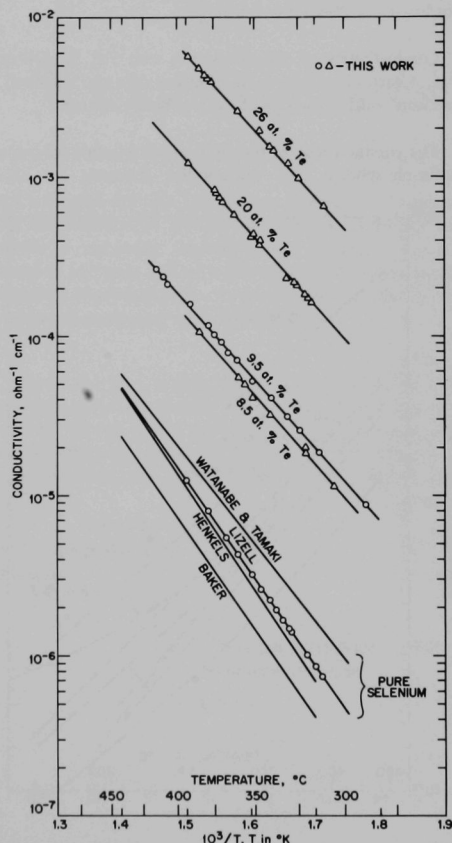


Fig. V-8. Conductivity of Selenium and Selenium-Tellurium Alloys as a Function of Temperature.

American Smelting and Refining Co. The results for both materials are given in the lower portion of Fig. V-9. The change in the slope of the curve for high-purity sulfur with changing temperature indicates that even this grade of sulfur may not be free of impurities. Our data differ from the extrapolated values of Feher and Lutz,<sup>29</sup> and from the findings of Watanabe and Tamaki<sup>26</sup> and of Kraus and Johnson.<sup>30</sup> However, the validity of the extrapolation of Feher and Lutz's data over a wide range of temperature is questionable.

The conductivities of several sulfur-tellurium mixtures and one sulfur-selenium mixture are also included in Fig. V-9 (as dashed lines). In the case of sulfur-tellurium mixtures, a plot of conductivity as a function of composition at constant temperature indicates that these curves are not linear near the sulfur-rich end.

Conductivities of sulfur mixtures with 5 at. % each or 9 at. % each of selenium and tellurium were also measured, and were roughly the sum of the two binary systems.

The conductivities as functions of temperature for some sulfur-phosphorus and sulfur-iodine mixtures are also

shown in Fig. V-9. The addition of phosphorus or iodine produced considerably larger increases in the conductivity of sulfur than did equal additions of tellurium or selenium. This result may be due to the extrinsic nature of conduction in the S-P and S-I mixtures, compared with the intrinsic conduction mechanism in S-Se and S-Te mixtures. Such extrinsic conduction predominates at the lower temperatures, as is exhibited by the S-P and S-I mixtures.

Preliminary conductivity measurements have also been made of lithium-sulfur mixtures. The data indicate that a highly conducting (probably lithium-rich) phase appears at  $375 \pm 10^\circ\text{C}$ .

## B. STUDIES OF MOLTEN SALTS

Because of the extensive use of molten salts in industrial applications, the understanding of their physicochemical, thermodynamic, and structural properties has become increasingly important. The program to study these properties has been concerned primarily with determining the phase relationships of binary and multicomponent systems, and with elucidating the structure of these systems. Attention has also been given to the characterization and analysis of paste electrolytes and filler materials (used in the battery program).

### 1. Thermodynamics: Phase Diagrams of Lithium Halide-containing Systems

The feasibility of using low-melting mixed-cation electrolytes in electrochemical cells is being investigated. Electrolytes for such cells would utilize mixtures of lithium halides with other alkali halides (excluding sodium), since these have suitably low-melting eutectics and appropriate thermodynamic stabilities.

Lumsden<sup>31</sup> has developed a method of estimating the thermodynamic data for binary alkali-halide systems with a common anion; these data can be used to calculate the requisite binary phase diagram. Using a regular solution model, Lumsden expressed the liquidus temperature of component *i* as

$$T_i = \frac{KN_i^2 + \Delta H_{mi}}{\Delta S_{mi} - R \ln N_i} \quad (1)$$

where  $\Delta H_{mi}$  and  $\Delta S_{mi}$  are the heat and entropy of fusion of component *i*, *N* is the mole fraction, and *K* is an interaction parameter calculated from London forces, polarization forces, and the interionic distances for each salt.

Lumsden's model was used to calculate the phase diagrams for the LiI-KI and LiI-RbI systems.<sup>32</sup> A minimal

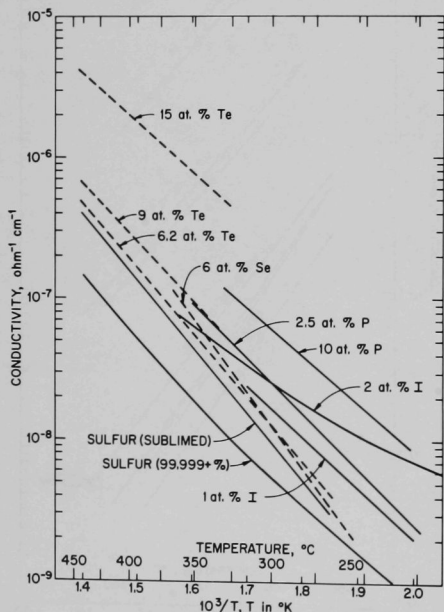


Fig. V-9. Conductivity of Sulfur and Sulfur-containing Mixtures as a Function of Temperature (mixtures made with sublimed sulfur except for 2% I mixture).



number of thermal-analysis data points were necessary to map the phase diagrams because of the guidance given by the calculated diagrams. The data for the LiI-KI system are given in Fig. V-10, along with the available literature data<sup>3,3,4</sup> for the system; the data for the LiI-RbI system are given in Fig. V-11.

The agreement between the calculated and experimentally determined phase diagrams is very good, especially for the LiI-RbI system, even though the 1:1 compound LiI·RbI forms. The compound LiI·RbI raises the minimum temperature only 25°C above that obtained in the calculation. It is clear that the model proposed by Lumdsen can

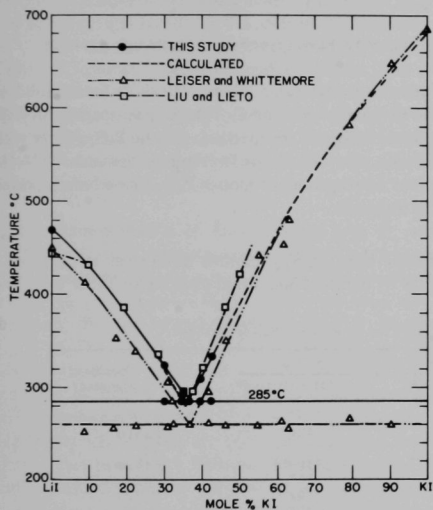


Fig. V-10. Solid-Liquid Phase Equilibria for the LiI-KI System.

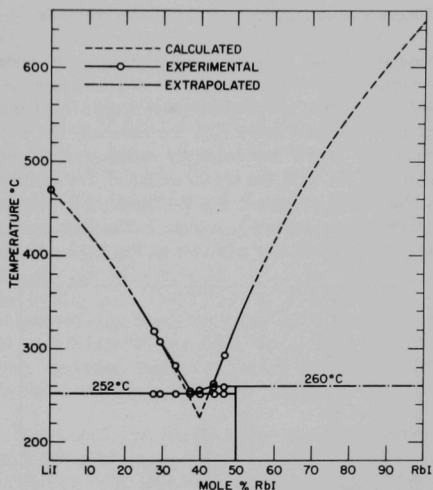


Fig. V-11. Solid-Liquid Phase Equilibria for the LiI-RbI System.

offer a significant reduction in experimental effort required for the selection of low-melting mixtures. Although this model is rigorously applicable only to simple eutectic systems, our work indicates that reasonable success can be expected in predicting the behavior of alkali-halide systems even when compound formation occurs.

Since the two binaries LiI-KI and LiI-RbI had low-melting eutectics, several ternary and multicomponent systems having these pairs as constituents were also investigated, and mixtures having even lower melting points were identified. The results of this study are summarized in Table V-4.

TABLE V-4. Low-melting Lithium Halide Mixtures

System/Composition (mol %)	Liquidus Temp (°C)	Peritectic Temp (°C)	Eutectic Temp (°C)	Remarks
LiI - RbI - CsI 60 20 20	232	≈230	≈227	Peritectic and eutectic occur close to each other
LiI - KI - CsI 60 18 22	207	-	204	Composition close to eutectic composition
LiBr - LiI - KI - CsI 9.6 54.3 16.2 19.9	194	-	189	Composition close to eutectic composition
LiCl - LiBr - LiI - KI - CsI 3.45 9.25 52.4 15.7 19.2	186	-	184	Composition close to eutectic composition

## 2. Structure Investigations by Spectroscopic Methods

Several of the phosphorus-sulfur compounds under investigation as cathode substances for electrochemical cells have been investigated by Raman spectroscopy. The Raman spectra of solid and liquid  $P_4S_3$  are essentially the same except that several low-frequency lattice modes were observed for the solid, but not for the liquid. The spectrum of molten  $P_4S_3$  is shown in Fig. V-12, and the frequencies are tabulated in Table V-5, column 3. The Raman spectrum for molten  $P_4S_{10}$  is shown in Fig. V-13, and the

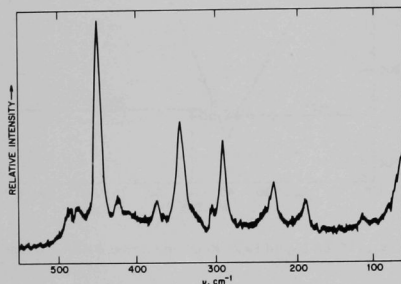


Fig. V-12. Raman Spectrum of Liquid  $P_4S_3$  (200°C).

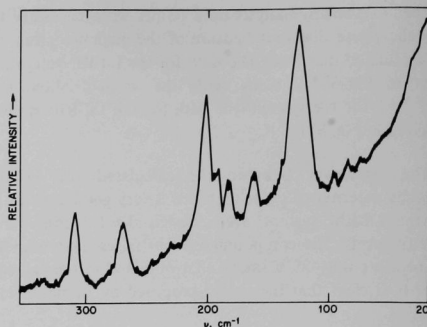


Fig. V-13. Raman Spectrum of Liquid  $P_4S_{10}$  (340°C).

frequencies are tabulated, along with those for the solid, in Table V-5, columns 1 and 2. The Raman spectra of solid and liquid  $P_4S_3$  and the spectrum of solid  $P_4S_{10}$  agree with previously reported results for these compounds.<sup>35,36</sup> No previous investigations of molten  $P_4S_{10}$  have been reported in the literature.

Unlike  $P_4S_3$ ,  $P_4S_{10}$  exhibits differences in the Raman spectra of the solid and liquid phases (see Table V-5). The

TABLE V-5. Composite of Raman Frequencies ( $cm^{-1}$ ) for the Phosphorus-Sulfur System<sup>a</sup>

$P_4S_{10}$		$P_4S_3$ Liquid	Liquid 85 at. % P-15 at. % S		Species Assignment
Solid	Liquid		Before Heating <sup>b</sup>	After Heating <sup>c</sup>	
42,54,66	-	-	-	-	Lattice modes
128	126 s	-	-	126	$P_4S_{10}$
-	-	-	151	-	S8
163	163 m	-	-	(163) <sup>d</sup>	$P_4S_{10}$
185	183 m	187 m	-	185	$P_4S_3$ , $P_4S_{10}$
197	202 s	-	-	202	$P_4S_{10}$
-	-	-	-	214	e
-	-	-	221	-	S8
-	-	227 m	-	225	$P_4S_3$
-	-	-	-	233	e
-	-	-	-	238	e
-	-	-	-	244	e
-	-	-	-	262	e
274	268 m	-	-	267	$P_4S_{10}$
-	-	292 s	-	290	$P_4S_3$
310	308 m	-	-	305	$P_4S_{10}$
-	-	347 s	-	346	$P_4S_3$
-	-	-	-	358	e
-	-	377 w	366	366	P4
401	-	-	-	375	$P_4S_3$
-	-	-	-	-	Solid $P_4S_{10}$
-	-	425 w	-	407	e
-	-	451 s	-	425	$P_4S_3$
-	-	-	-	451	$P_4S_3$
-	-	-	465	465	P4
-	-	490 w	479	-	S8
-	-	-	-	490	$P_4S_3$
697	-	-	605	605	P4
726	-	-	-	-	Solid $P_4S_{10}$
-	-	-	-	-	Solid $P_4S_{10}$

<sup>a</sup>s = strong intensity; m = medium intensity; w = weak intensity.

<sup>b</sup>Spectrum of liquid eutectic at 25°C before temperature cycling to 200°C.

<sup>c</sup>Spectrum of liquid eutectic at 25°C after temperature cycling to 200°C.

<sup>d</sup>Observed as a shoulder on the 185  $cm^{-1}$  band.

<sup>e</sup>Probably associated with polyphosphide or a phosphorus-sulfur compound other than  $P_4S_{10}$  or  $P_4S_3$ .

absence of any bands above  $400\text{ cm}^{-1}$  in the liquid indicates that, on melting, the P-S terminal bonds in  $\text{P}_4\text{S}_{10}$  undergo some cross-linking. The inner cage structure of  $\text{P}_4\text{S}_{10}$  (the  $\text{P}_4\text{S}_6$  portion) is not affected by this cross-linking, as evidenced by the similarity in the Raman data below  $400\text{ cm}^{-1}$  for the solid and liquid phases. In  $\text{P}_4\text{S}_3$ , the bands below  $400\text{ cm}^{-1}$  are also attributed to the P-S-P network, and those in the region of  $400$  to  $500\text{ cm}^{-1}$  are assigned to vibrations of the equilateral triangular base formed by three phosphorus atoms.

The eutectic  $85\text{ at. \% P-15 at. \% S}$  (mp,  $<25^\circ\text{C}$ ) has also been investigated by Raman spectroscopy. Spectral data at  $25^\circ\text{C}$  for this mixture (prepared at  $40^\circ\text{C}$ ) show that only  $\text{P}_4$  and  $\text{S}_8$  are present (see Table V-5, column 4). Data taken at  $25^\circ\text{C}$  after the sample had been heated above  $200^\circ\text{C}$  (see Table V-5, column 5) are considerably different from those for the unheated sample, and indicate the formation of  $\text{P}_4\text{S}_{10}$ ,  $\text{P}_4\text{S}_3$ , and possibly other phosphorus-sulfur compounds. Because of the large excess of phosphorus,  $\text{P}_4$  molecules are still evident in the heat-treated sample, but  $\text{S}_8$  molecules are not.

The Raman studies of divalent metal ions in molten halide media have continued with an investigation of the  $\text{MgI}_2$ -KI system. Raman spectra of molten samples containing 40 and 50 mol %  $\text{MgI}_2$  in KI were identical; the spectrum of the 40 mol %  $\text{MgI}_2$  sample is shown in Fig. V-14. The band at  $109\text{ cm}^{-1}$  is almost totally polarized, whereas the bands at 58 and  $39\text{ cm}^{-1}$  are depolarized, as indicated by trace b in the figure. These results and those previously reported in ANL-7550, p. 79 for the  $\text{MgCl}_2$ -KCl and  $\text{MgBr}_2$ -KBr systems are very much the same. In each system, two bands were observed: a strong polarized band and a broad depolarized band, which was less intense and occurred at a lower frequency. In the  $\text{MgI}_2$ -KI system, the lower-frequency band was resolved into two components. Although this band was not resolved in the  $\text{MgCl}_2$ -KCl and  $\text{MgBr}_2$ -KBr systems, it very probably contained two components in these systems as well. The Raman spectra for the magnesium halide systems are most consistent with the formation of tetrahedral  $\text{MgX}_4^{-2}$  ( $\text{X} = \text{Cl}, \text{Br}, \text{or I}$ ).

### C. STUDIES OF ENERGY CONVERSION

Exploratory studies of laboratory-scale secondary cells have been directed toward obtaining a better understanding of the electrochemical processes occurring in the cells. New and potentially useful cathode materials containing phosphorus and sulfur have been introduced, and the nature of the diffusion mechanism in these cathodes has been examined. The influence of the salt-to-filler ratios in paste electrolytes on cell performance has been investigated. Several promising low-melting, mixed-cation electrolytes have evolved. In all of these studies, inert

containment materials are needed to ensure that electrochemical measurements are thermodynamically meaningful; this need is being met by the materials research program.

## 1. Lithium/Chalcogen Cells

### a. Lithium/Selenium Cells

**Cells with Liquid Electrolytes.** An attractive feature of the lithium/selenium cell is that both selenium and lithium have low melting points:  $220$  and  $180^\circ\text{C}$ , respectively. However, cell operating temperatures have been limited by the melting point,  $341^\circ\text{C}$ , of the commonly used electrolyte, the eutectic mixture composed of  $11.7\text{ mol \% LiF-29.1 mol \% LiCl-59.2 mol \% LiI}$ . In an effort to achieve lower operating temperatures, lower-melting electrolytes for lithium/selenium cells have been sought.

For successful cell operation, the electrolyte should have high lithium-ion content and mobility as well as a low melting point. At present, the adequacy of the lithium-ion flux can only be inferred from the results of cell operation and from the stability of other halides relative to  $\text{LiI}$ , the major component in most of the eutectics that have been used in cells. From a comparison of the standard free

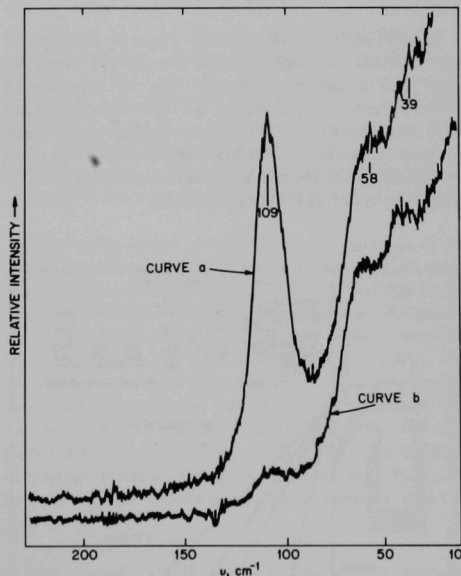


Fig. V-14. Raman Spectrum of 40 mol %  $\text{MgI}_2$ -60 mol % KI ( $360^\circ\text{C}$ ). (Incident laser beam was polarized perpendicular to direction of observation in curve a and parallel to direction of observation in curve b.)

energies of formation at 600°C for all of the alkali metal halides,<sup>37</sup> electrolytes based on the binaries LiI-KI, LiI-RbI, and LiI-CsI seem attractive. With consideration of the additional requirement that the electrolyte have a high lithium-ion content, a eutectic composed of 8.5 mol % LiCl-59 mol % LiI-32.5 mol % KI, mp = 265°C (see ANL-7550, p. 78), was prepared for use in lithium/selenium cells.

Short-time voltage-current density data for several lithium/selenium cells with LiCl-LiI-KI electrolytes are given in Fig. V-15, together with a tabulation of the cell parameters and operating conditions. The effects of adding tellurium to selenium (to improve the conductivity) and of using an expanded-mesh current collector on the performance of these cells are well illustrated by the data.

It was not possible to achieve full theoretical capacity in these cells operating at high current densities and low temperatures (below 300°C) because of formation of solid product in the cathode (see lithium-selenium phase diagram in Fig. V-4). However, it was possible to achieve 82% of theoretical capacity (1.22 A-hr) at 295°C at a current density of 0.125 A/cm<sup>2</sup> in a cell with an expanded-mesh cathode current collector; 70% of this capacity was achieved at a terminal voltage above 1 V.

Thermal analysis of the electrolyte used for all the above runs indicated its composition had not changed during the runs; thus it can be concluded that no reduction of potassium ion occurred during cell operation. It appears from these results that selected low-melting mixed-cation electrolytes can be used in lithium/selenium cells without significantly affecting cell performance relative to that of cells of the type Li/LiF-LiCl-LiI/Li in Se.

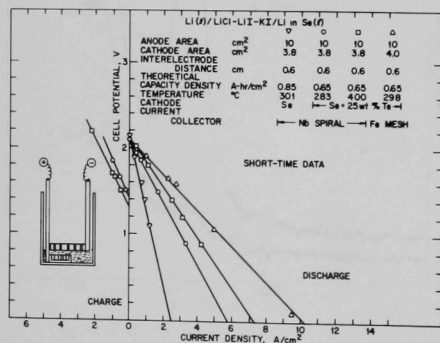


Fig. V-15. Voltage-Current Density Characteristics of a Lithium/Selenium Cell with a Mixed-Cation Liquid Electrolyte.

**Cells with Paste Electrolytes.** In the study of lithium/selenium cells with paste electrolytes, cell performance has been evaluated as a function of (1) composition of the paste electrolyte and (2) properties of the cathode current collector, including porosity, pore size, and configuration (metal felt or expanded mesh). (A further discussion of paste electrolytes is given below in Sect. V.C.2.) A diagram of the cell configuration used in these studies is shown in Fig. V-16 along with voltage-current density characteristics and the pertinent structural information for two of the cells. Discharge curves for one of the cells are given in Fig. V-17; the curves are typical of those obtained throughout the investigation. Data for the entire series of cells are summarized in Table V-6. It was generally found that at low current densities (<0.1 A/cm<sup>2</sup>), high-capacity densities were obtained with expanded-mesh current collectors, whereas at higher current densities (>0.25 A/cm<sup>2</sup>),

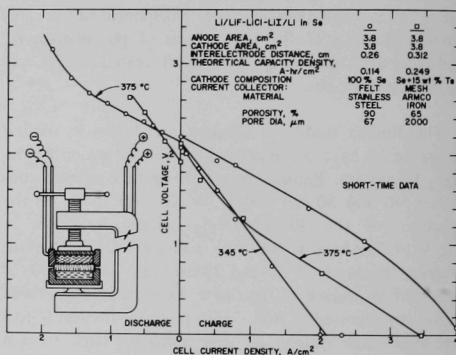


Fig. V-16. Voltage-Current Density Characteristics of Lithium/Selenium Cells with Paste Electrolytes.

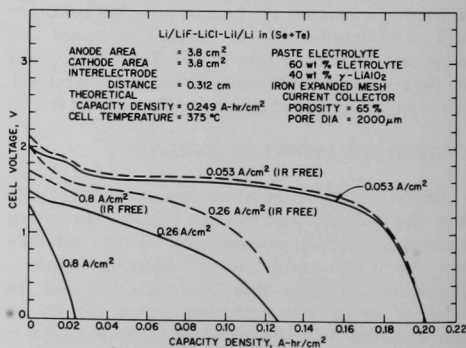


Fig. V-17. Voltage-Capacity Density Characteristics for a Lithium/Selenium Cell.

TABLE V-6. Characteristics of Some Lithium/Selenium Cells with Paste Electrolytes

Electrolyte Concentration (wt %)	Filler	Paste		Cathode Current Collector Material <sup>b</sup>	Test Duration (hr)	Max Short-circuit Current Density (A/cm <sup>2</sup> )	Maximum Power Density (W/cm <sup>2</sup> )	Maximum Capacity Density (A-hr/cm <sup>2</sup> )	Theoretical Capacity Density (A-hr/cm <sup>2</sup> )
		Thickness (cm)	Resistivity Ratio <sup>a</sup>						
50	$\gamma$ -Al <sub>2</sub> O <sub>3</sub>	0.302	11.3 <sup>c</sup>	A	5.5	1.0	0.6	0.066	0.355
	$\gamma$ -LiAlO <sub>2</sub>	0.282	8.4 <sup>c</sup>	A	24	2.1	1.1	0.070	0.585
	$\gamma$ -LiAlO <sub>2</sub>	0.300	9.5	C	6.5	1.6	0.9	0.105	0.451
	$\gamma$ -LiAlO <sub>2</sub>	0.244	10.4 <sup>c</sup>	A	24	1.3	0.7	0.237	0.494
	Y <sub>2</sub> O <sub>3</sub>	0.264	9.1	A	192	1.3	0.7	0.197	0.494
60	$\gamma$ -LiAlO <sub>2</sub>	0.259	3.5	C	25	4.1	2.7	0.073	0.371
	$\gamma$ -LiAlO <sub>2</sub>	0.274	4.7	C	3	3.4	1.9	0.105	0.114
	$\gamma$ -LiAlO <sub>2</sub>	0.312	6.3	A	24	2.3	1.2	0.206	0.249
	$\gamma$ -LiAlO <sub>2</sub>	0.305	14.7	B	192	0.79	0.45	0.040	0.460
	$\alpha$ -LiAlO <sub>2</sub>	0.285	5.4	D	5	2.63	1.4	0.033	0.123
70	$\gamma$ + $\alpha$ -LiAlO <sub>2</sub>	0.368	36 <sup>c</sup>	A	24	0.42	0.23	0.088	0.454
	$\gamma$ -LiAlO <sub>2</sub>	0.325	4.7	D	75	3.16	1.7	0.113	0.527

<sup>a</sup>Ratio of resistivity of paste to resistivity of pure electrolyte.

<sup>b</sup>A - Iron expanded mesh 1: porosity = 65%, pore size = 2000  $\mu$ m; B - Iron expanded mesh 2: porosity = 57%, pore size = 1800  $\mu$ m;

C - Stainless steel felt 1: porosity = 90%, pore size = 67  $\mu$ m; D - Stainless steel felt 2: porosity = 80%, pore size = 29  $\mu$ m.

<sup>c</sup>Poor wetting of paste by reactants.

metal-felt current collectors provided higher capacity densities. Pastes with high concentrations of electrolyte ( $\geq 70$  wt %) experienced structural failure of the paste electrolyte owing to excessive softening. Pastes with  $\leq 50$  wt % electrolyte showed generally higher resistivity ratios (paste/pure electrolyte) and poor wetting at the electrolyte-electrode interfaces.

#### b. Lithium/Sulfur Cells

A number of lithium/sulfur cells have been operated with liquid eutectic electrolytes.<sup>38,39</sup> Figure V-18 contains a diagram of the cell assembly, structural information, operating conditions, and results for three Li/LiF-LiCl-LiI/(Li in S) cells.

The performance of lithium/sulfur cells was closely related to the characteristics (porosity and pore size) of the metals used as cathode current collectors. The low-porosity

(<50%) cathode current collectors showed a low resistance overvoltage and a high diffusion overvoltage, whereas the converse was true for the high-porosity (>80%) materials. A current density of 3 A/cm<sup>2</sup> at 1 V was obtained from a cell that had sintered tungsten powder (41% porosity, 15- $\mu$ m pore diameter) as the cathode current collector; a current density of 6 A/cm<sup>2</sup> at 1 V was achieved from a cell with stainless steel felt (90% porosity, 67- $\mu$ m pore diameter) as the cathode current collector. The best performance, 7 A/cm<sup>2</sup> at 1 V, was obtained with stainless steel felt of 80% porosity and 29- $\mu$ m pore diameter. Although the cathode current collector with intermediate porosity showed the best performance of the three, it is not clear that these values of porosity and pore diameter (80% porosity, 29- $\mu$ m pore diameter) are optimum. Further improvement seems likely with additional efforts at optimization of the structure of the cathode current collector.

The voltage-current density curves for discharge of the cell having the current collector with 80% porosity show that an open-circuit voltage of 2.3 V is available and a short-circuit current density of 13 A/cm<sup>2</sup> can be obtained for a short time. The maximum power density calculated from the data in Fig. V-18 is 7.5 W/cm<sup>2</sup> (at 1.2 V). The resistance-free voltages measured by a current-interruption technique indicated that the short-time overvoltage was essentially ohmic, and originated primarily in the electrolyte and the cathode current collector. The diffusion overvoltage increases during the discharge while the resistance overvoltage remains approximately constant, as can be seen in Fig. V-19.

The overall cathode compositions at full discharge ranged from Li<sub>0.5</sub>S to LiS. Complete discharge of the cell to Li<sub>2</sub>S was not possible at current densities near 1 A/cm<sup>2</sup> because of the high diffusion overvoltage. For this reason, the highest capacity density achieved at a current density of

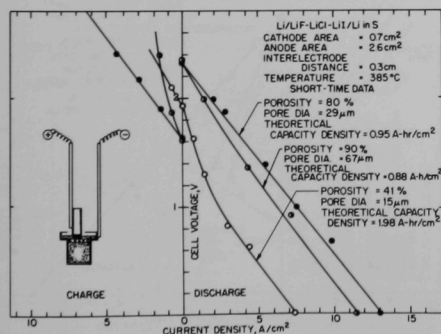


Fig. V-18. Effect of Cathode Current Collector on Cell Performance of a Lithium/Sulfur Cell.

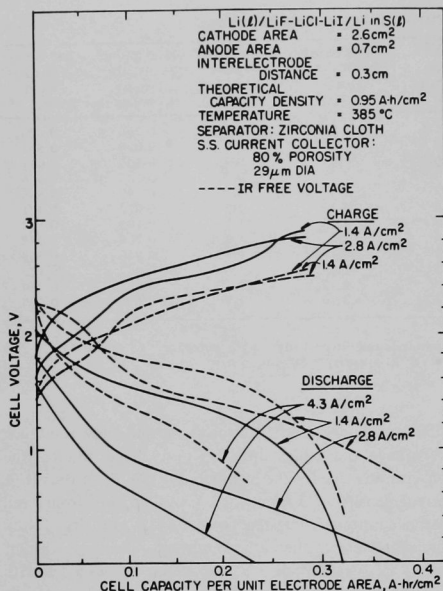


Fig. V-19. Voltage-Capacity Density Curves at Constant Current for a Lithium/Sulfur Cell.

1.4 A/cm<sup>2</sup> was 0.33 A-hr/cm<sup>2</sup> or 35% of the theoretical capacity density, based on Li<sub>2</sub>S as the final cathode composition. The open-circuit voltage was stable in a 54-hr test, thereby indicating a low rate of self-discharge.

A lithium/sulfur cell was also operated with the low-melting (184°C) LiCl-LiBr-LiI-KI-CsI eutectic as the electrolyte. The sulfur cathode of this cell contained approximately 30 wt % of a selenium-tellurium alloy to aid in current collection. Figure V-20 gives the cell design and voltage-current density characteristics for this cell at various temperatures. The performance of the cell is poor below 300°C, but seems to improve appreciably at about 330°C. The poor performance at lower temperatures is attributed to the high viscosity of the cathode alloy and to solid formation in the cathode after addition of small amounts of lithium. At higher operating temperatures, the capacity of the cell is increased by the greater solubility of lithium in the cathode alloy.

### c. Lithium/P<sub>x</sub>S<sub>y</sub> Cells

Cells with lithium anodes and compounds of phosphorus and sulfur as cathodes have been operated in an effort to improve the performance characteristics of

sulfur-containing cells.<sup>40</sup> Although lithium/sulfur cells can be operated at open-circuit voltages and short-circuit current densities comparable with those of the lithium/selenium and lithium/tellurium cells, the fraction of theoretical capacity density of the sulfur cathode that can be achieved has proven to be less than 50% of that achieved by the selenium or tellurium cathode. The low fraction of theoretical capacity density of the sulfur cathode is believed to be at least partially due to the high viscosity of liquid sulfur, which inhibits the diffusion of cell products away from the cathode-electrolyte interface. Additives such as phosphorus are known to reduce the viscosity of the sulfur considerably.<sup>41</sup>

A comparison of instantaneous voltage<sup>42</sup>-current density characteristics for a Li/P<sub>4</sub>S<sub>3</sub> cell, a Li/P<sub>4</sub>S<sub>10</sub> cell, and a Li/S cell is given in Fig. V-21, along with a diagram of

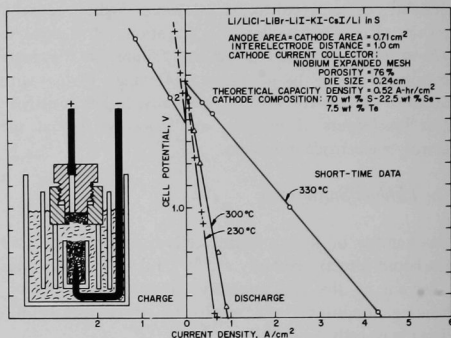


Fig. V-20. Voltage-Current Density Characteristics for a Lithium/Sulfur Cell.

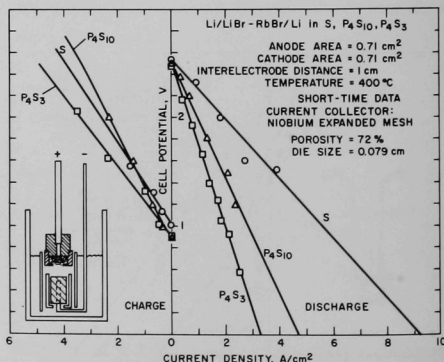


Fig. V-21. Voltage-Current Density Characteristics for Lithium/Sulfur, Lithium/P<sub>4</sub>S<sub>10</sub>, and Lithium/P<sub>4</sub>S<sub>3</sub> Cells.



the cell assembly and a summary of the operating conditions, which were the same for each cell. The sulfur cathode appears to be superior to the phosphorus-sulfur cathodes in producing a high instantaneous power density; however, a comparison of capacity density-current density data for these cathodes, shown in Fig. V-22, indicates that the phosphorus-sulfur cathodes are capable of higher capacity densities, particularly at discharge rates above  $1 \text{ A/cm}^2$ . The linear relationship between capacity density and current density on logarithmic scales is to be expected from simple diffusion theory, and the slope and position of these lines are recognized as being related to the pore size, porosity, and configuration of the cathode current collector, and to the nature of the cathode material.

Voltage-current density data for the  $\text{Li/P}_4\text{S}_{10}$  cell taken as a function of temperature indicate that the changes in internal resistance of the  $\text{Li/LiBr-RbBr/P}_4\text{S}_{10}$  cell as a function of temperature are due almost exclusively to the electrolyte. The plot of conductance against reciprocal temperature yields a straight line with a slope corresponding to an activation energy of  $3.6 \text{ kcal/mol}$ . The activation energy for ionic liquids such as fused salts is normally very close to  $3.6 \text{ kcal/mol}$ .<sup>43</sup>

The importance of diffusion in controlling cell capacity densities has prompted an investigation of the diffusion mechanism in cells with sulfur-containing cathodes. The instantaneous and long-time recovery of the terminal voltage of  $\text{Li/P}_4\text{S}_{10}$  cells was measured with a dual-beam, dual-trace oscilloscope after rapid interruption of current flow, using a method similar to that of Trachtenburg.<sup>44</sup> Figure V-23 shows the results of a typical experiment. The short-time or IR-related overvoltage was measured with the lower beam by sweeping at a rate of  $2 \mu\text{sec/cm}$ ; the long-time or diffusion-related terminal voltage recovery was measured with the upper beam by sweeping at a much lower rate of  $5 \text{ sec/cm}$ . Graphs of the steady-state terminal

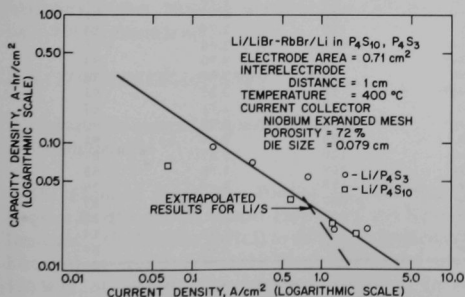


Fig. V-22. Capacity Density-Current Density Characteristics for  $\text{Li/P}_4\text{S}_3$ ,  $\text{Li/P}_4\text{S}_{10}$ , and  $\text{Li/S}$  Cells at  $400^\circ\text{C}$ .

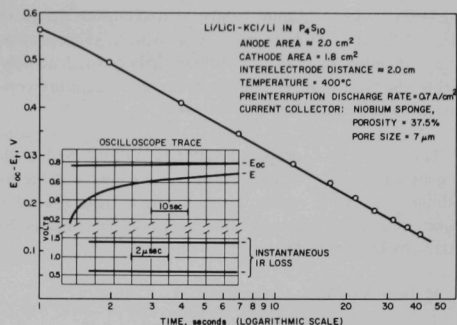


Fig. V-23. Voltage-Time Relations of a Lithium/ $\text{P}_4\text{S}_{10}$  Cell after Current Interruption.

voltage,  $E_{oc}$ , obtained after interruption, minus the time-dependent terminal voltage,  $E_t$ , plotted against time on a logarithmic scale have yielded straight lines in the time range of 1 to 100 sec after interruption of current flow (see Fig. V-23). Work currently in progress to derive mathematical expressions for this behavior has indicated that the equations governing diffusion in a semi-infinite medium adequately predict the observed region of linearity.

## 2. Immobilization of Fused-salt Electrolytes

An important factor in the development of practical cell configurations is the immobilization of one or more of the three liquid phases. A program is in progress (see ANL-7550, p. 85) to study immobilization of the electrolyte phase through the use of paste disks. The paste-electrolyte disk is a pressed composite of an inert infusible filler and the electrolyte proper, which is an ionic lithium-salt mixture. At the operating temperature of an electrochemical cell, the electrolyte is above its melting point; however, the paste, being a highly viscous material, behaves essentially as a solid. This pseudo-solid functions both as a mechanical separator between the electrodes and as an ionic conductor between them.

### a. Filler Studies

The material that has shown the most promise as a filler for paste electrolytes is meta-lithium aluminate,  $\text{LiAlO}_2$ . Both  $\alpha$ - and  $\gamma$ - $\text{LiAlO}_2$  have been studied, and methods of preparation of these materials have been devised. During the preparation studies, a previously unreported form of  $\text{LiAlO}_2$  was discovered.

In experiments to study preparation methods of other lithium aluminates, namely,  $\text{Li}_5\text{AlO}_4$  and  $\text{LiAl}_5\text{O}_8$ , a high-temperature ( $900^\circ\text{C}$ ) reaction was observed between

$\gamma$ -LiAlO<sub>2</sub> and the lithium halides that comprise the paste electrolyte. It remains to be seen whether a paste electrolyte containing  $\gamma$ -LiAlO<sub>2</sub> and lithium halides is adequately stable chemically under long-term, lower-temperature conditions of cell operation.

The stability of proposed fillers to lithium and halogens was tested. Both  $\gamma$ -LiAlO<sub>2</sub> and MgO were stable to lithium and selenium in tests of more than a week's duration at 375°C; however, Li<sub>2</sub>ZrO<sub>3</sub> was not resistant to attack by lithium under similar conditions.

#### b. Paste Studies

A necessary part of the development of cells employing paste electrolytes is the selection of pastes with suitable electrochemical and physical characteristics. Work has continued on the preparation of paste-electrolyte disks of various compositions and the determination of the properties of the disks.

Recent efforts have been directed toward producing paste electrolytes of high density. Conditions of preparation and resulting densities for several paste electrolytes are listed in Table V-7. The disks were all 2.5 cm in diameter and varied in thickness from 2 to 4 mm. The densities of

the disks that were pressed without pre-evacuation of the mold were usually lower than the densities of those obtained when the mold was evacuated prior to pressing. The effects of pressing force and pressing temperature on disk density have not yet been investigated in detail; however, it has been established that high densities can be obtained even at room temperature if enough pressing force is used. For example, 98% of theoretical density was achieved for a disk containing 50 wt %  $\gamma$ -LiAlO<sub>2</sub> by pressing at 25°C under 29,000 kg force after mold evacuation. The effect of pressing temperature (at 1450-kg pressing force) on disk density was investigated with and without evacuation using  $\gamma$ -Al<sub>2</sub>O<sub>3</sub> as the filler. At temperatures of 300 and 340°C without evacuation, the disk density approached 90% of the theoretical value. These results can be compared with a value of 85% for an identical mixture pressed at only 105°C with evacuation. Evidently, evacuation is more important to the achievement of high disk density than is elevated temperature (above 105°C).

From the above experiments, it may be concluded that, for paste-electrolyte disks of 2.5-cm diameter, densities within a few percent of the theoretical value can be obtained by vacuum molding with a force of 29,000 kg at room temperature or with a force of 1450 kg at 110°C.

TABLE V-7. Conditions of Preparation and Densities of 2.5-cm-dia Paste-electrolyte Disks

Electrolyte <sup>a</sup> Content		Filler	Source <sup>c</sup>	Pressing <sup>d</sup> Atmosphere	Pressing Temp (°C)	Density (g/cm <sup>3</sup> )	Percent of Theoretical Density
Wt %	Vol %						
50	55	$\alpha$ -LiAlO <sub>2</sub>	ANL-1	He	117	1.69	52
	49	$\gamma$ -LiAlO <sub>2</sub>	ANL-2	He	124	2.75	99
	49	$\gamma$ -LiAlO <sub>2</sub>	ANL-2	Vac	105	2.70	97
	49	$\gamma$ -LiAlO <sub>2</sub>	ESP	He	120	2.39	86
	49	$\gamma$ -LiAlO <sub>2</sub>	ESP	Vac	102	2.48	89
	49	$\gamma$ -LiAlO <sub>2</sub>	ESP	Vac <sup>e</sup>	25	2.72	98
	49	$\gamma$ -LiAlO <sub>2</sub>	G & S	He	120	2.42	87
	64	Y <sub>2</sub> O <sub>3</sub>	ROI	He	125	3.16	81
	58	$\gamma$ -Al <sub>2</sub> O <sub>3</sub>	VITRO	He	120	2.53	81
	58	$\gamma$ -Al <sub>2</sub> O <sub>3</sub>	VITRO	Vac	106	2.67	77
	66 <sup>b</sup>	$\alpha$ -LiAlO <sub>2</sub>	ANL-3	Vac	25	2.79	80
	66 <sup>b</sup>	$\alpha$ -LiAlO <sub>2</sub>	ANL-3	Vac	120	3.17	91
	65	$\alpha$ -LiAlO <sub>2</sub>	ANL-1	He	120	2.74	84
	67	$\alpha$ -LiAlO <sub>2</sub>	ANL-4	Vac	120	2.64	78
60	67	$\alpha$ -LiAlO <sub>2</sub>	ANL-4	Vac <sup>e</sup>	25	3.20	94
	67	$\alpha$ -LiAlO <sub>2</sub>	ANL-3	Vac	180	2.64	78
	67	$\alpha$ -LiAlO <sub>2</sub>	ANL-3	Vac <sup>e</sup>	25	3.22	95
	59	$\gamma$ -LiAlO <sub>2</sub>	ANL-2	He	120	2.51	85
	59	$\gamma$ -LiAlO <sub>2</sub>	ANL-2	Vac	107	2.91	99
	59	$\gamma$ -LiAlO <sub>2</sub>	ANL-5	He	120	2.66	91
	59	$\gamma$ -LiAlO <sub>2</sub>	ESP	He	120	2.57	87
	68	$\gamma$ -Al <sub>2</sub> O <sub>3</sub>	VITRO	Vac	105	2.89	85
	68	$\gamma$ -Al <sub>2</sub> O <sub>3</sub>	VITRO	He	118	2.69	79
	68	$\gamma$ -Al <sub>2</sub> O <sub>3</sub>	VITRO	He	300	2.96	87
	68	$\gamma$ -Al <sub>2</sub> O <sub>3</sub>	VITRO	He	340	>3.0	>88
	74	$\alpha$ -LiAlO <sub>2</sub>	ANL-1	He	120	2.79	74
	77	$\gamma$ -Al <sub>2</sub> O <sub>3</sub>	VITRO	He	120	2.81	84

<sup>a</sup>LiF-LiCl-LiI eutectic except where indicated.

<sup>b</sup>LiCl-LiI-KI eutectic.

<sup>c</sup>ANL = Argonne National Laboratory; ESP = Electronic Space Products; G & S = Gallard and Schlesinger;

<sup>d</sup>ROI = Research Organic/Inorganic Chemical Co.

<sup>e</sup>Pressing force 1450 kg except where indicated.

<sup>f</sup>Pressing force 29,000 kg.

### 3. Materials Stability

Some of the chemical systems of interest in the research program on liquid metals and molten salts are highly corrosive. A continuing program is being carried out to identify metals, alloys, and ceramics that resist the corrosive action of the systems being investigated so that reliable laboratory data can be obtained.

Aluminum oxide ( $\text{Al}_2\text{O}_3$ ) is a suitable electrical insulator material for use in systems with sodium and sodium-containing alloys. Other insulators are needed, however, for lithium, which is more corrosive. The results of static immersion tests of various insulators in molten lithium at  $375^\circ\text{C}$  indicate that thorium ( $\text{ThO}_2$ ), boron nitride (BN), aluminum nitride (AlN), yttria ( $\text{Y}_2\text{O}_3$ ), beryllia ( $\text{BeO}$ ), and single-crystal magnesia ( $\text{MgO}$ ) have acceptable corrosion rates, ranging from  $<1$  to 20 mils per year. Silica (Pyrex and quartz), alumina ( $\text{Al}_2\text{O}_3$ ), zirconia ( $\text{ZrO}_2$ ), and conventional magnesia ( $\text{MgO}$ ) were severely attacked.

The corrosion resistance of various materials to molten  $\text{Li-P}_4\text{S}_{10}$  mixtures at  $375^\circ\text{C}$  was measured by static immersion and corrosion agitator tests. Several materials such as molybdenum, niobium, tantalum, Durimet 20, Hastelloy B, Hastelloy C, Inconel 718, and Nicaloy demonstrated corrosion rates of less than 5 mils per year and should be useful in laboratory programs.

Molten selenium and selenium-tellurium alloys are very corrosive, especially in the presence of lithium. The Li-Te-Se system is of interest because the addition of tellurium to selenium increases the electrical conductivity of the mixture. Corrosion tests were therefore performed to determine the resistance of various materials to molten Li-Se and Li-Te-Se mixtures at  $375^\circ\text{C}$ . Of the materials tested in the Li-Se mixtures, only beryllium, niobium, niobium-1% zirconium alloy, chromium, and tungsten possess sufficient corrosion resistance to be useful in laboratory studies. Niobium is resistant to Li-Te-Se mixtures, but beryllium is not.

### D. BATTERY DEVELOPMENT

#### 1. High-specific-energy Lithium/Selenium Batteries for Implantation<sup>45</sup>

The Chemical Engineering Division has undertaken a program for the Artificial Heart Program of the National Heart and Lung Institute (NHLI) to develop an implantable battery that would deliver 10 W of power and store 120 W-hr of energy. The proposed battery is to be composed of four lithium/selenium cells having paste electrolytes of  $\text{LiAlO}_2$  compacted with the eutectic salt of  $\text{LiF-LiCl-LiI}$ . The program has the following objectives:

1) To carry out design, fabrication, and electrical performance evaluations of the pertinent characteristics of cells 7.5 cm in diameter.

2) To develop sealing and insulating materials that are stable during long-term battery operation under implantable conditions.

3) To design, fabricate, and test three first-generation batteries of implantable-sized and sealed configuration *in vitro* at  $37^\circ\text{C}$ .

#### a. Design of Sealed Cells and Batteries

The basic designs proposed for the implantable lithium/selenium cell and battery are shown in Fig. V-24. The characteristics of the battery are listed in Table V-8. This battery design, designated Mark I, is expected to deliver about 110 W-hr/kg. The battery consists of four single cells, which are stacked physically and electrically in series in a bipolar design. The cathode current collector and cathode cup are niobium; the ring insulators are boron nitride.

The Mark I design has been modified to incorporate a boron nitride ring in the periphery of the paste electrolyte. The modified design, Mark II, is expected to have a larger specific energy: 210 W-hr/kg with a niobium current collector and cathode housing, or 295 W-hr/kg with a beryllium current collector and cathode housing.

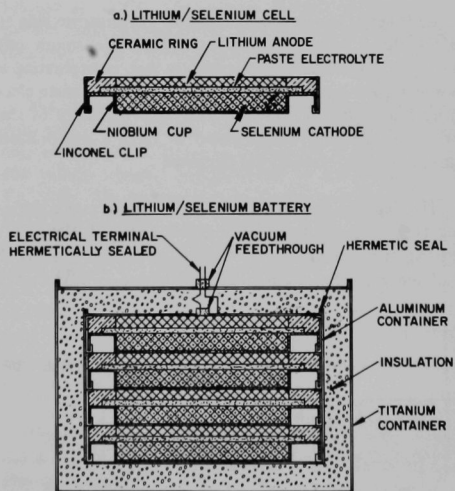


Fig. V-24. Proposed NHLI Lithium/Selenium Battery (Mark I Design).

TABLE V-8. Characteristics of Proposed NHLI Lithium/Selenium Battery (Mark I Design)

Diameter of paste electrolyte:	8.3 cm
Active electrode area per cell:	38.7 cm <sup>2</sup>
Thickness of paste electrolyte:	0.2 cm
Thickness of selenium (without current collector):	0.3 cm
Total cathode thickness:	0.65 cm
Thickness of lithium and anode current collector:	0.35 cm
Diameter of cell:	9.4 cm
Thickness of cell:	1.36 cm
Number of cells:	4
Overall diameter of battery (with 1-cm-thick insulation):	11.5 cm
Height of battery (with insulation):	7.5 cm
Volume of battery (with insulation):	781 cm <sup>3</sup>
Weight of battery:	1.09 kg
Specific energy of battery:	110 W-hr/kg
Operating temperature:	375°C
Open-circuit voltage (average):	2.0 V/cell, 8.0 V total
Operating voltage (average):	1.9 V/cell, 7.6 V total
Operating current:	1.32 A
Operating current density:	0.034 A/cm <sup>2</sup>
Short-circuit current density:	2.0 A/cm <sup>2</sup>

An alternative to using a ceramic ring as an insulator and seal in a lithium/selenium cell is to use a composite material consisting of a high-temperature-resistant polymer mixed with an inert filler such as  $\text{LiAlO}_2$  which can be cast in place. A cell design incorporating this concept is shown in Fig. V-25. Since the inner anode cup is electrically isolated from the outer cup by the insulation, the cell can be hermetically sealed by potting, brazing, or welding.

#### b. Studies of Lithium/Selenium Single Cells

**Cells with Ceramic Ring Insulators.** Performance data at 375°C have been obtained for a lithium/selenium cell having a 2.5-cm-dia paste-electrolyte disk incorporating a boron nitride insulator. Figure V-26 shows the paste electrolyte disk used in this cell. The inner periphery of the boron nitride ring was threaded to form a well-bonded surface between the ring and the paste.

The cell assembly consists of (1) an anode cup containing type 302 stainless steel Feltmetal (Huyck Metal Co.) wetted with lithium, (2) a cathode cup containing layers of niobium expanded mesh (0.23-cm die size, 57% porosity)

wetted with selenium, and (3) a paste-electrolyte disk having a composition of 60 wt %  $\text{LiF}$ - $\text{LiCl}$ - $\text{LiI}$  eutectic and 40 wt %  $\text{LiAlO}_2$  filler.

The performance of the cell at 375°C is summarized in Table V-9. During the 26-hr experiment, the cell was charged and discharged 15 times; current densities during charging ranged from 0.25 to 1 A/cm<sup>2</sup>. The cell resistance was high; however, no short circuits were observed, thus indicating that the boron nitride ring was successful in preventing the deposition of lithium in the gasket area.

**Studies of Sealing Methods.** As discussed above, boron nitride has proved to be a suitable material for sealing the anode compartment-paste interface in a lithium/chalcogen paste electrolyte cell so that lithium would not be deposited in the gasketing area of the anode compartment during the charging operation. In preliminary studies, the gasketing area of the anode compartment had been flame-sprayed with either  $\text{Y}_2\text{O}_3$ ,  $\text{Al}_2\text{O}_3$ , or  $\gamma\text{-LiAlO}_2$ ,<sup>4,6</sup> all three left a coarse, grainy surface which was not suitable for good sealing. These cells failed through a combination of separation, cracking, and corrosion of the sprayed materials. Although the boron nitride ring seal worked adequately, investigations are also being made of the sealing properties of some polymeric materials, including polyimides, with the aim of reducing the cell weight and simplifying fabrication.

A polyimide, Pyre ML (manufactured by E. I. duPont), and a silicone resin, DC 63-502 (manufactured by Dow Corning), have been examined as possible binders with  $\text{LiAlO}_2$  filler to form composite materials which possess both sealing and insulating properties. The initial results indicate that structurally sound and adherent composites can be produced with both types of resins.

A composite of  $\text{LiAlO}_2$  and Pyre ML was tested as an insulator in an anode cup of the design shown in Fig. V-25. The cup was thermally cycled from room temperature to 370°C under helium atmosphere; no cracking or separation

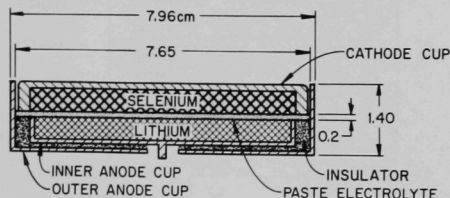


Fig. V-25. Test Cell Utilizing a Laminated Anode Cup.

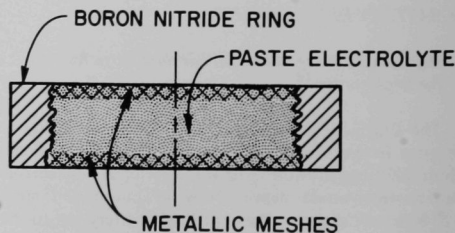


Fig. V-26. Modified Paste-electrolyte Disk and Insulator (2.5-cm diameter)

TABLE V-9. Summary of Performance Data for Lithium/Selenium Cell with Boron Nitride Ring/Paste-electrolyte Disk

Open-circuit Voltage (V)	Short-circuit Current Density (A/cm <sup>2</sup> )	Diffusion Overvoltage <sup>a</sup> (V)	Resistance Overvoltage <sup>a</sup> (V)	Resistivity Ratio <sup>b</sup>
2.11	1.6	0.39	1.16	11.1

<sup>a</sup>At 0.26 A/cm<sup>2</sup> after 0.022 A-hr/cm<sup>2</sup> discharge. Diffusion overvoltage = open-circuit voltage - IR-free voltage. Resistance overvoltage = IR-free voltage - terminal voltage.

<sup>b</sup>Resistivity of the paste disk divided by the resistivity of the pure fused-salt electrolyte.

of the composite from the walls of the cup occurred. Because the composite used in this cell design will be in contact with a paste electrolyte containing the molten LiF-LiCl-LiI eutectic, the corrosion resistance of the LiAlO<sub>2</sub> and Pyre ML composite towards the molten salt was also tested. After an exposure of 24 hr at 370°C under helium, attack on this composite was moderate and probably at an acceptable level.

DC 63-502, both as the pure resin and as a composite with LiAlO<sub>2</sub>, was applied to two metal disks which were then joined and cured. Good bonding was achieved, but gastight seals were not obtained. In a corrosion test, a composite of DC 63-502 and LiAlO<sub>2</sub> was severely attacked by the molten LiF-LiCl-LiI eutectic after 24-hr exposure at 375°C under helium.

On the basis of work performed so far, the composite of Pyre ML and LiAlO<sub>2</sub> seems promising for use as a seal and insulator for the test cell.

## 2. High-specific-power Lithium/Selenium Cells for Vehicle Propulsion<sup>4,7</sup>

The secondary lithium/selenium batteries being developed at Argonne National Laboratory have projected capabilities appropriate for hybrid electrically driven military vehicles. In particular, the projected specific power for these batteries meets the performance requirements for acceleration and hill-climbing. The lithium/selenium batteries, which will operate at temperatures of 375°C or lower, will be composed of cells with liquid lithium anodes, immobilized fused-salt electrolytes (in the form of a rigid paste), and liquid selenium cathodes. Typical peak power densities are 1 to 3 W/cm<sup>2</sup>, which correspond to an estimated 440 W/kg for optimized multikilowatt batteries. Earlier work<sup>4,8</sup> on small (3.8 cm<sup>2</sup>) laboratory-scale lithium/selenium cells resulted in the development of a cell having a peak power density of 2.7 W/cm<sup>2</sup>, a cell life of at least 200 hr, and a cycle life of more than 50 charge-discharge cycles. The objective of the present program is to develop large, scaled-up cells (30-100 cm<sup>2</sup>) having the same power density capabilities as small cells and having long lives (1000-2000 hr and 1000-2000 charge-discharge cycles).

### a. Studies of Single Cells

The studies of single cells are primarily concerned with scaling up small (2.5-cm diameter) laboratory lithium/selenium cells with paste electrolytes to 7.5-cm-dia cells that retain high electrical performance. Specific responsibilities include (1) optimizing current collection at the selenium electrode to obtain high power density for the largest possible fraction of the theoretical cell capacity, (2) evaluating various cell designs with respect to minimizing cell resistance, and (3) providing adequate sealing of selenium in the cathode compartment.

An assembled paste electrolyte cell of 7.5-cm diameter, which was used for electrical performance measurements, is shown in Fig. V-27. In the cell, a boron nitride ring insulates the anode from the cathode compartment and also serves at the anode housing. The anode consists of stainless steel Feltmetal (type 302 SS, 1.6 mm thick, 90% porosity; or type 430 SS, 6.4 mm thick, 87% porosity) soaked with lithium at 550°C. The cathode consists of niobium expanded mesh (welded to the cathode cup) of 63% porosity (0.23-cm dia size) containing selenium.

The measurements of electrical performance were made with seven test cells. The voltage-current characteristics of two of the cells (Cells 5 and 7) are given in Fig. V-27, and the voltage-capacity characteristics of the same cells in Fig. V-28. The maximum capacity obtained was 11.4 A-hr (0.36 A-hr/cm<sup>2</sup>) for Cell 7 (see Fig. V-28). This capacity, which corresponds to 58.8% of the theoretical capacity, based upon Li<sub>2</sub>Se as the fully discharged cathode composition, was measured at 400°C, 4.8-A discharge current (0.15 A/cm<sup>2</sup>) for 2.4 hr, and an average cell voltage of 1.6 V. During short-time voltage-current measurements for this cell, a short-circuit current density of 1.1 A/cm<sup>2</sup> (34.8 A) was obtained (see Fig. V-27).

The maximum short-circuit current density obtained was 3.8 A/cm<sup>2</sup> (120 A) for Cell 5 (see Fig. V-27). This cell was also discharged at constant current densities of 0.31 A/cm<sup>2</sup> (9.7 A) and 0.49 A/cm<sup>2</sup> (15.6 A); the average cell voltages during these discharges were 1.75 and 1.54 V, respectively (see Fig. V-28).

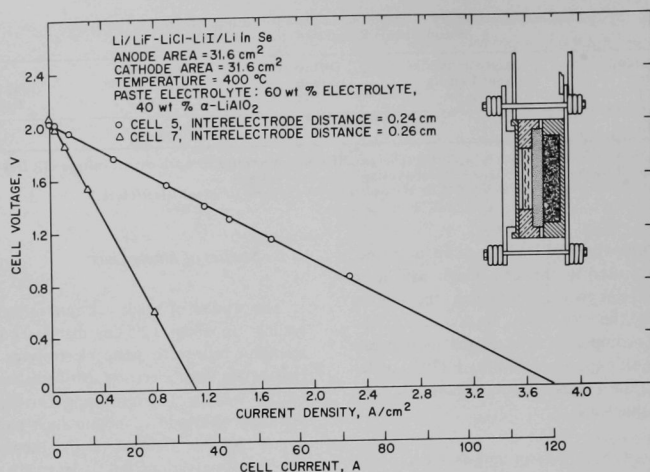


Fig. V-27. Voltage-Current Characteristics for Lithium/Selenium Cell.

#### b. Studies of Paste Electrolytes for Lithium/Selenium Cells

An important area of investigation of lithium/selenium cells is the development of large-area (30 to 100 cm<sup>2</sup>) paste electrolytes of maximum strength, minimum weight, and minimum electrolytic resistivity to serve as separators between the lithium anode and selenium cathode. The strength of the paste electrolyte is increased by increasing the ceramic filler content, whereas the resistivity is decreased by increasing the fused-salt content. The objective, therefore, is to prepare a paste electrolyte with the maximum fused-salt content consistent with good strength.

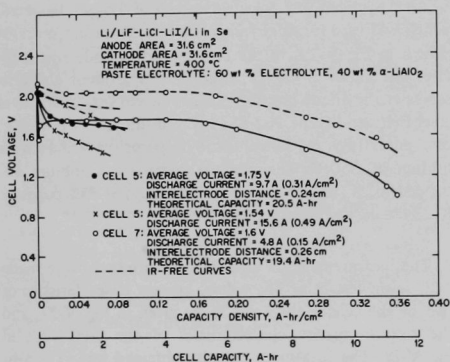


Fig. V-28. Voltage-Capacity Curves for Lithium/Selenium Cell.

The problem areas encountered during these initial performance tests were (1) the need to enhance wetting of the paste electrolyte by lithium in the anode (lack of wetting in some cells has resulted in high internal resistance and correspondingly poor electrical performance) and (2) the need to identify major factors contributing to good electrical performance of the cells so that reproducible, optimum performance can be maintained for long periods of time. A major effort in the experimental program is directed toward varying cell parameters with the aim of isolating the factors that contribute to optimum capacity density and provide high-power-density capabilities.

**Physicochemical Properties of Paste Electrolytes.** Studies aimed at developing paste-electrolyte disks possessing an optimum combination of conductivity, strength, and wettability by molten lithium have begun. The initial experiments involved (1) pressing paste disks (of 13-mm diameter and thickness of 2-3 mm) from mixtures of LiF-LiCl-LiI eutectic and lithium aluminate, and (2) investigating their resistances and wettability by molten lithium.

Since good wetting of the paste electrolyte by lithium is essential for valid resistance measurements, wetting experiments were conducted first. Wettability of the paste disks by molten lithium has been assessed by visual observation of the adherence of the lithium to paste surfaces. Paste surfaces exposed to molten lithium at 400 to 500°C became darkened and showed small areas of adhering lithium that increased in size with exposure time. Paste



surfaces became pitted at these temperatures, possibly as a result of dissolution of salt in molten lithium. Additional wetting experiments showed that paste disks could be completely covered with an adherent coating of lithium by first exposing the disks to lithium vapor ( $\sim 10^{-2}$  mm) at  $530^{\circ}\text{C}$  for about 16 hr, and then contacting them with molten lithium (previously saturated with LiF-LiCl-LiI eutectic) at  $350$  to  $360^{\circ}\text{C}$ . Further tests are needed to determine whether these are optimum conditions for wetting the paste electrolyte.

Resistances of the paste disks are currently being tested by dc measurements of the voltage across the disk and the current through the disk.

**Fabrication of Larger-diameter Paste-electrolyte Disks.** Scaling-up the 2.5-cm-dia lithium/chalcogen secondary cells requires the development of techniques for preparing paste electrolyte of 7.5-cm and larger diameters. Consequently, 7.5-cm-dia paste-electrolyte disks are being prepared under various pressing conditions to determine the effect of pressing force, temperature, and specific surface area of the ceramic filler material on the disk density (densities of approximately 99% of the theoretical value are desirable). In recent tests, the LiF-LiCl-LiI eutectic (usually  $\sim 60$  wt %) was mixed with the filler ( $\alpha$ - or  $\gamma$ - $\text{LiAlO}_2$ ) under an inert atmosphere, the mixture was pressed under vacuum at temperatures from  $25$  to  $275^{\circ}\text{C}$  using a press of  $5.9 \times 10^4$ -kg capacity, and the density of the disk was then measured.

The paste electrolytes prepared under these conditions had densities that ranged from 77 to 99% of the theoretical values. Although the optimum pressing conditions have not yet been determined, these data show that high-density paste electrolytes can be prepared from both  $\alpha$ - $\text{LiAlO}_2$  and  $\gamma$ - $\text{LiAlO}_2$ . Hot pressing under vacuum appears to be necessary for high density in the present pressing apparatus.

#### c. Sealants and Insulators

Lithium/selenium batteries will require electrically insulating materials resistant to lithium, selenium, and lithium-selenium alloys. A sealant that is resistant to these same materials may be required to produce a hermetically sealed battery.

The electrical insulators being tested are primarily the more stable oxides and nitrides, such as  $\text{MgO}$ ,  $\text{Y}_2\text{O}_3$ ,  $\text{ThO}_2$ , and  $\text{AlN}$ . Preliminary tests show corrosion rates of 26 mils/yr for single-crystal  $\text{MgO}$  and 71 mils/yr for  $\text{Y}_2\text{O}_3$ .

Insulating polymers are also being tested for thermal stability and for resistance to lithium, selenium, and electrolytes, since they offer the potential of providing

both electrical insulation and hermetic sealing in a thin, light-weight form. Screening tests indicate that polyimides and polycarbonesiloxanes possess adequate thermal stability but inadequate corrosion resistance to cell components. More extensive testing under simulated cell environments is necessary.

#### d. Corrosion by Lithium-Selenium Mixtures

The development of reliable, long-lived lithium/selenium secondary batteries requires corrosion-resistant materials of construction. Selenium, lithium, and the molten salts utilized in these cells are relatively reactive and, consequently, are corrosive to many common materials. The selection of suitable corrosion-resistant materials is a major requirement for the successful development of these batteries.

Current program emphasis is on corrosion resistance to the lithium-selenium alloys. Corrosion by lithium is not being extensively investigated because lithium can probably be contained in austenitic stainless steels or similar conventional materials. These steels have performed well in laboratory tests for several hundred hours.

The corrosion resistance of a variety of materials to 20 at. % lithium-selenium mixtures at  $375^{\circ}\text{C}$  were measured in  $\sim 300$ -hr static immersion tests. The results of these tests, which are shown graphically in Fig. V-29, indicate that niobium and niobium-1% zirconium alloys are the most resistant materials tested. Chromium and two cobalt-base alloys (Haynes 25 and Unitemp 605) also seem to be usable, although their corrosion resistance needs to be

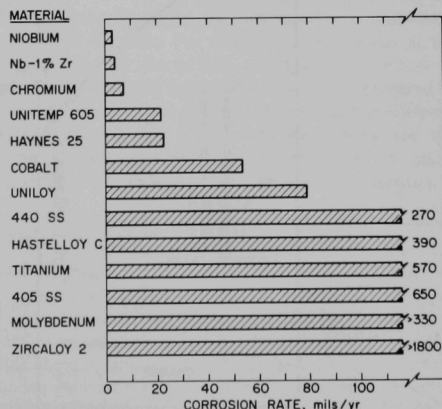


Fig. V-29. Corrosion of Test Materials by 20 at. % Lithium-Selenium Mixtures (static immersion tests; temperature,  $375^{\circ}\text{C}$ ; test duration, 200-350 hr).

better established through longer-term tests. The other materials tested are not sufficiently corrosion resistant for use under cell conditions.

### 3. Lithium/Sulfur Cells for Vehicle Propulsion<sup>49</sup>

Battery-powered urban automobiles should significantly reduce the amount of air pollution caused by combustion-engine exhaust gases. However, presently available batteries do not have sufficient energy-storage capacity per unit weight, and consequently are heavy, bulky, and too costly for consumer acceptance. The ultimate objective of the present program is to provide the technology necessary for the construction of a multikilowatt secondary battery able to power a technically attractive electric passenger vehicle. This battery must be able to store 200 W-hr/kg and deliver power at a peak rate of 200 W/kg. The immediate objectives are to investigate the performance characteristics of promising lithium/chalcogen cells, to provide a cell structure compatible with vehicle applications, and to identify suitable materials of construction.

#### a. Investigation of Small-scale Lithium/Sulfur Cells

A study of lithium/sulfur cells with molten salt electrolytes is being performed to determine if these cells offer sufficient potential for development of a vehicular propulsion system. An experimental vertical lithium/sulfur cell has

been operated at temperatures from 340 to 380°C under a helium atmosphere. The electrolyte was the molten LiF-LiCl-LiI eutectic (mp, 341°C). Both the cathode and anode compartments were made of type 304 stainless steel, and had a geometrical electrode area of 3.8 cm<sup>2</sup> and a depth of 1.25 cm. Disks of stainless steel Feltmetal (90% porosity), soaked with either sulfur or lithium, were placed in the appropriate electrolyte holders; average amounts of reactants held in the Feltmetal disks were 3.8 g sulfur and 3.6 g lithium, amounts which correspond to a capacity of about 10 A-hr. The interelectrode distance was varied, but for most experiments was 1.0 cm. The cell was discharged and charged at temperatures from 340 to 380°C; the data obtained at 350°C are shown in Fig. V-30. Although these data demonstrate good cell performance, displacement of sulfur from the cathode current collector by the electrolyte has limited the usefulness of this cell geometry.

A horizontal lithium/sulfur cell (similar to the one shown in Fig. V-18 and described in Sect. V.C.1.b of this report) was operated to investigate various configurations of the cathode current collector with the aim of finding a configuration that would reduce ohmic and diffusion overvoltages to acceptable values. Seven cathode current collectors made of stainless steel Feltmetal having various porosities and pore sizes were evaluated in Li/LiF-LiCl-LiI/S cells at 375°C. The physical characteristics and capabilities of the cells are listed in Table V-10.

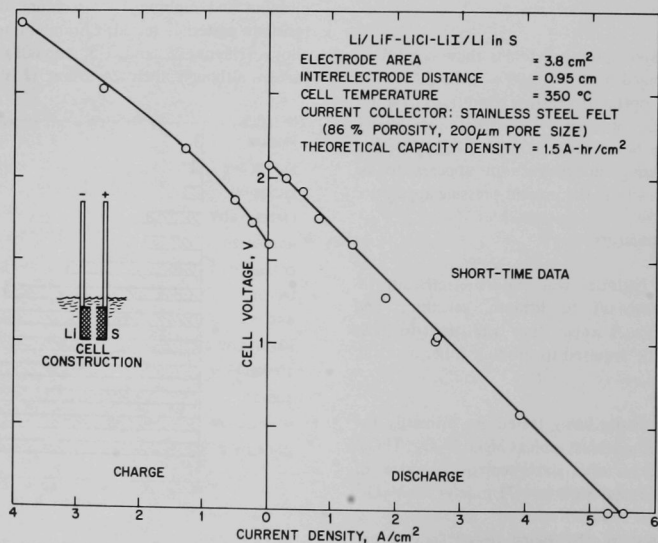


Fig. V-30. Voltage-Current Characteristics of a Lithium/Sulfur Cell.

TABLE V-10. Characteristics of Cathode Structures and Cell Performance

				Cell System	Li/LiF-LiCl-Li/S		
				Anode Area	2.6 cm <sup>2</sup>		
				Cathode Area	0.7 cm <sup>2</sup>		
				Inter-electrode Distance	0.3 cm		
				Typical Cell Temperature	375°C		
Material	Cathode		Theoretical Capacity <sup>a</sup> (A-hr)	Capacity (A-hr)	Overvoltages <sup>b</sup>		
	Porosity (%)	Pore Size (μm)			η <sub>r</sub> (V)	η <sub>d</sub> (V)	η (V)
430 SS	80	240	0.910	0.12	0.48	0.50	0.98
430 SS	60	100	0.657	0.067	0.75	0.60	1.35
302 SS	40	19	0.437	0.030	1.0	0.90	1.9
302 SS	70	19	0.767	0.067	0.46	0.45	0.91
302 SS	60	19	0.657	0.042	0.75	0.80	1.55
302 SS	80	29	0.910	0.18	0.38	0.40	0.78
430 SS	80	240	0.910	0.14	0.48	0.65	1.13

<sup>a</sup>Based on the conversion of total sulfur charge into Li<sub>2</sub>S. No consideration was made for evaporation losses.

<sup>b</sup>These overvoltages were calculated from IR-free voltages of the cells running at 1.4-A/cm<sup>2</sup> discharge after 0.047-A-hr/cm<sup>2</sup> operation. η<sub>r</sub> = resistance overvoltage = IR-free voltage - terminal voltage. η<sub>d</sub> = diffusion overvoltage = open circuit voltage - IR-free voltage. η = total overvoltage = η<sub>r</sub> + η<sub>d</sub>.

The results of this series of performance tests show that capacity densities as high as 0.26 A-hr/cm<sup>2</sup> are obtainable. When the cells are operated under similar charge and discharge conditions, the capacity density is related to the porosity of the cathode current collector, higher porosities yielding higher capacity densities.

Design calculations based on these data have been performed to assess laboratory-cell performance in terms of the requirements for electric vehicle propulsion. These calculations indicate that present laboratory-cell performance is probably adequate for urban electric vehicles, but that it should be increased if high-performance electric vehicles are contemplated.

#### b. Fillers for Paste Electrolytes

Possible fillers for paste electrolytes in lithium/sulfur cells were tested by observing their reactivity with sulfur at 375°C. Under test conditions, MgAl<sub>2</sub>O<sub>4</sub> and MgO suffered no degradation. Except for a trace of Li<sub>2</sub>S found in one experiment, no sign of attack on γ-LiAlO<sub>2</sub> was observed. The compounds ThO<sub>2</sub>, CaO, AlN, and LiYO<sub>2</sub> reacted with sulfur and are, therefore, unsatisfactory as fillers in pastes for use in lithium/sulfur cells.

#### c. Corrosion by Sulfur-containing Mixtures

The corrosion resistance of various materials to conditions that would be encountered in the anode and cathode compartments of lithium/sulfur cells is being determined to identify suitable materials of construction. Two classes of materials resistant to lithium-sulfur mixtures at temperatures near 375°C are needed. Firstly, a corrosion-resistant material possessing good electrical conductivity is required to serve as the cathode current collector and probably as the cathode housing. Secondly, a corrosion-resistant

material that is electrically insulating is required to prevent short-circuit contact between the anode and cathode housings. Of the electrically conductive materials tested, molybdenum, chromium, Zircaloy-2, and Inconel 702 were the most corrosion resistant, all with corrosion rates less than 3 mils/yr. Of the electrically insulating materials tested, boron nitride and yttria appear to be the most resistant and will be used in initial cell tests. Single-crystal magnesia is not resistant to lithium-sulfur mixtures.

#### 4. Performance Comparison

To understand the capabilities of the various cells studied, including those previously reported (see ANL-7550, p. 84), the performance data must be placed in perspective.<sup>4,8,50</sup> A comparison of the voltage-current density characteristics for the cells with liquid electrolytes is shown in Fig. V-31. For purposes of the comparison, the original data for the Li/P<sub>4</sub>S<sub>10</sub> and Li/P<sub>4</sub>S<sub>3</sub> cells were adjusted (as indicated by the dashed lines) to correspond to a smaller interelectrode distance. The average interelectrode distance for the cells of Fig. V-31 was 0.4 cm, and the active electrode area varied from 0.7 to 10 cm<sup>2</sup>. A similar comparison of voltage-current density characteristics is

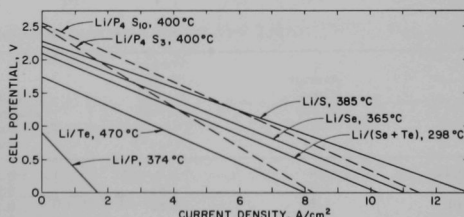


Fig. V-31. Comparison of the Voltage-Current Density Characteristics of Cells with Liquid Electrolytes.

shown in Fig. V-32 for cells with paste electrolytes. Data are given for a scaled-up, 7.5-cm-dia lithium/selenium cell as well as for 2.5-cm-dia cells. Table V-11 lists the best capacity densities obtained for both the liquid- and paste-electrolyte cells; the best cell performance is achieved in cells having high capacity densities at high current densities. No data are given in Table V-11 for the lithium/phosphorus cell, which has not performed well enough to be of further interest.

The performance data shown in Fig. V-32 and Table V-11 were used, together with a battery design

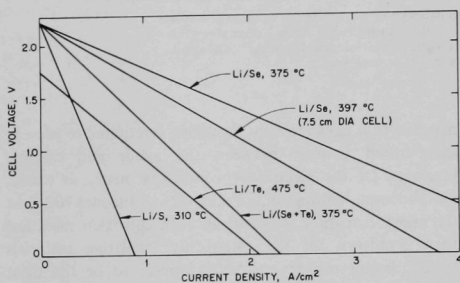


Fig. V-32. Comparison of the Voltage-Current Density Characteristics for Cells with Paste Electrolytes (all cells 2.5 cm in diameter except as indicated).

TABLE V-11. Summary of Capacity Densities Achieved for Lithium/Chalcogen Cells

Cell	Type Electrolyte <sup>a</sup>	Temp (°C)	Capacity Density (A-hr/cm <sup>2</sup> )
Li/LiF-LiCl-Li/Te	L	470	0.125 at 2 A/cm <sup>2</sup>
	P (2.5)	475	
Li/LiF-LiCl-Li/Se	L	365	0.52 at 2 A/cm <sup>2</sup>
	P (2.5)	375	0.202 at 0.26 A/cm <sup>2</sup>
	P (7.5)	397	0.32 at 0.5 A/cm <sup>2</sup>
Li/LiCl-LiI-KI/Se + Te	L	298	0.52 at 0.13 A/cm <sup>2</sup>
Li/LiF-LiCl-LiI/Se + Te	P (2.5)	375	0.274 at 0.26 A/cm <sup>2</sup>
Li/LiF-LiCl-LiI/S	L	385	0.38 at 2.8 A/cm <sup>2</sup>
Li/LiBr-RbBr/P <sub>4</sub> S <sub>10</sub>	L	400	0.05 at 0.6 A/cm <sup>2</sup>
Li/LiBr-RbBr/P <sub>4</sub> S <sub>3</sub>	L	400	0.04 at 0.58 A/cm <sup>2</sup>

<sup>a</sup>L indicates liquid-electrolyte cells ranging in active electrode area from 0.7 to 10 cm<sup>2</sup>.

P (2.5) indicates a 2.5-cm-dia paste-electrolyte cell. P (7.5) indicates a 7.5-cm-dia paste-electrolyte cell.

TABLE V-12. Specific Power and Specific Energy Calculated for Lithium/Chalcogen Batteries<sup>a</sup>

	Average Open-circuit Voltage (V)	Average Short-circuit Current Density (A/cm <sup>2</sup> )	Paste-electrolyte Thickness (cm)	Cathode-cup Material	Specific Power <sup>b</sup> (W/kg)	Specific Energy <sup>c</sup> (W-hr/kg)
Li/Te	1.4	1.4	0.2	W	95	115
Li/Se	1.85	1.85	0.2	Be	254	313
Li/S	1.85	1.85	0.2	Mg (or Be)	342	437

<sup>a</sup>In all cases cathode thickness was 0.5 cm and the anode-cup material was beryllium.

<sup>b</sup>Based on a 30-min rate.

<sup>c</sup>Based on a 2-hr rate.

similar to that shown in Fig. V-24, to calculate the expected performance for fully engineered batteries with paste electrolytes. These calculated values (based on a 30-min rate for specific power and a 2-hr rate for specific energy) are shown in Table V-12 for lithium/tellurium, lithium/selenium, and lithium/sulfur batteries. The expected performance for a lithium/(selenium + tellurium) battery would be similar to that for the lithium/selenium battery; likewise, the expected performance for a lithium/P<sub>4</sub>S<sub>10</sub> battery would be almost the same as that for the lithium/sulfur battery. The calculations indicate that both specific power and specific energy increase as the equivalent weight of the cathode material decreases, i.e., the lithium/sulfur battery would show the best performance of the three. From an economic standpoint, only batteries using small amounts of the relatively costly selenium and tellurium are practical.

The advantages of the lithium/chalcogen batteries can be seen by a comparison of their expected performance characteristics (see Table V-12) with the performance characteristics of conventional batteries. On the same rate basis (a 30-min rate for specific power and a 2-hr rate for specific energy), a Cd/Ni<sub>2</sub>O<sub>3</sub> battery has a specific power of 70 W/kg and a specific energy of 35 W-hr/kg; a Pb/PbO<sub>2</sub> battery has a specific power of 50 W/kg and a specific energy of 30 W-hr/kg. In contrast, a lithium/sulfur battery, for example, is expected to produce a specific power of 342 W/kg and a specific energy of 437 W-hr/kg.

## REFERENCES AND FOOTNOTES

1. A. S. Dworkin, H. R. Bronstein, and M. A. Bredig, *J. Phys. Chem.* **66**, 572 (1962).
2. M. Okada, R. A. Guidotte, and J. V. Corbett, *Inorg. Chem.* **7**, 2118 (1968).
3. F. G. Fumi, *Phil. Mag.* **46**, 1007 (1955).
4. Atomic units are used throughout this discussion.
5. N. H. March, *Liquid Metals*, Pergamon Press, London, (1968), p. 51.
6. K. Mukherjee, *Trans. Met. Soc. AIME* **236**, 1324 (1966).
7. N. W. Ashcroft and J. Lekner, *Phys. Rev.* **145**, 83 (1966).
8. The Ostwald solubility coefficient is defined as the volume of dissolved gas per unit volume of solvent.
9. M. S. Wertheim, *Phys. Rev. Lett.* **10**, 321 (1963).
10. J. O. Hirschfelder, C. F. Curtiss, and R. Bird, *Molecular Theory of Gases and Liquids*, John Wiley and Sons, New York, Ch. 3 (1954).
11. G. T. Clayton and LeRoy Heaton, *Phys. Rev.* **121**, 649 (1961).
12. E. A. Guggenheim, *J. Chem. Phys.* **13**, 253 (1945).
13. E. A. Guggenheim, *Proc. Phys. Soc.* **85**, 811 (1965).
14. G. M. Ziesing, *Aust. J. Phys.* **6**, 86 (1953).
15. J. Bohdanský and H. E. J. Schins, *J. Inorg. Nucl. Chem.* **29**, 2173 (1967).
16. E. U. Franck and F. Hensel, *Phys. Rev.* **147**, 109 (1966).
17. J. Bender, *Ann. Phys. (Leipzig)* **16**, 246 (1915); **19**, 410 (1918).
18. A. V. Grosse, *J. Inorg. Nucl. Chem.* **22**, 23 (1961).
19. I. G. Dillon, P. A. Nelson, and B. S. Swanson, *J. Chem. Phys.* **44**, 4229 (1966).
20. A. V. Grosse, *J. Inorg. Nucl. Chem.* **22**, 23 (1961).
21. A. I. Gerbanov, *Quantum Electron Theory of Amorphous Conductors*, Consultants Bureau, New York (1965).
22. H. W. Henkels, *J. Appl. Phys.* **21**, 725 (1950).
23. H. W. Henkels and J. Maczuk, *J. Appl. Phys.* **24**, 1056 (1953).
24. B. Lizell, *J. Chem. Phys.* **20**, 672 (1952).
25. E. H. Baker, *J. Chem. Soc.* **A1968**, 1089.
26. O. Watanabe and S. Tamaki, *Electrochim. Acta* **13**, 11 (1968).
27. J. C. Perron, *Advan. Phys.* **16**, 657 (1967).
28. A. I. Blum and A. R. Regel, *Zh. Tekhn. Fiz.* **23**(6), 964 (1953); data taken from D. M. Chizhikov and V. P. Schastlivyi, *Selenium and Selenides*, Collett Publishers, London (1968), p. 362.
29. F. Feher and H. D. Lutz, *Z. Anorg. Allgem. Chem.* **333**, 216 (1964).
30. C. A. Kraus and E. W. Johnson, *J. Phys. Chem.* **32**, 1281 (1928).
31. J. Lumdsen, *Discussions Faraday Soc.* **32**, 138 (1961).
32. R. Sridhar, C. E. Johnson, and E. J. Cairns, *Phase Diagrams of the Systems LiI-KI and LiI-RbI*, *J. Chem. Eng. Data* (in press).
33. D. B. Leiser and O. J. Whittemore, Jr., *J. Amer. Ceram. Soc.* **50**, 50 (1967).
34. C. H. Liu and L. R. Lieto, *J. Chem. Eng. Data* **14**, 83 (1969).
35. H. Gerding, J. W. Maarsen, and P. C. Nobel, *Rev. Tran. Chem.* **76**, 757 (1957).
36. D. H. Zipp, *Proc. 4th Intern. Meet. Mol. Spectroscop., Bologna, Italy, 1959*, Vol. 1 (1962), p. 345.
37. *JANAF Thermochemical Tables*, Dow Chemical Co., Midland, Michigan (1962).
38. E. J. Cairns and H. Shimotake, *High Temperature Batteries*, *Science* **164**, 1347 (1969).

39. H. Shimotake and E. J. Cairns, *A Lithium/Sulfur Secondary Cell with a Fused-salt Electrolyte*, The Electrochemical Society New York Meeting, May 1969, Abstr. No. 206; Extended Abstracts of the Industrial Electrolytic Div., 5, 520 (1969).
40. V. A. Maroni and E. J. Cairns, *Studies of a Li/P<sub>4</sub>S<sub>10</sub> Electrochemical Cell*, Abstracts of Papers Presented at the 158th Amer. Chem. Soc. Mtg., New York, Sept. 8-12, 1969: PHYS-113.
41. J. R. Van Wazer, *Phosphorus and Its Compounds*, Vol. I, Chemistry, Interscience Publishers, Inc., New York (1958), p. 300.
42. The instantaneous voltage is the cell terminal voltage a fraction of a second after initiation of current flow.
43. G. Kortum and J. O'M. Bockris, *Textbook of Electrochemistry*, Vol. I, Elsevier Publishing Co., Amsterdam (1951), p. 203.
44. I. Trachtenburg, J. Electrochem. Soc. *111*(1), 110 (1964).
45. This work is sponsored by the Artificial Heart Program, National Heart and Lung Institute.
46. Experiments conducted under AEC-sponsored work.
47. This work is sponsored by the U.S. Army Mobility Equipment Research and Development Center, Fort Belvoir, Virginia.
48. H. Shimotake, A. K. Fischer, and E. J. Cairns, "Secondary Cells with Lithium Anodes and Paste Electrolytes," in *Proc. 4th Intersociety Energy Conversion Engineering Conference*, American Institute of Chemical Engineers, New York (1969), p. 538.
49. This work is sponsored by the National Air Pollution Control Administration of CPE, Public Health Service, U.S. Department of Health, Education, and Welfare.
50. E. J. Cairns, H. Shimotake, and A. K. Fischer, *Lithium/Chalcogen Electrochemical Cells for Energy Storage*, Argonne National Laboratory Reviews 5(2), 87 (1969).



## VI. FLUIDIZED-BED COMBUSTION OF FOSSILE FUELS

The fluidized-bed technique is being investigated as a possible way to reduce the emission of atmospheric pollutants in the combustion of coal.<sup>1</sup> The concept involves the introduction of fuel and an SO<sub>2</sub>-reactive additive (such as limestone) into a hot fluidized bed of solids. The solids consist of small particles of noncombustible material, such as ash, held in a dense suspension by a stream of air passing upward through them. The fuel burns as it mixes with the bed material. The heat generated is transferred to boiler tubes immersed in the fluidized bed, and simultaneously SO<sub>2</sub> reacts *in situ* with the additive material. The efficient gas-solids contacting in a fluidized bed may greatly decrease SO<sub>2</sub> emission.

A 6-in.-dia, bench-scale fluidized-bed combustor (see Fig. VI-1) has been constructed, together with a preheater, three feeders, and two cyclones (see ANL-7550, Fig. VI-1, p. 98). Initially, exploratory bench-scale experiments were performed to aid in the selection of operating conditions. Next, a systematic set of bench-scale experiments were performed to investigate the emission of SO<sub>2</sub> under conditions applicable to conceptual designs of both utility-sized power-generating stations and industrial steam boilers. The variables considered were the particle size of the limestone additive, the superficial velocity of fluidizing gas,

and the recycling or nonrecycling of elutriated solids to the fluidized-bed combustor. An objective of the bench-scale experimental work is to determine the conditions necessary to achieve a high degree of SO<sub>2</sub> removal from the flue gas and a high degree of utilization of the limestone or other additive material.

The major results of the bench-scale experiments, which were all conducted at a combustion temperature of 1600°F and a superficial gas velocity of 3 ft/sec, are as follows:

- 1) The emission of SO<sub>2</sub> was reduced by 29 to 87% of the SO<sub>2</sub> concentration obtained in the absence of limestone, with the percentage decrease depending on the type, particle size, and quantity of limestone added.
- 2) The most favorable result (87% reduction in the emission of SO<sub>2</sub>) was obtained when a calcitic limestone No. 1359 of 25- $\mu$ m average particle size was added at 2.2 times the stoichiometric requirement.
- 3) For any particular type of limestone additive, greater SO<sub>2</sub> removal was generally noted for finer-particle-sized material than for that of coarse particle size.

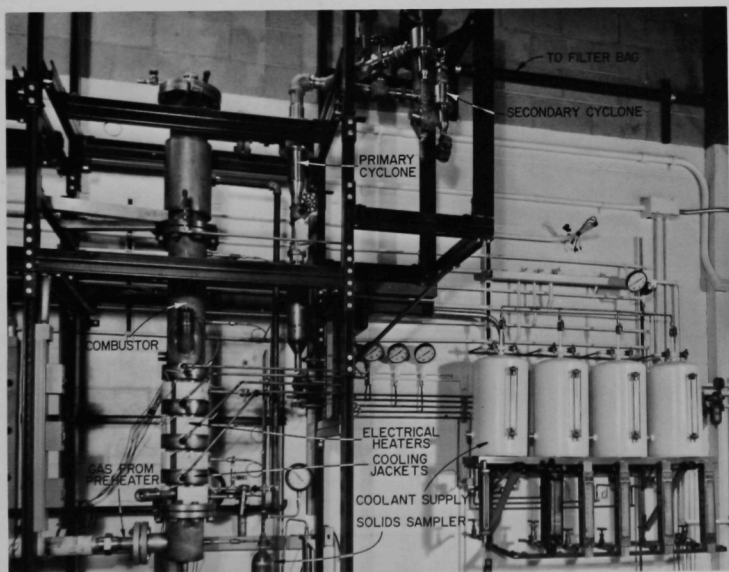


Fig. VI-1. Fluidized-bed Bench-scale Combustor and Associated Equipment.

4) From the experimental results, it appears that calcitic limestone No. 1360 is more reactive with  $\text{SO}_2$  than calcitic limestone No. 1359 or dolomitic limestone No. 1337 of the same particle size.

5) The time elapsed from the start of additive feeding to the achievement of a constant  $\text{SO}_2$  level in the flue gas ranged from less than one hour to several hours, depending on the particle size of the additive.

6) The maximum degree of utilization of CaO achieved during the experiments was 38%.

7) Partially reacted additive that accumulated in the fluidized bed contributed little to overall  $\text{SO}_2$  absorption, indicating that CaO particles absorb  $\text{SO}_2$  to a negligible extent after about 30% of the CaO is converted to  $\text{CaSO}_4$ .

8) The observed reductions in  $\text{SO}_2$  emission with limestone No. 1359 are less than predicted by the ANL empirical model (90%, discussed in ANL-7550, pp. 98-99), presumably because the kinetic data upon which the model is based reflect the reactivity of 1337 and 1360 limestones that were calcined and sulfated in laboratory equipment.

9) The combustion efficiency of a fluidized-bed system, expressed as the percentage of carbon completely burned, was determined to be 96.7 and 97.1% for two experiments. The principal loss of unburned carbon during these experiments was that associated with the solids elutriated from the fluidized bed (average carbon content, 15 wt %) and was about 3% of the carbon input associated with the coal feed. Recycle of elutriated solids would be expected to reduce the overall carbon losses from the system. The carbon monoxide and hydrocarbon concentrations in the flue gas were 75-400 ppm and 2-20 ppm, respectively, corresponding to a maximum loss of 0.26% of the input carbon. Solids withdrawn to maintain a constant bed level had a carbon concentration of only 0.01 to 0.1 wt %, and their total carbon content was 0.001 to 0.04% of the input carbon.

10) Analysis of solids elutriated during an experiment that employed a 25- $\mu\text{m}$  particle-sized additive indicated

that the fines residence time in the fluidized bed was sufficient for about 80% of the additive to be calcined to CaO before it was elutriated.

11) Solids elutriation rates determined during periods of no additive feeding indicate that virtually all of the ash associated with the coal used in these experiments was elutriated. Other solids elutriated were  $\text{CaSO}_4$ , unreacted CaO, and uncalcined  $\text{CaCO}_3$ . Comparison of elutriation rates for experiments using different additives suggests that there was less decrepitation of additive material 1359 than of 1337 or 1360.

12) The average particle size of elutriated solids was about 90  $\mu\text{m}$  during periods of no additive feeding and decreased to about 60  $\mu\text{m}$  during an experiment in which 25- $\mu\text{m}$  additive was added to the fluidized bed. The efficiencies of the two cyclones for separation of solids ranged from 86 to 90% of total solids for the primary cyclone and from 97 to 99% for the combined cyclones.

13) Bench-scale experiments conducted at 1600°F with argon substituted for nitrogen established that nitrogen compounds contained in coal are the source of  $\text{NO}_x$  compounds in the flue gas.

14) A reduction of 30-40% in nitric oxide emission in the flue gas was noted when limestone additive (No. 1359) was introduced into the fluidized-bed combustor. This reduction (concomitant with the reduction in  $\text{SO}_2$  concentration) could be due to catalysis or other enhancement of reactions to form  $\text{NO}_2$ , or decompose NO, or react NO with CaO or  $\text{CaSO}_4$ .

At the request of NAPCA, members of the ANL fluidized-bed combustion group accompanied NAPCA personnel and others to England for a review of British work on fluidized-bed combustion of fossil fuels. The results of this survey have been published.<sup>2</sup>

Future experimental work planned on the reduction of  $\text{SO}_2$  emission will investigate the effects of two variables: (1) superficial gas velocity and (2) recycle of elutriated fines to the fluidized bed.

## REFERENCES AND FOOTNOTES

1. The program at ANL is sponsored by the National Air Pollution Control Administration (NAPCA). The first annual report (in press) on this investigation is: A. A. Jonke, E. L. Carls, R. L. Jarry, M. Haas, W. A. Murphy, and C. B. Schoffstoll, *Reduction of Atmospheric Pollution by the Application of Fluidized-bed Combustion*, Annual Report, July 1968-July 1969, ANL-ES/CEN-FB1001.
2. Review of British Program on Fluidized-bed Combustion - Report of U.S. Team Visit to England, February 17-28, 1969, ANL-ES/CEN-FB1000 (in press).

## VII. ADDENDUM

### Publications--1969

#### A. OPEN LITERATURE PUBLICATIONS

R. J. Ackermann, E. G. Rauh, and M. S. Chandrasekharaiah  
*A Thermodynamic Study of the Uranium-Uranium System*  
J. Phys. Chem. 73, 762-769 (April 1969).

M. D. Adams  
*Distribution of Alpha and Gamma Emitting Nuclides in a Fast Reactor Irradiated  $UO_2$ - $PuO_2$  Fuel*  
Abstracts of Papers Presented at the 158th Amer. Chem. Soc. Mtg., New York, Sept. 8-12, 1969. NUCL-52.

L. J. Anastasia, P. G. Alfredson, and M. J. Steindler  
*Fluidized-Bed Fluorination of  $UO_2$ - $PuO_2$ -Fission Product Pellets with  $BrF_5$  and Fluorine. Part I. The Fluorination of Uranium, Neptunium and Plutonium*  
Nucl. Appl. and Technol. 7(5), 425-432 (1969).

L. J. Anastasia, P. G. Alfredson, and M. J. Steindler  
*Fluidized-Bed Fluorination of  $UO_2$ - $PuO_2$ -Fission Product Pellets with  $BrF_5$  and Fluorine. Part II. Process Considerations*  
Nucl. Appl. and Technol. 7(5), 432-442 (1969).

L. J. Anastasia and M. J. Steindler  
*Reprocessing of Simulated Fast Breeder Fuel ( $UO_2$ -20 wt %  $PuO_2$ ) Using Fluoride Volatility Methods*  
Trans. Amer. Nucl. Soc. 12(2), 446 (1969). Abstract.

E. J. Cairns and H. Shimotake  
*High Temperature Batteries*  
Science 164, 1347-1355 (June 20, 1969).

E. J. Cairns  
*Fuel Cell Electrolyte and Process of Using*  
U.S. Patent No. 3,432,358, March 11, 1969.

E. J. Cairns and H. Shimotake  
*Recent Advances in Fuel Cells and Their Application to New Hybrid Systems*  
Advan. Chem. Ser. 90, 392 (1969).

E. J. Cairns, H. Shimotake, and A. K. Fischer  
*Lithium/Chalcogen Electrochemical Cells for Energy Storage*  
ANL Reviews 5(2), 87 (1969).

M. G. Chasanov, R. V. Schablaske, and I. Johnson  
*The System Ta-Zn: Phase Studies*  
J. Electrochem. Soc. Japan 36, 192-196 (1968).

A. A. Chilenskas  
*Volatility Experiments on Irradiated Fuels*  
Proc. Rocky Flats Fluoride Volatility Conf., Golden, Colo., June 24-25, 1968, USAEC Report CONF-680610 (1969), pp. 63-64.

C. E. Crouthamel, N. R. Stalica, C. E. Johnson, and C. A. Seils  
*Electron Microprobe Studies of the Migration of Elements in Irradiated Oxide Fuels*  
Abstracts of Papers Presented at the 158th Amer. Chem. Soc. Mtg., New York, Sept. 8-12, 1969. NUCL-47.

C. E. Crouthamel and N. D. Dudey  
*Radiochemical Analysis and Tracer Applications*  
Chapter in Encyclopedia of Chemical Technology, 2nd Ed., Vol. 17, John Wiley & Sons (1968), pp. 35-54.

P. M. Danielson  
*A Demountable Induction Heater Power-Lead Coupling for Use in Ultrahigh Vacuum*  
Rev. Sci. Instrum. 40(5), 736-737 (1969).

P. M. Danielson and J. S. Hetherington  
*Ultrahigh Vacuum Equipment for Materials Studies above 2000°C*  
Int. Trans. Vacuum Metallurgy Conf., New York, June 1967, E. L. Foster (ed.), Amer. Vacuum Soc., New York (1968), pp. 305-319.

P. M. Danielson and F. C. Mrazek  
*A Foreline Trap for Contamination-Free Roughing*  
J. Vac. Sci. Technol. 6(3), 423-425 (1969).

P. M. Danielson  
*Sealing Large Ultrahigh-Vacuum Flanges with Polytetrafluoroethylene Gaskets*  
J. Vac. Sci. Technol. 6(3), 425-427 (1969).

P. M. Danielson  
*A Demountable, Stainless Steel-to-Aluminum Transition Seal for Ultrahigh Vacuum*  
Vacuum 19, 365 (August 1969). Letter.

P. M. Danielson  
*A Design for Modular Ultrahigh Vacuum Feedthrough*  
Vacuum 19, 412 (September 1969).

- N. D. Dudgey, R. R. Heinrich, J. Williams, and A. A. Madson  
*Nuclear Reaction Rates in EBR-II Irradiated Stainless Steel*  
Nucl. Appl. and Technol. 7(1), 35-43 (1969).
- N. D. Dudgey  
*The Role of Nuclear Chemistry in Fast Reactor Development*  
Abstracts of Papers Presented at the 158th Amer. Chem. Soc. Mtg., New York, Sept. 8-12, 1969.  
NUCL-36.
- N. D. Dudgey, L. E. Ross, and V. E. Noshkin  
*Application of Activation Analysis and Ge(Li) Detection Techniques for the Determination of Stable Elements in Marine Aerosols*  
Modern Trends in Activation Analysis, Proc. 1968 Int. Conf. Gaithersburg, Md., Oct. 7-11, 1968, Nat. Bur. Std. Spec. Publ. 312, Vol. 1, U.S. Dept. Commerce, Washington (June 1969), pp. 55-61.
- N. D. Dudgey, R. R. Heinrich, and A. A. Madson  
*Fast Neutron Capture by Vanadium and Titanium*  
J. Nucl. Energy 23(8), 443-456 (1969).
- J. J. Dutton, J. Royal, D. H. Lennos, and R. Gold (eds.)  
Reactor and Fuel-Process. Technol. 11(4), Division of Technical Information, U.S. Atomic Energy Commission (Fall 1968).
- J. G. Eberhart, F. A. Cafasso, H. M. Feder, and W. Kremsner  
*The Grain Boundary Grooving of Iron in Liquid Sodium*  
Abstr. Bull. Met. Soc. AIME Fall Mtg., Philadelphia, Pa., Oct. 13-16, 1969 (1969), p. 128.
- R. K. Edwards  
*Law of Maxima in Species Partial Pressures for Equilibria in Two-Component Systems*  
High Temp. Sci. 1(2), 232-237 (1969).
- R. K. Edwards, M. S. Chandrasekharaiah, and P. M. Danielson  
*The Congruently Evaporating Compositions of Urania*  
High Temp. Sci. 1(1), 98-113 (1969).
- D. F. Fischer and J. G. Schnitzlein  
*The Ignition of Irradiated Uranium*  
J. Nucl. Mater. 28, 124-128 (1968).
- J. Fischer  
*Glove Box Facility for Pyrochemical Research and Development Work with  $^{238}\text{Pu}$*   
Proc. 17th Conf. Remote Syst. Technol., San Francisco, November 1969, Amer. Nucl. Soc. (1969), pp. 63-73; also published in Trans. Amer. Nucl. Soc. 12(2), 848 (1969). Abstract.
- H. E. Flotow, W. N. Hubbard, P. A. G. O'Hare, D. W. Osborne, and J. L. Settle  
*Heat Capacity from 1 to 350°K and Enthalpy of Formation at 298.15°K of Uranium Diboride*  
Preprints of Papers Presented at 1st International Conference on Calorimetry and Thermodynamics, Warsaw, Poland, Sept. 3, 1969. Paper No. 02.
- H. E. Flotow, D. W. Osborne, P. A. G. O'Hare, J. L. Settle, F. C. Mrazek, and W. N. Hubbard  
*Uranium Diboride: Preparation, Enthalpy of Formation at 298.15°K, Heat Capacity from 1 to 350°K, and Some Derived Thermodynamic Properties*  
J. Chem. Phys. 51, 583-592 (July 15, 1969).
- D. R. Fredrickson, R. Kleb, R. L. Nuttall, and W. N. Hubbard  
*A Drop Calorimeter with an Electron Beam Heated Furnace*  
Rev. Sci. Instr. 40, 1022-1025 (August 1969).
- D. R. Fredrickson, M. G. Chasanov, R. D. Barnes, and S. A. Johnson  
*The Enthalpy of Fusion of  $\text{Na}_3\text{Bi}$  by Drop Calorimetry*  
Abstracts of Papers Presented at 24th Annual Calorimetry Conference, Portsmouth, N. H., Oct. 13-16, 1969 (1969), p. 57.
- D. R. Fredrickson, R. D. Barnes, M. G. Chasanov, R. L. Nuttall, R. Kleb, and W. N. Hubbard  
*The Enthalpy of  $\text{UB}_2$  from 600-1500°K by Drop Calorimetry*  
High Temp. Sci. 1(3), 373-380 (1969).
- J. D. Gabor  
*Interaction Effects on the Fluid Dynamics of Bubbles in a Fluidized Bed. Chain of Rising Bubbles in an Infinite Two-Dimensional Medium*  
Ind. Eng. Chem. Fundamentals 8, 84-91 (February 1969).
- E. C. Gay, P. A. Nelson, and W. P. Armstrong  
*Flow Properties of Suspensions with High Solids Concentration*  
A.I.Ch.E. (Amer. Inst. Chem. Eng.) J. 15(6), 815-822 (1969).
- E. Greenberg, H. M. Feder, and W. N. Hubbard  
*The Thermochimistry of HF: The Enthalpy of Formation of Liquid HF*  
Preprints of Papers Presented at 1st International Conference on Calorimetry and Thermodynamics, Warsaw, Poland, Sept. 2, 1969. Paper No. H2.

- E. Greenberg and W. N. Hubbard  
*Determination of the Enthalpy of Formation of Liquid HF by Direct Reaction of the Elements*  
 Abstracts of Papers Presented at 24th Annual Calorimetry Conference, Portsmouth, N. H., Oct. 13-16, 1969 (1969), p. 33.
- D. Gruen, M. Krumpelt, and I. Johnson  
*Electronic Absorption Spectra and the Nature of Dilute Solutions of Alkali Metals in Alkali Halides*  
 Chapter in Molten Salts: Characterization and Analysis, G. Mamantov (ed.), Marcel Dekker, New York (1969), pp. 169-188.
- D. C. Hampson, W. L. Sales, and L. F. Coleman  
*Operating Experience with an Argon Atmosphere at the Fuel Cycle Facility*  
 Proc. 16th Conf. Remote Systems Technol., Idaho Falls, March 11-13, 1969, Amer. Nucl. Soc. (1969), pp. 91-111.
- R. R. Heinrich, N. D. Dudey, and M. S. Foster  
*EBR-II Spectrum-Averaged Cross Sections*  
 Abstracts of Papers Presented at the 158th Amer. Chem. Soc. Mtg., New York, Sept. 8-12, 1969. NUCL-40.
- P. B. Henault, G. J. Bernstein, L. F. Coleman, E. R. Ebersole, W. J. Larson, and R. R. Smith  
*Identification of Failed Fuel Elements by Xenon Tag*  
 Trans. Amer. Nucl. Soc. 12(1), 102 (June 1969). Abstract.
- J. T. Holmes, L. B. Koppel, J. D. Gabor, D. Ramaswami, and A. A. Jonke  
*Engineering-Scale Studies of the Fluorination of Uranium Oxide with Bromine Pentafluoride*  
 Ind. Eng. Chem. Process. Des. Develop. 8(1), 43 (1969).
- P. K. Hon  
*Some Simple Techniques to Prepare Powder Samples for Spark Source Mass Spectrometric Analysis*  
 Anal. Chem. 41, 1148 (1969).
- W. N. Hubbard  
*Thermochemical Bond Energies of Some Fluorides*  
 Abstracts of Papers Presented at 24th Annual Calorimetry Conference, Portsmouth, N. H., Oct. 13-16, 1969 (1969), p. 14.
- R. L. Jarry and M. J. Steindler  
*The Reaction of Gaseous Bromine Trifluoride with  $U_3O_8$*   
 J. Inorg. Nucl. Chem. 31(6), 1847-1851 (June 1969). Note.
- C. E. Johnson and E. J. Hathaway  
*Lithium Hydride Systems: Solid-Liquid Phase Equilibria for the Ternary Lithium Hydride-Lithium Chloride-Lithium Iodide System*  
 J. Chem. Eng. Data 14, 174-175 (April 1969).
- C. E. Johnson, C. E. Crouthamel, H. Chen, and P. E. Blackburn  
*Studies in Mixed-Oxide Irradiated Fuels: Transport of Cladding Components*  
 Trans. Amer. Nucl. Soc. 12(2), 565 (1969). Abstract.
- C. E. Johnson and M. S. Foster  
*Phase Equilibrium Studies of Lithium Halide-Containing Electrolytes*  
 J. Electrochem. Soc. 116, 1612 (1969).
- G. K. Johnson, E. H. Van Deventer, O. L. Kruger, and W. N. Hubbard  
*The Enthalpies of Formation of Plutonium Dioxide and Plutonium Mononitride*  
 J. Chem. Thermodyn. 1, 89-98 (1969).
- G. K. Johnson and W. N. Hubbard  
*The Enthalpies of Formation of Crystalline and Amorphous Boric Oxide and Orthoboric Acid*  
 J. Chem. Thermodyn. 1, 459 (1969).
- G. K. Johnson, P. N. Smith, E. H. Appelman, and W. N. Hubbard  
*The Thermodynamic Properties of Perbromate and Bromate Ions*  
 Inorg. Chem. 9, 119 (1970).
- I. Johnson  
*The Solubility of Uranium and Plutonium in Liquid Alloys*  
 Proc. Symp. Reprocessing of Nuclear Fuels, Ames, Iowa, Aug. 25-27, 1969, Nuclear Metallurgy, Vol. 15, USAEC Report CONF-690801 (1969), pp. 547-564.
- A. A. Jonke  
*Development of Volatility Process for Thermal and Fast Reactor Fuels*  
 Proc. Rocky Flats Fluoride Volatility Conf., Golden, Colo., June 24-25, 1968, USAEC Report CONF-680610 (1969), pp. 65-78.

- A. A. Jonke, N. M. Levitz, and M. J. Steindler  
*The Potential of the Fluoride Volatility Process for Fast Breeder Reactor Fuels*  
 Proc. Symp. Reprocessing of Nuclear Fuels, Ames, Iowa, Aug. 25-27, 1969, Nuclear Metallurgy, Vol. 15, USAEC Report CONF-690801 (1969), pp. 231-240.
- R. W. Kessie  
*Containment of PuF<sub>6</sub>*  
 Proc. Rocky Flats Fluoride Volatility Conf., Golden, Colo., June 24-25, 1968, USAEC Report CONF-680610 (1969), pp. 166-184.
- J. B. Knighton, I. Johnson, and R. K. Steunenberg  
*Uranium and Plutonium Purification by the Salt Transport Method*  
 Proc. Symp. Reprocessing of Nuclear Fuels, Ames, Iowa, Aug. 25-27, 1969, Nuclear Metallurgy, Vol. 15, USAEC Report CONF-690801 (1969), pp. 337-362.
- W. Knoch, J. B. Knighton, and R. K. Steunenberg  
*Contribution to the Plutonium-Magnesium Phase Diagram*  
 Proc. Symp. Reprocessing of Nuclear Fuels, Ames, Iowa, Aug. 25-27, 1969, Nuclear Metallurgy, Vol. 15, USAEC Report CONF-690801 (1969), pp. 535-546.
- T. S. Krolkowski, L. Leibowitz, R. E. Wilson, J. C. Cassulo, and S. K. Styne  
*The Reaction of Molten Sodium Spray with Air in an Enclosed Volume. Part I. Experimental Investigation*  
 Nucl. Sci. Eng. 38, 156-160 (November 1969).
- T. S. Krolkowski, L. Leibowitz, R. O. Ivins, and S. K. Styne  
*The Reaction of Molten Sodium Spray with Air in an Enclosed Volume. Part II. Theoretical Model*  
 Nucl. Sci. Eng. 38, 161-166 (November 1969).
- M. Krumpelt, I. Johnson, and J. J. Heiberger  
*Cadmium-Neptunium-A Partial Phase Diagram of the System*  
 J. Less-Common Metals 18(1), 35-40 (1969).
- M. L. Kyle, R. D. Pierce, and V. M. Kolba  
*Containment Materials for Pyrochemical Processes*  
 Proc. Symp. Reprocessing of Nuclear Fuels, Ames, Iowa, Aug. 25-27, 1969, Nuclear Metallurgy, Vol. 15, USAEC Report CONF-690801 (1969), pp. 433-452.
- M. L. Kyle, R. D. Pierce, and K. R. Tobias  
*A Titanium Gettering System for Purification of Glove Box Atmospheres*  
 Proc. 17th Conf. Remote Syst. Technol., San Francisco, November 1969, Amer. Nucl. Soc. (1969), pp. 185-191; also published in Trans. Amer. Nucl. Soc. 12(2), 859 (1969). Abstract.
- R. P. Larsen, R. V. Schablaske, R. D. Oldham, R. J. Meyer, and M. I. Homa  
*X-Ray Spectrometric Determination of Fission Product Rare Earths. Application to the Measurement of Burnup in Nuclear Fuels*  
 Abstracts of Papers Presented at the 158th Amer. Chem. Soc. Mtg., New York, Sept. 8-12, 1969. NUCL-49.
- R. P. Larsen, K. K. S. Pillay, and R. J. Meyer  
*Fast Fission Yield of <sup>141</sup>Pr Using Neutron Activation Analysis*  
 J. Radioanal. Chem. 3, 235 (1969).
- T. W. Latimer, L. A. Neimark, C. E. Johnson, and C. E. Crouthamel  
*Compatibility of Carbide Fuels with Potential LMFBR Claddings*  
 Trans. Amer. Nucl. Soc. 12(2), 594 (1969). Abstract.
- L. Leibowitz, L. W. Mishler, and M. G. Chasanov  
*Enthalpy of Solid Uranium Dioxide from 2500°K to Its Melting Point*  
 J. Nucl. Mater. 29, 356-358 (March 1969).
- L. Leibowitz, M. G. Chasanov, and L. W. Mishler  
*The Enthalpy of Solid Tungsten from 2800°K to Its Melting Point*  
 Trans. Met. Soc. AIME 245, 981-984 (May 1969).
- N. M. Levitz  
*Fluorination of Uranium and Plutonium to Hexafluorides*  
 Proc. Rocky Flats Fluoride Volatility Conf., Golden, Colo., June 24-25, 1968, USAEC Report CONF-680610 (1969), pp. 18-41.
- N. M. Levitz, E. L. Carls, D. Grosvenor, G. J. Vogel, and I. Knudsen  
*Engineering-Scale Fluoride Volatility Studies on Plutonium-Bearing Fuel Materials*  
 Proc. Symp. Reprocessing of Nuclear Fuels, Ames, Iowa, Aug. 25-27, 1969, Nuclear Metallurgy, Vol. 15, USAEC Report CONF-690801 (1969), pp. 211-230.



- N. M. Levitz, G. J. Vogel, E. L. Carls, D. E. Grosvenor, B. J. Kullen, D. J. Raue, and W. A. Murphy  
*Production of Plutonium Hexafluoride by Fluorination in a Fluidized Bed*  
Nucl. Appl. 6(2), 147-155 (1969).
- H. A. Liebhafsky and E. J. Cairns  
Fuel Cells and Fuel Batteries. A Guide to Their Research and Development, John Wiley & Sons, New York (1968).
- J. O. Ludlow, L. F. Coleman, V. M. Drabek, L. E. Ross, and M. A. Slawewski  
*Cathodic Etcher*  
Proc. 16th Conf. Remote Systems Technol., Idaho Falls, March 11-13, 1969, Amer. Nucl. Soc. (1969), p. 309. Note.
- J. O. Ludlow, L. F. Coleman, T. W. Eckels, J. E. A. Graae, L. E. Ross, and M. A. Slawewski  
*Start-up of Shielded Fuel Evaluation Facility*  
Proc. 16th Conf. Remote Systems Technol., Idaho Falls, March 11-13, 1969, Amer. Nucl. Soc. (1969), pp. 56-61.
- J. T. Madell, N. D. Dudgey, R. R. Heinrich, and R. E. Jarka  
*Analysis of Recent Dosimetry Experiments in EBR-II*  
Trans. Amer. Nucl. Soc. 12(2), 939 (1969). Abstract.
- R. F. Malecha, L. F. Coleman, P. Fineman, A. S. Kelecus, and M. A. Slawewski  
*EBR-II Intrasite Spent-Fuel Shipping Casks*  
Proc. 16th Conf. Remote Systems Technol., Idaho Falls, March 11-13, 1969, Amer. Nucl. Soc. (1969), pp. 205-211.
- V. A. Maroni and E. J. Cairns  
*A Review of Raman Spectroscopy of Fused Salts and Studies of Some Halide-Containing Systems*  
Chapter in Molten Salts: Characterization and Analysis, Gleb Mamantov (ed.), Marcel Dekker, Inc., New York (1969), pp. 231-239.
- V. A. Maroni and E. J. Cairns  
*Studies of a Li/P<sub>4</sub>S<sub>10</sub> Electrochemical Cell*  
Abstracts of Papers Presented at the 158th Amer. Chem. Soc. Mtg., New York, Sept. 8-12, 1969. PHYS-113.
- W. E. Miller and R. K. Steunenberg  
*Compact Pyrochemical Processes*  
Reactor and Fuel-Process. Technol. 11(4), 219-226 (Fall 1968).
- P. A. Nelson, D. E. Grosvenor, S. Vogler, N. P. Quattropani, and P. W. Krause  
*Synthesis and Fabrication of (U,Pu)C Nuclear Fuel Pellets from U-Pu Alloy*  
Bull. Amer. Ceram. Soc. 48(9), 863 (1969).
- P. A. G. O'Hare, W. N. Hubbard, and O. Glemser  
*A Thermochemical Study of NSF<sub>3</sub> and Bond Energies of Thiazyl Fluorides*  
Abstracts of Papers Presented at the 158th Amer. Chem. Soc. Mtg., New York, Sept. 8-12, 1969. PHYS-244.
- P. A. G. O'Hare, J. E. Johnson, B. E. Klamecki, M. E. Mulvihill, and W. N. Hubbard  
*The Enthalpy of Formation of Germanium Tetrafluoride*  
J. Chem. Thermodyn. 1, 177-181 (1969).
- R. D. Pierce, W. E. Miller, J. B. Knighton, and G. J. Bernstein  
*Multistage Contactors for Liquid Metal-Salt Extraction*  
Proc. Symp. Reprocessing of Nuclear Fuels, Ames, Iowa, Aug. 25-27, 1969, Nuclear Metallurgy, Vol. 15, USAEC Report CONF-690801 (1969), pp. 511-533.
- J. G. Riha, L. E. Trevorow, and M. J. Steindler  
*Separation of Ruthenium and Plutonium by a Lithium Fluoride Sorption Technique*  
U.S. Patent No. 3,458,291 (to USAEC), July 29, 1969.
- L. E. Ross, V. M. Drabek, and R. P. Larsen  
*Colorimetric Determination of Zirconium with 1-(2-pyridylazo)-2-naphthol*  
Talanta 16(6), 748-750 (1969).
- L. E. Ross and R. A. Juvinall  
*A Small Cylindrical Separatory Funnel and Rack*  
J. Chem. Educ. 46, 322 (May 1969).
- R. Sharma and I. Johnson  
*Kinetics of the Reduction of UO<sub>2</sub> by Mg or Ca Dissolved in Molten Chlorides*  
J. Metals 21, 32A (March 1969). Abstract.
- H. Shimotake, G. L. Rogers, and E. J. Cairns  
*Secondary Cells with Lithium Anodes and Immobilized Fused-Salt Electrolytes*  
Ind. Eng. Chem. Process Des. Develop. 8, 51-56 (January 1969).

- H. Shimotake and E. J. Cairns  
*A Lithium/Sulfur Secondary Cell with a Fused-Salt Electrolyte*  
 Extended Abstracts of Electrochem. Soc. Industrial Electrolytic Div., Spring Mtg., New York, May 4-9, 1969, Vol. 5, Abst. No. 206 (1969), pp. 520-524.
- H. Shimotake and E. J. Cairns  
*A Lithium/Sulfur Secondary Cell with a Fused-Salt Electrolyte*  
 J. Electrochem. Soc. 116, 137C (1969). Abstract.
- H. Shimotake, A. K. Fischer, and E. J. Cairns  
*Secondary Cells with Lithium Anodes and Paste Electrolytes*  
 Proc. 4th Intersoc. Energy Conversion Eng. Conf., Washington, D.C., Sept. 22-26, 1969, AIChE, New York (1969), pp. 538-547.
- H. Shimotake and E. J. Cairns  
*Lithium/Chalcogen Secondary Cells*  
 Proc. Advances in Battery Technology Symp., Los Angeles, Dec. 6, 1968, Southern California-Nevada Section of Electrochemical Society (1969), p. 165.
- P. N. Smith, G. K. Johnson, and W. N. Hubbard  
*The Enthalpy of Formation of Aqueous Hydrogen Fluoride*  
 Abstracts of Papers Presented at 24th Annual Calorimetry Conference, Portsmouth, N. H., Oct. 13-16, 1969 (1969), p. 35.
- M. J. Steindler, L. J. Anastasia, L. E. Trevorow, and A. A. Chilenskas  
*Laboratory Development of the Fluoride Volatility Process for Oxidic Nuclear Fuels*  
 Proc. Symp. Reprocessing of Nuclear Fuels, Ames, Iowa, Aug. 25-27, 1969, Nuclear Metallurgy, Vol. 15, USAEC Report CONF-690801 (1969), pp. 177-210.
- M. J. Steindler  
*The Chemistry of Plutonium Hexafluoride*  
 Proc. Rocky Flats Fluoride Volatility Conf., Golden, Colo., June 24-25, 1968, USAEC Report CONF-680610 (1969), pp. 2-17.
- M. J. Steindler and A. A. Jonke  
*Plutonium Tetrafluoride Preparation and Separation by Sorption on Sodium Fluoride*  
 U.S. Patent No. 3,423,190, January 1969.
- R. K. Steunenberg, R. D. Pierce, and I. Johnson  
*Status of the Salt Transport Process for Fast Breeder Reactor Fuels*  
 Proc. Symp. Reprocessing of Nuclear Fuels, Ames, Iowa, Aug. 25-27, 1969, Nuclear Metallurgy, Vol. 15, USAEC Report CONF-690801 (1969), pp. 325-335.
- M. Tetenbaum and P. D. Hunt  
*High Temperature Vaporization Behavior of Uranium Carbides*  
 Bull. Amer. Ceram. Soc. 48, 462 (April 1969). Abstract.
- M. Tetenbaum and P. D. Hunt  
*High Temperature Thermodynamic Properties of Oxygen-Deficient Urania*  
 J. Chem. Phys. 49(11), 4739-4744 (1968).
- L. E. Trevorow  
*Process Chemistry of NpF<sub>6</sub>*  
 Proc. Rocky Flats Fluoride Volatility Conf., Golden, Colo., June 24-25, 1968, USAEC Report CONF-680610 (1969), pp. 140-160.
- G. J. Vogel and J. W. Simmons  
*Volatility Processes*  
 Reactor and Fuel-Process. Technol. 11(4), 209-218 (Fall 1968).
- W. J. Walsh, R. D. Pierce, and R. K. Steunenberg  
*Liquid-Metal Decladding Processes for Fast Breeder Fuel Reprocessing*  
 Trans. Amer. Nucl. Soc. 12(2), 445 (1969). Abstract.
- I. O. Winsch, R. D. Pierce, G. J. Bernstein, W. E. Miller, and L. Burris, Jr.  
*EBR-II Skull Reclamation Process*  
 Proc. Symp. Reprocessing of Nuclear Fuels, Ames, Iowa, Aug. 25-27, 1969, Nuclear Metallurgy, Vol. 15, USAEC Report CONF-690801 (1969), pp. 297-324.
- D. A. Wenz, I. Johnson, and R. D. Wolson  
*The CaCl<sub>2</sub>-Rich Region of the CaCl<sub>2</sub>-CaF<sub>2</sub>-CaO System*  
 J. Chem. Eng. Data 14, 250-252 (April 1969).
- D. A. Wenz and I. Johnson  
*Reaction of PuO<sub>2</sub> with Molten MgCl<sub>2</sub>*  
 Inorg. Nucl. Chem. Letters 4, 735-738 (December 1968).

**B. PAPERS ACCEPTED FOR PUBLICATION IN  
THE OPEN LITERATURE**

J. J. Barghusen, A. A. Jonke, N. M. Levitz, M. J. Steindler,  
and R. C. Vogel

*Fluid-Bed Fluoride Volatility Processing of Reactor Fuel  
Materials\**

Accepted for publication as a chapter in Progr. Nucl.  
Energy, Ser. III, Process Chemistry, Vol. 4.

J. E. Battles, W. A. Shinn, P. E. Blackburn, and R. K. Edwards  
*A Mass Spectrometric Study of the Volatilization  
Behavior in the Plutonium-Carbon System*

Accepted for publication in High Temp. Sci.

T. L. Denst, E. Greenberg, J. L. Settle, and W. N. Hubbard  
*An Improved Interconnecting Valve for a Two-  
Compartment Calorimetric Bomb*

Accepted for publication in Rev. Sci. Instrum.

J. D. Gabor

*Heat Transfer to Particle Beds with Gas Flow Less Than  
or Equal to That Required for Incipient Fluidization*

Accepted for publication in Chem. Eng. Sci.

J. D. Gabor and L. B. Koppel

*Interaction Effects on the Fluid Dynamics of Bubbles in  
a Fluidized Bed: Chain of Rising Bubbles in an Infinite  
Three Dimensional Medium*

Accepted for publication in Chem. Eng. Prog.  
Symp. Ser.

J. D. Gabor

*Wall-to-Bed Heat Transfer in Fluidized and Packed Beds*

Accepted for publication in Chem. Eng. Prog.  
Symp. Ser.

E. Greenberg, C. A. Natke, and W. N. Hubbard

*The Enthalpy of Formation of Silicon Carbide*

Accepted for publication in J. Chem. Thermodyn.

C. E. Johnson and C. E. Crouthamel

*Cladding Interactions in Mixed-Oxide Irradiated Fuels*

Accepted for publication in J. Nucl. Mater.

C. E. Johnson and A. K. Fischer

*New Measurements for the Sodium-Bismuth Phase  
Diagram*

Accepted for publication in J. Less-Common Metals.

I. Johnson, J. J. Heiberger, and J. Fischer

*Thermodynamics of Dilute Solutions of Neptunium in  
Liquid Magnesium*

Accepted for publication in Trans. Met. Soc. AIME.

I. Johnson and R. M. Yonco

*Thermodynamics of Cadmium- and Zinc-Rich Alloys in  
the Cd-La, Cd-Ce, Cd-Pr, Zn-La, Zn-Ce, Zn-Pr Systems*

Accepted for publication in Trans. Met. Soc. AIME.

T. R. Johnson, R. D. Pierce, F. G. Teats, and E. F. Johnston  
*Behavior of Countercurrent Liquid-Liquid Columns with  
a Liquid Metal*

Accepted for publication in A.I.Ch.E. (Amer. Inst.  
Chem. Eng.) J.

L. B. Koppel, R. D. Patel, and J. T. Holmes

*Statistical Models for Surface Renewal in Heat and Mass  
Transfer. Part III. Residence Time and Age  
Distributions\**

Accepted for publication in A.I.Ch.E. (Amer. Inst.  
Chem. Eng.) J.

L. B. Koppel, R. D. Patel, and J. T. Holmes

*Statistical Models for Surface Renewal in Heat and Mass  
Transfer. Part IV. Wall-to-Fluidized-Bed Heat Transfer  
Coefficients\**

Accepted for publication in A.I.Ch.E. (Amer. Inst.  
Chem. Eng.) J.

V. A. Maroni, D. M. Gruen, R. L. McBeth, and E. J. Cairns  
*Raman Spectrum and Vibrational Analysis for Gaseous  
Aluminum Chloride*

Accepted for publication in Spectrochim. Acta.

K. M. Myles

*The Ternary System Copper-Magnesium-Calcium*

Accepted for publication in J. Less-Common Metals.

P. A. G. O'Hare, W. N. Hubbard, O. Glemser, and  
J. Wegener

*Thiazyl Tri- and Monofluorides: Enthalpies of Forma-  
tion and Dissociation Enthalpies of the N≡S Bonds*

Accepted for publication in J. Chem. Thermodyn.

P. A. G. O'Hare, G. K. Johnson, and E. H. Appelman

*The Thermochemistry of Aqueous Xenon Trioxide*

Accepted for publication in Inorg. Chem.

P. A. G. O'Hare

*Dissociation Energies, Enthalpies of Formation, Ioniza-  
tion Potentials, and Dipole Moments of NS and NS\**

Accepted for publication in J. Chem. Phys.

E. Rudzitis, E. H. Van Deventer, and W. N. Hubbard

*The Enthalpy of Formation of Phosphorus Trifluoride*

Accepted for publication in J. Chem. Thermodyn.

\*Also listed in ANL-7550.

- R. A. Sharma  
*Liquidus and Eutectic Phase Equilibria in the Systems  $\text{CaI}_2\text{-CaCl}_2$ ,  $\text{CaI}_2\text{-CaF}_2$ , and  $\text{CaI}_2\text{-MgCl}_2$*   
Accepted for publication in High Temp. Sci.
- R. A. Sharma  
*Phase Diagrams for the Systems  $\text{MgCl}_2\text{-MgF}_2$ ,  $\text{CaCl}_2\text{-MgF}_2$ , and  $\text{NaCl-MgF}_2$*   
Accepted for publication in J. Amer. Ceram. Soc.
- R. Sridhar, C. E. Johnson, and E. J. Cairns  
*Phase Diagrams for the Systems  $\text{LiI-KI}$  and  $\text{LiI-RbI}$*   
Accepted for publication in J. Chem. Eng. Data.
- R. K. Steunenberg, R. D. Pierce, and L. Burris, Jr.  
*Pyrometallurgical and Pyrochemical Fuel Processing Methods\**  
Accepted for publication as a chapter in Progr. Nucl. Energy, Ser. III, Process Chemistry, Vol. 4.
- M. Tetenbaum and P. D. Hunt  
*Total Pressure of Uranium-Bearing Species over Oxygen-Deficient Urania*  
Accepted for publication in J. Nucl. Mater.
- L. E. Trevorrow, T. J. Gerding, and M. J. Steindler  
*Ultraviolet-Activated Synthesis of Plutonium Hexafluoride at Room Temperature*  
Accepted for publication in Inorg. Nucl. Chem. Letters.
- R. C. Vogel and S. Lawroski  
*Nuclear Fuels Reprocessing*  
Accepted for publication in Encyclopedia of Science and Technology.
- C. ANL REPORTS**
- J. Fischer  
*Glovebox Facility for Pyrochemical Research and Development Work with Plutonium-238*  
ANL-7568.
- D. E. Grosvenor, I. O. Winsch, W. E. Miller, G. J. Bernstein, and R. D. Pierce  
*Design and Application of Corrosion-resistant Heated Transfer Tubes for Liquid Metals and Salts*  
ANL-7522.
- J. T. Holmes, J. R. Pavlik, P. A. Nelson, and J. E. A. Graae  
*A High-temperature, Fluidized-bed Process for Converting Uranium Dioxide to Uranium Monocarbide*  
ANL-7482.
- T. R. Johnson, F. G. Teats, and R. D. Pierce  
*A Method for the Purification of Molten Salts*  
ANL-7603.
- J. B. Knighton, I. Johnson, and R. K. Steunenberg  
*Uranium Purification by the Process of Salt Transport*  
ANL-7524.
- T. S. Krolkowski  
*Violently Sprayed Sodium-Air Reaction in an Enclosed Volume*  
ANL-7472.
- J. F. Lenc, W. E. Miller, G. J. Bernstein, A. L. Chandler, R. C. Paul, and E. F. Johnston  
*Retorting Unit for Recovery of Uranium from Zinc-Magnesium Solutions*  
ANL-7503.
- N. M. Levitz, L. J. Anastasia, E. L. Carls, A. A. Chilenskas, J. E. A. Graae, A. A. Jonke, R. W. Kessie, R. P. Larsen, W. J. Mecham, D. Ramaswami, M. J. Steindler, and G. J. Vogel  
*A Conceptual Design Study of a Fluoride-volatility Plant for Reprocessing LMFBR Fuels*  
ANL-7583.
- C. Luner, H. M. Feder, and F. A. Cafasso  
*Carbon Transport in Liquid Sodium*  
Proc. Int. Conf. Sodium Technology and Large Fast Reactor Design, Argonne National Laboratory, Nov. 7-9, 1968, ANL-7520, Part I, pp. 455-459.
- R. J. Meyer, C. E. Johnson, and L. E. Ross  
*Trace Element Behavior in Sodium*  
Proc. Int. Conf. Sodium Technology and Large Fast Reactor Design, Argonne National Laboratory, Nov. 7-9, 1968, ANL-7520, Part I, pp. 291-294.
- W. E. Miller, G. J. Bernstein, J. F. Lenc, and R. C. Paul  
*Preparation of First Mark-IA Fuel Alloy for EBR-II*  
ANL-7474.
- P. A. Nelson and M. G. Chasanov  
*Uranium Nitride-Sodium Paste Fuel for Fast-reactor Blankets*  
ANL-7475.
- P. A. G. O'Hare  
*The Thermodynamic Properties of  $\text{P}_2$ ,  $\text{P}_4$  and Some Phosphorus Fluorides*  
ANL-7459.

\*Also listed in ANL-7550.

- P. A. G. O'Hare  
*The Thermodynamic Properties of Some Chalcogen Fluorides*  
ANL-7315.
- P. A. G. O'Hare  
*The Thermodynamic Properties of As<sub>2</sub>, As<sub>4</sub>, and Some Arsenic Fluorides*  
ANL-7456.
- P. A. G. O'Hare  
*The Thermodynamic Properties of Gaseous Ge<sub>2</sub>, GeF<sub>4</sub>, GeF<sub>2</sub>, and GeF*  
ANL-7523.
- J. W. Reishus, G. E. Gundersen, P. M. Danielson, and R. K. Edwards  
*Mass-spectrometric Effusion Study of Uranium Monophosphide*  
ANL-7514.
- E. Veleckis, K. E. Anderson, F. A. Cafasso, and H. M. Feder  
*Solubilities of Nitrogen Gas and Sodium Cyanide in Liquid Sodium*  
Proc. Int. Conf. Sodium Technology and Large Fast Reactor Design, Argonne National Laboratory, Nov. 7-9, 1968, ANL-7520, Part I, pp. 295-298.
- D. R. Vissers and M. J. Steindler  
*Laboratory Investigations in Support of Fluid-bed Fluoride Volatility Processes. Part XX. Fission Product Tellurium Off-Gas Disposal in the Fluid-bed Fluoride Volatility Process*  
ANL-7464.
- R. C. Vogel, M. Levenson, E. R. Proud, and J. Royal  
*Chemical Engineering Division Research Highlights, May 1968-December 1968*  
ANL-7550.
- R. C. Vogel, M. Levenson, E. R. Proud, and J. Royal  
*Chemical Engineering Division Annual Report 1968*  
ANL-7575.
- D. A. Wenz, R. D. Wolson, and I. Johnson  
*Reduction of Uranium Dioxide in Molten Salt-Metal Systems*  
ANL-7463.
- D. PAPERS PRESENTED AT SCIENTIFIC MEETINGS**
- J. P. Ackerman  
*Chemistry of Disodium Acetylide*  
Presented at Purdue University, Dec. 11, 1969.
- E. J. Cairns  
*Atomic Energy Commission Program on Secondary Cells*  
Presented at Power Information Center (PIC) Mtg., Fort Belvoir, Va., March 26, 1969.
- E. J. Cairns  
*High Energy Batteries*  
Presented at the Chicago Section of the Electrochemical Society, April 10, 1969.
- E. J. Cairns and H. Shimotake  
*Lithium/Sulfur Cells with Alkali Halide Electrolytes*  
Presented at Gordon Conference, Meridan, N. H., Aug. 25-29, 1969.
- C. E. Crouthamel  
*Electron Microprobe Studies of Fast Reactor Mixed Oxide Fuel*  
Libby-Cockroft Meeting, Los Alamos, New Mexico, June 10-12, 1969.
- P. M. Danielson  
*An Apparatus for High-Temperature Effusion Studies in Ultrahigh Vacuum*  
Presented at 6th Annual Symposium of Midwest Section of American Vacuum Society, Dallas, May 26-27, 1969.
- J. E. Draley  
*Corrosion by Liquid Sodium*  
Presented at Kansas State University, Dec. 3, 1969.
- N. D. Dudgey  
*Methods for Spectral Characterization in Fast Reactors*  
Presented at Lawrence Radiation Laboratory, Livermore, Calif., Dec. 3, 1969.
- J. G. Eberhart  
1. *A Relationship between the Surface Tension and Critical Properties of Liquid Metals*  
2. *Evidence for Repulsive Atomic Interactions in Liquid Metals from Bond Energy Calculations*  
Presented at New Mexico Section of American Vacuum Society Symposium on Surface Science, Evaporation and Effusion, Los Alamos, New Mexico, April 28-30, 1969.
- H. M. Feder  
*Interactions Between Cover Gases and Liquid Sodium: A Review*  
Presented at Libby-Cockroft Exchange Mtg., Harwell, England, Sept. 15-19, 1969.

- J. D. Gabor  
*Interaction Effects on the Fluid Dynamics of Bubbles in a Fluidized Bed*  
Presented at Northwestern University, March 3, 1969.
- J. D. Gabor and L. B. Koppel  
*Interaction Effects on the Fluid Dynamics of Bubbles in a Fluidized Bed*  
Presented at Symposium on Fluidization, 64th Nat. Mtg., AIChE, New Orleans, March 16-20, 1969.
- J. D. Gabor  
*Wall-to-Bed Heat Transfer Mechanisms in Fluidized and Packed Beds*  
Presented at Illinois Institute of Technology, Oct. 14, 1969.
- J. D. Gabor  
*Wall-to-Bed Heat Transfer Mechanisms in a Fluidized Bed*  
Presented at University of Notre Dame, Oct. 29, 1969.
- J. D. Gabor  
*Wall-to-Bed Heat Transfer in Fluidized and Packed Beds*  
Presented at 62nd Annual Mtg., AIChE, Washington, Nov. 16-20, 1969.
- E. C. Gay  
*Lithium/Selenium Cells*  
Presented at 1969 National Youth Conference on the Atom, Chicago, Ill., Oct. 24, 1969.
- J. T. Holmes  
*Application of Factorial Experiments to Research and Development Programs*  
Presented at Northwestern University, May 12, 1969.
- P. K. Hon  
*The Study of a Master Emulsion Calibration Curve for Quantitative Spark Source Mass Spectrometric Analysis*  
Presented at 17th Annual Conference on Mass Spectrometry and Allied Topics, Princeton, N. J., May 21, 1969.
- W. N. Hubbard  
*Recent Thermochemical Studies at Argonne National Laboratory*  
Presented at seminar of Philips Zentrallaboratorium, Aachen, Germany, Sept. 6, 1969.
- W. N. Hubbard  
*The Thermochemistry of Hydrogen Fluoride*  
Presented at National Bureau of Standards, Washington, Nov. 26, 1969.
- C. E. Johnson, C. E. Crouthamel, H. Chen, and P. E. Blackburn  
*Microprobe Analysis of Irradiated Fuel: Cladding Interactions*  
Presented at International Metallographic Society Mtg., San Francisco, Sept. 8-10, 1969.
- T. R. Johnson  
1. *Development of Pyrochemical Processes*  
2. *Some Studies Related to Mass Transfer in Metal-Salt Systems*  
Presented at Iowa State University, Oct. 16, 1969.
- M. Kobayashi, D. Ramaswami, and W. T. Brazelton  
*Pulsed-Bed Approach to Fluidization*  
Presented at Symposium on Fluidization, 64th Nat. Mtg., AIChE, New Orleans, March 16-20, 1969.
- M. Kobayashi, D. Ramaswami, and W. T. Brazelton  
*Heat Transfer from an Internal Surface to a Pulsed Bed*  
Presented at Symposium on Fluidization Fundamentals, 62nd Annual Mtg. AIChE, Washington, Nov. 16-20, 1969.
- R. P. Larsen, R. V. Schablaske, R. D. Oldham, R. J. Meyer, and M. I. Homa  
*X-Ray Spectrometric Determination of Fission Product Rare Earths - Application to Burnup Analysis*  
Presented at Libby-Cockroft Meeting, Los Alamos, New Mexico, June 10-12, 1969.
- R. D. Pierce  
*Pyrochemical Reprocessing of Fast Reactor Fuels*  
Presented at University of Illinois, Urbana, July 10, 1969.
- R. D. Pierce  
*Pyrochemical Reprocessing of Fast Reactor Fuels*  
Presented to Reactor Assessment Panel of Edison Electric Institute, Argonne, July 15, 1969.
- R. D. Pierce  
*The Salt Transport Process for Fast Reactor Fuels*  
Presented at The University of Texas at Austin, Nov. 3, 1969.
- H. Shimotake and E. J. Cairns  
*Lithium/Chalcogen Cells with Fused-Salt Electrolytes*  
Presented at Mid-year Meeting, Society of Automotive Engineers, Chicago, May 19, 1969.



H. Shimotake, M. L. Kyle, V. A. Maroni, and E. J. Cairns  
*Lithium/Sulfur Cells and Their Potential for Vehicle Propulsion*

Presented at the International Electric Vehicle Symposium, Phoenix, Ariz., Nov. 5-7, 1969.

N. R. Stalica, C. A. Seils, and C. E. Crouthamel  
*Electron Probe Microanalysis of Irradiated Oxide Fuels*

Presented at International Nuclear Symposium on Ceramic Fuels, American Ceramic Society, Washington, D.C., May 7, 1969.

M. J. Steindler  
*Fluoride Volatility Processes*

Presented at AEC Safeguards Training Program, Argonne, May 22, 1969.

R. K. Steunenberg  
*Hybrid Pyrochemical-Aqueous Processes for LMFBF Fuels*

Presented to Reactor Assessment Panel of Edison Electrical Institute, Argonne, July 15, 1969.

A. D. Tevebaugh  
*High-Temperature Studies of Materials for Liquid-Metal Cooled, Fast-Breeder Reactors*

Presented at The University of Iowa, Nov. 17, 1969.

R. C. Vogel  
*ANL - Chemical Engineering Division Research Highlights*

Presented at Purdue University, April 10, 1969.

R. C. Vogel  
*The Work of the Chemical Engineering Division*

Presented at University of Illinois, Urbana, April 22, 1969.

S. Vogler  
*Theory and Principles of Solvent Extraction*  
Presented at AEC Safeguards Training Program, Argonne, May 19, 1969.

W. J. Walsh  
*Pyrochemical Reprocessing of Nuclear Fuels*  
Presented at Iowa State University, March 20, 1969.

D. S. Webster  
*Survey of Reprocessing of Spent Reactor Fuels*  
Presented at The University of Michigan, Oct. 10, 1969.

D. S. Webster  
*Survey of Reprocessing of Spent Reactor Fuels*  
Presented at University of Cincinnati, Oct. 24, 1969.



ARGONNE NATIONAL LAB WEST



3 4444 00008273 5

2

